Check for updates



NANO · MICRO small
www.small-journal.com

# 2D Materials for Emerging Neuromorphic Vision: From Devices to In-Sensor Computing

*Pengshan Xie, Dengji Li, Weijun Wang, and Johnny C. Ho**

**The von Neumann architecture faces significant challenges in meeting the growing demand for energy-efficient, real-time visual processing in edge applications, primarily due to data-transfer bottlenecks between processors and memory. Two-dimensional (2D) materials, characterized by their atomic-scale thickness, adjustable optoelectronic properties, and diverse integration capabilities, present a promising avenue for advancing in-sensor computing. These material systems, which include ferroelectric 2D materials, topological insulators, and twistronic systems, enhance the device's ability to handle perception, computation, and storage efficiently. This review provides a comprehensive overview of the latest advancements in 2D material systems, exploring their operational mechanisms and key visual perceptual functions, such as polarization sensing and spectral selection. The potential applications of visual neural synaptic devices within current material systems are also examined, highlighting ongoing efforts to integrate various deep learning algorithmic architectures with innovative device integration strategies. This includes everything from demand-side design to the selection of appropriate material systems. By merging device and materials innovation with neuromorphic engineering, 2D materials hold the promise of overcoming the limitations of the von Neumann architecture, paving the way for the development of intelligent vision systems that harness the power of in-sensor computing.**

## 1. Introduction

Modern computer architectures are fundamentally based on the classical von Neumann architecture, which integrates data and program storage in a unified memory, with the central processing unit (CPU) executing computations by retrieving instructions from this memory.[1–3] This architecture primarily relies on sequential execution controlled by the central processor. Despite advancements that have led to more complex instruction sets, enhanced processing units, and expanded memory capacity, thereby improving computing system performance, the von Neumann architecture faces significant limitations and challenges, particularly in terms of performance enhancement and energy efficiency as technology progresses.[4] The most notable of these challenges is the von Neumann bottleneck, a performance constraint arising from the limited speed of data transfers between the CPU and memory.[5] These issues are especially pronounced in visual perception tasks, where the increasing volume of image and video data necessitates rapid and frequent data exchanges between the CPU and memory.[6] This separation between storage and processing results in insufficient memory bandwidth, access delays, and performance degradation. Machine vision, which serves as a critical link between AI and real-world applications, demands more from architectural designs. In embedded systems, such as self-driving cars, robots, and smart cameras, in-sensor computing architectures that integrate computational capabilities within the sensor itself hold significant promise for real-time data processing, intelligent decision-making, and edge computing applications.[7]

The choice of semiconductor material system plays a pivotal role in determining the computing, storage, energy efficiency, and responsiveness of neuromorphic devices. 2D material systems are emerging as strong contenders to traditional silicon materials, garnering significant interest in the artificial intelligence (AI) field due to their exceptional electrical conductivity, unique physicochemical properties, and diverse material options, all of which hold great potential for future in-sensor computing architectures.[8] Unlike bulk materials, 2D materials, with their structure comprising only a few atomic or even a single layer, offer ultrafast carrier mobility, high-density integration efficiency, reduced energy consumption, and tunable quantum effects. Specifically, this material system offers a variety of advantages in in-sensor computing compared to bulk or thin film

P. Xie, D. Li, W. Wang, J. C. Ho
Department of Materials Science and Engineering
City University of Hong Kong
Hong Kong SAR 999077, China
E-mail: johnnyho@cityu.edu.hk
J. C. Ho
State Key Laboratory of Terahertz and Millimeter Waves
City University of Hong Kong
Hong Kong SAR 999077, China
J. C. Ho
Shenzhen Research Institute
City University of Hong Kong
Shenzhen 518057, China
J. C. Ho
Institute for Materials Chemistry and Engineering
Kyushu University
Fukuoka 816–8580, Japan

The ORCID identification number(s) for the author(s) of this article can be found under https://doi.org/10.1002/smll.202503717

**DOI: 10.1002/smll.202503717**

 © 2025 Wiley-VCH GmbH

materials. In order to achieve sensing-computing integration and reduce the latency and power consumption generated by data handling, the material needs to perform neural-like functions at the sensing end. Therefore, excellent optoelectronic properties are an important foundation. Many 2D materials (e.g., molybdenum disulfide, black phosphorus) are extremely sensitive to optical signals, and can achieve high responsivity, detectivity, and ultrawide detection band, demonstrating detection advantages over silicon-based materials. Second, compared to various thin film materials (including polycrystalline and amorphous films), ultrathin 2D materials can greatly avoid interfacial scattering and trapping caused by grain boundaries and defects during carrier transport. As a result, 2D materials also offer certain advantages in terms of carrier mobility and device switching performance, demonstrating smaller switching voltages and operating power consumption. In particular, compared to some n-type organic semiconductor materials, some n-type 2D materials have better stability in the air environment. Finally, regarding sensing dimensions, 2D materials can couple multiple physical fields. A series of 2D materials has demonstrated high sensitivity to external stimuli such as light, electricity, heat, and force. By coupling and decoupling different stimulus responses, neuromorphic devices based on 2D materials can perform fusion analysis and individual discrimination of complex stimulus scenarios. Miniaturization and wearability of sensory processing systems are important foundations for the future development of human–machine interfaces. 2D materials have an advantage over metal oxide films regarding bending strain and scalability. The interlayer van der Waals (vdW) forces of 2D materials confer a certain sliding ability on the lattice. Combined with miniaturized preparation processes and vdW electrode contacts, interlayer sliding of materials and material/electrode sliding would substantially release the effects of external stresses on the microdevices. In-sensor computing visual perception architectures require devices capable of directly sensing and computing external stimuli in real time.[9] Consequently, 2D materials can fully exploit their multimodal properties to integrate various dimensions of information in machine vision perception. Current favorable material systems for achieving multimodal in-sensor computing for visual sensing include ferroelectric, thermoelectric, and spintronic 2D semiconductors, as well as topological insulators, all based on optoelectronic responses. Furthermore, the advent of twistronics introduces novel concepts for 2D materials in the realm of neuromorphic responses.[10,11]

The von Neumann bottleneck of traditional computing architectures has demonstrated significant limitations in many areas. The separation of sensors and processors, and the time and energy consumption associated with frequent data transfers, greatly limit the full integration of AI algorithms and hardware. **Figure 1**a shows a conventional computing architecture's information sensing, processing, and transmission flow. The captured information in analog form undergoes initial digitization through an analog-to-digital converter (ADC) module, after which it undergoes buffering in temporary storage buffers. This digitized information is subsequently routed to computational modules for analysis.[12] However, this conventional architecture employing sequential signal transformation and data transfer mechanisms demonstrates suboptimal energy efficiency characteristics while introducing significant processing delays. In visual

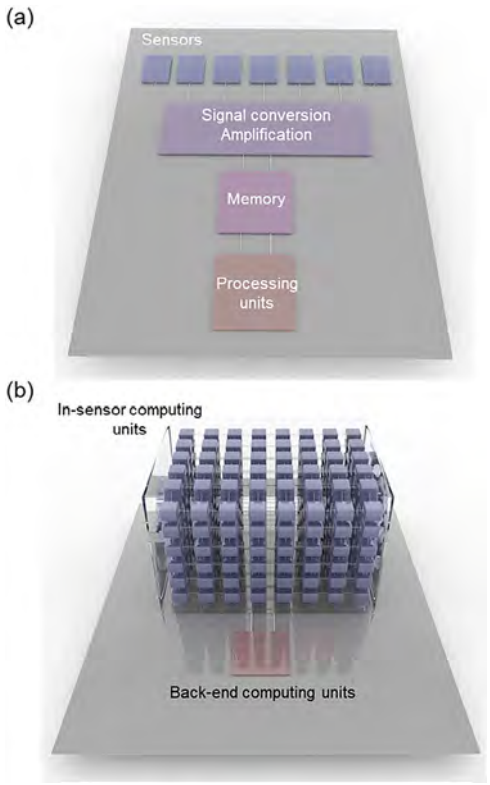


**Figure 1.** Schematic diagram of the workflow of a) von Neumann and b) in-sensor computing architectures.

sensing, the transmission of the object from the low-definition picture to the current high-definition video, the entire sensing, transmission, and processing system is experiencing huge functional changes and needs to be improved. In the early days, in order to cope with the rapid growth of data and the massive demand for computing power, cloud computing, which is centered on resource virtualization and centralized management, began to be widely used. As perceptual hardware rapidly evolves and imaging rates and pixel counts grow exponentially, bandwidth constraints and data explosion pressures make it difficult for cloud computing to process data quickly and in real-time, requiring immediate decision-making, such as autonomous driving and intelligent robotics. Therefore, this potential latency in data transfer and processing greatly limits the potential of cloud computing for offline, fast, real-time tasks.[13]

Thus, a better solution is to deploy computational tasks directly to sensing devices at the outer edges of the computer system, reducing unnecessary data movement. This structure, which processes analog information directly from the sensors and eliminates the sensor/processor interface, is the in-sensor computing architecture (Figure 1b). In particular, in-sensor computing architectures enable intrinsic execution of Boolean logic operations (AND, OR, NOT gates) and mathematical computations (including addition/multiplication algorithms) directly on the detection matrix.[14] Moreover, it also enables preliminary data processing (e.g., edge detection, feature extraction, dynamic filtering) to be done directly at the sensor layer, significantly reducing power consumption.[15] For further complex operations that require


© 2025 Wiley-VCH GmbH

16136829, 0, Downloaded from https://onlinelibrary.wiley.com/doi/10.1002/smll.202503717 by City University Of Hong Kong, Wiley Online Library on [19/08/2025]. See the Terms and Conditions (https://onlinelibrary.wiley.com/terms-and-conditions) on Wiley Online Library for rules of use; OA articles are governed by the applicable Creative Commons License

decision making, such as autonomous driving, object recognition, and so on, in-sensor computing architectures can greatly simplify the hardware design with extremely low latency for efficient advanced information processing such as classification, recognition, and coding. It is feasible to directly prepare in-sensor computing device layouts based on the actual computational matrix. According to Kirchhoff's laws, the resulting currents can be operated directly along a matrix circuit through a multimodal sensing process, where multiplication of different stimuli and responsiveness occurs in a single device. This real-time processing architecture, which is almost exclusively related to device response time and has no transmission delays, is suitable for various fast decision-making scenarios.

This review focuses on the emerging field of neuromorphic visual devices based on 2D material systems. We begin by exploring the current branches of 2D material systems widely utilized in visual neuromorphic computing, covering material preparation and system selection. We then summarize the current functional layer designs and operational principles of devices implementing optoelectronic neuromorphic responses. The subsequent section highlights several key functions in visual neuromorphic computing. Finally, we review the applications of various neuromorphic visual devices. Concluding with a forward-looking perspective, we discuss the perceptual and computational factors and challenges that must be addressed to implement more advanced in-sensor computing for artificial vision systems based on 2D materials. **Figure 2** illustrates visual neuromorphic devices' material systems and application prospects based on 2D materials.

## 2. 2D Material Systems

Since the 1990s, 2D materials have become a hotspot for research on semiconductor material systems. Their wide range of material choices and ideal optoelectronic response have made 2D materials a major candidate for replacing silicon-based materials in the future.[16] Particularly, 2D semiconductors exhibit excellent photoresponsivity and offer broad bandgap coverage. Additionally, the near-atomic thickness of these materials, characterized by covalent bonding and a surface free from dangling bonds, makes them an ideal platform for developing artificial visual systems and memristors.[17,18] After the successful mechanical exfoliation of graphene (Gr), the preparation and application of 2D materials have ushered in a brand-new outbreak. Organic 2D materials, transition metal dichalcogenides (TMDs), monoelemental 2D materials, Mxenes, and 2D perovskite have been widely used in artificial neural vision systems.[19,20]

For visual neuromorphic devices, the optoelectronic properties of the material are the priority. For different material systems, the energy band structure, bandgap, light absorption efficiency, and carrier transport modes will be different. For organic semiconductors, most of the materials have direct bandgaps, where $\pi$–$\pi$ conjugated systems form carrier transport channels that can efficiently conduct photogenerated carriers. The bandgap is usually between 1 and 3 eV, enabling detection from the ultraviolet (UV) to the near infrared (NIR) (**Figure 3a**).[21] The advantages of organic semiconductors lie in the high efficiency of light absorption, especially 2D organic semiconductors, to overcome the shortcomings of the carriers being easily compromised and low mobility. However, the lower photoelectric conversion efficiency limits the application of some organic 2D semiconductor materials. For TMDs, the bandgap is typically in the range of 1.0–2.5 eV, which is affected by the type of material and the number of layers. For most TMDs, the single layer is the direct bandgap, and the multilayer transition is the indirect bandgap (reduced bandgap). Thus, the response band of TMDs is similar to that of organic semiconductors (Figure 3b).[22] For monoelemental 2D materials and some other 2D material systems, the detection range can be extended from UV to terahertz (THz). In particular, some narrow bandgap materials, such as BP, exhibit ideal light absorption and carrier separation efficiencies and are well suited for high-performance optoelectronic devices. MXene is a typical light-absorbing material with very strong broadband absorption. However, the properties of its metallic state make it difficult for the photogenerated carriers to separate intrinsically. Hence, energy band design (heterojunction) or acting as other types of functional layers are often required. 2D perovskite has been a star material in photovoltaics, possessing excellent photovoltaic conversion capability and absorption efficiency. The detection band can range from visible light to NIR. However, the low carrier mobility is a major problem for these materials. This section will introduce the corresponding 2D material systems individually, including synthesis methods, crystal structures, device performance, and application scenarios.

### 2.1. Organic 2D Materials

Organic semiconductors possess excellent photoelectric response, a wide range of material options, versatile fabrication techniques, compatibility with flexible substrates, and relatively low costs, making them an indispensable component in the semiconductor field.[23,24] Depending on the type of material, 2D organic semiconductors can now be categorized into small-molecule and porous organic semiconductors.[25] Among them,1]benzothieno[3,2-b]benzothiophene (BTBT) material system is widely used in low-dimensional optoelectronic neuromorphic devices from material synthesis to different preparation methods. The unique electronic characteristics of BTBT stem from its delocalized $\pi$-electron system, where optimized intermolecular orbital interactions enable superior charge transport properties. Structural modifications through molecular engineering can significantly improve charge transfer efficiency. Specifically, elongation of the aromatic backbone, introduction of heteroatoms into the conjugated system, and functionalization with branched long alkyl side chains collectively reduce lattice vibration interference in charge transport processes.[26] Crystalline analysis reveals a lamellar organization with periodic alternation between aromatic moieties and insulating alkyl chains. This layered architecture enables face-to-edge molecular packing in the semiconductor component, creating efficient charge transport pathways through conjugated system interactions.[27] Current developments demonstrate that organic field-effect transistors utilizing BTBT derivatives achieve charge mobility parameters that are approaching those of conventional polycrystalline silicon semiconductors, suggesting promising applications in next-generation microelectronics, including flexible


© 2025 Wiley-VCH GmbH

16136829, 0, Downloaded from https://onlinelibrary.wiley.com/doi/10.1002/smll.202503717 by City University Of Hong Kong, Wiley Online Library on [19/08/2025]. See the Terms and Conditions (https://onlinelibrary.wiley.com/terms-and-conditions) on Wiley Online Library for rules of use; OA articles are governed by the applicable Creative Commons License

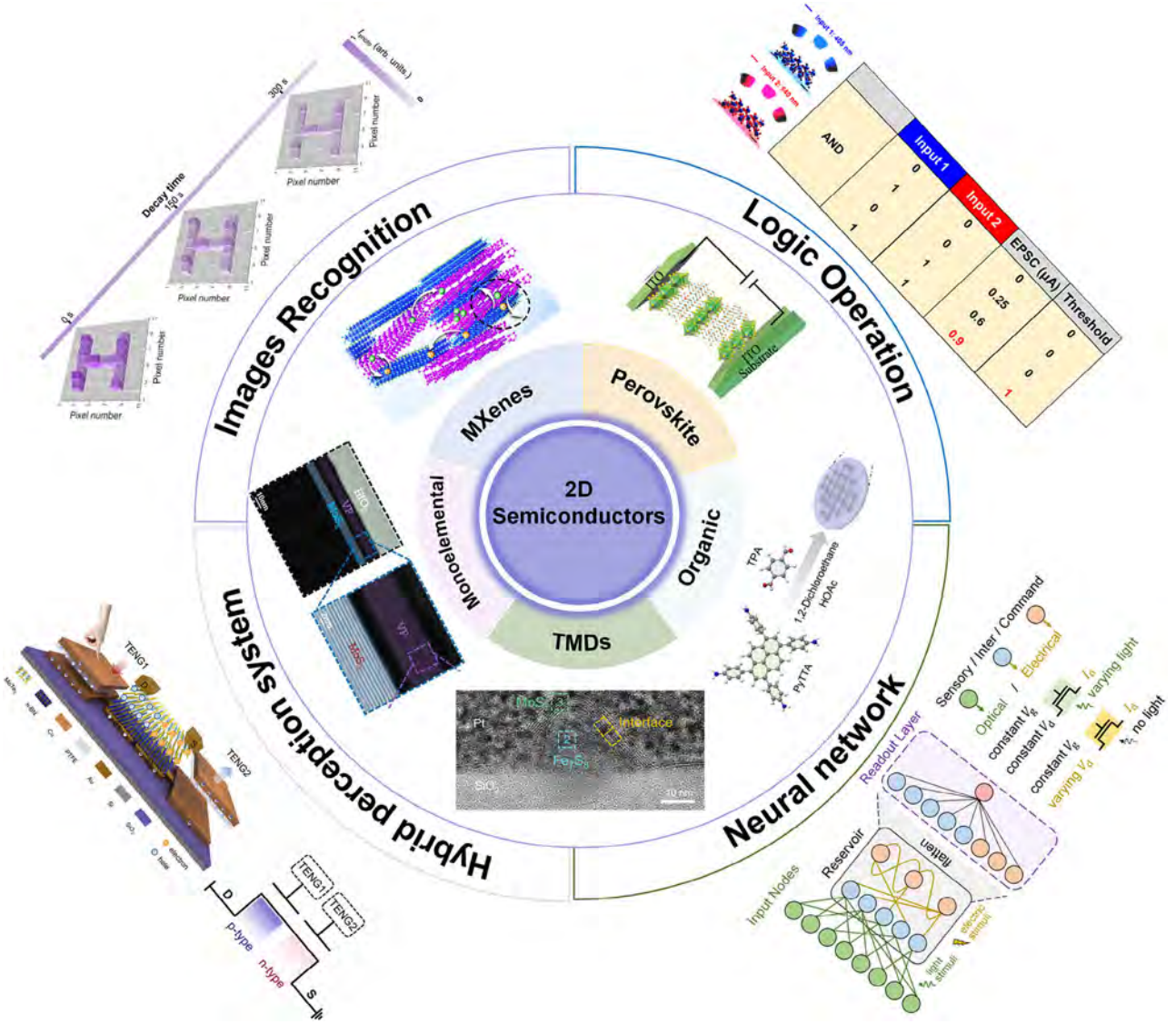


**Figure 2.** Specific classification and neuromorphic visual applications based on 2D material systems. Schematic of the synthesis in 2D COF films on Si substrate.[35] Copyright 2024, Wiley-VCH. Cross-sectional transmission electron microscopy (TEM) image of a heterojunction with wrapped structures.[55] Copyright 2024, Wiley-VCH. Cross-sectional HAADF scanning transmission electron microscope (STEM) images of the heterojunction.[76] Copyright 2023, Wiley-VCH. Schematic of MXene/VP hybrid films and photogenerated carrier transport.[81] Copyright 2024, Springer Nature. Schematic of vertical device structure and array based on 2D Perovskite.[95] Copyright 2024, Wiley-VCH. AND logic operation was realized by using two different light irradiations.[172] Copyright 2024, American Chemical Society. Graphical perception and memory of "H" shapes on a 10 × 10 device array.[181] Copyright 2023, Springer Nature. Schematic structure of the device with integrated strain sensing and its channel type modulation.[191] Copyright 2025, Elsevier. Schematic of the multimode RC system.[202] Copyright 2024, American Chemical Society.

circuit fabrication and integrated smart systems. Previously widely used preparation methods, such as spin-coating and thermal evaporation, are unsuitable for preparing 2D single-crystal organic semiconductors. Self-assembly and blade coating are preferred for both large area and high-quality preparations. Both blade coating and self-assembly involve solid–liquid and liquid–gas interfacial interactions and solvent evaporation processes in preparing thin films. Self-assembly utilizes intermolecular interactions (e.g., hydrogen bonding, vdW forces, etc.) to naturally arrange the molecules into an ordered structure on the assembled surface.[28] Blade coating involves first coating the organic solution onto a substrate with a spatula and then realizing an evaporation-crystallization process. Duan et al. adopted the blade coating method to fabricate optoelectronic synapses based on 2,7-Dioctyl[1]benzothieno[3,2-b][1]benzothiophene (C8-BTBT) organic single-crystal phototransistors (**Figure 4a**).[29] Polarized optical microscopy (POM) images and high-resolution atomic force microscopy (AFM) verified the anisotropy and crystallographic information of the organic crystal film. Because of efficient carrier transport in a single-crystal thin film, the device demonstrated an on/off ratio close to $10^8$ and a subthreshold swing (SS) of 59.8 mV $dec^{-1}$, which was suitable for low

 © 2025 Wiley-VCH GmbH

16136829, 0, Downloaded from https://onlinelibrary.wiley.com/doi/10.1002/smll.202503717 by City University Of Hong Kong, Wiley Online Library on [19/08/2025]. See the Terms and Conditions (https://onlinelibrary.wiley.com/terms-and-conditions) on Wiley Online Library for rules of use; OA articles are governed by the applicable Creative Commons License

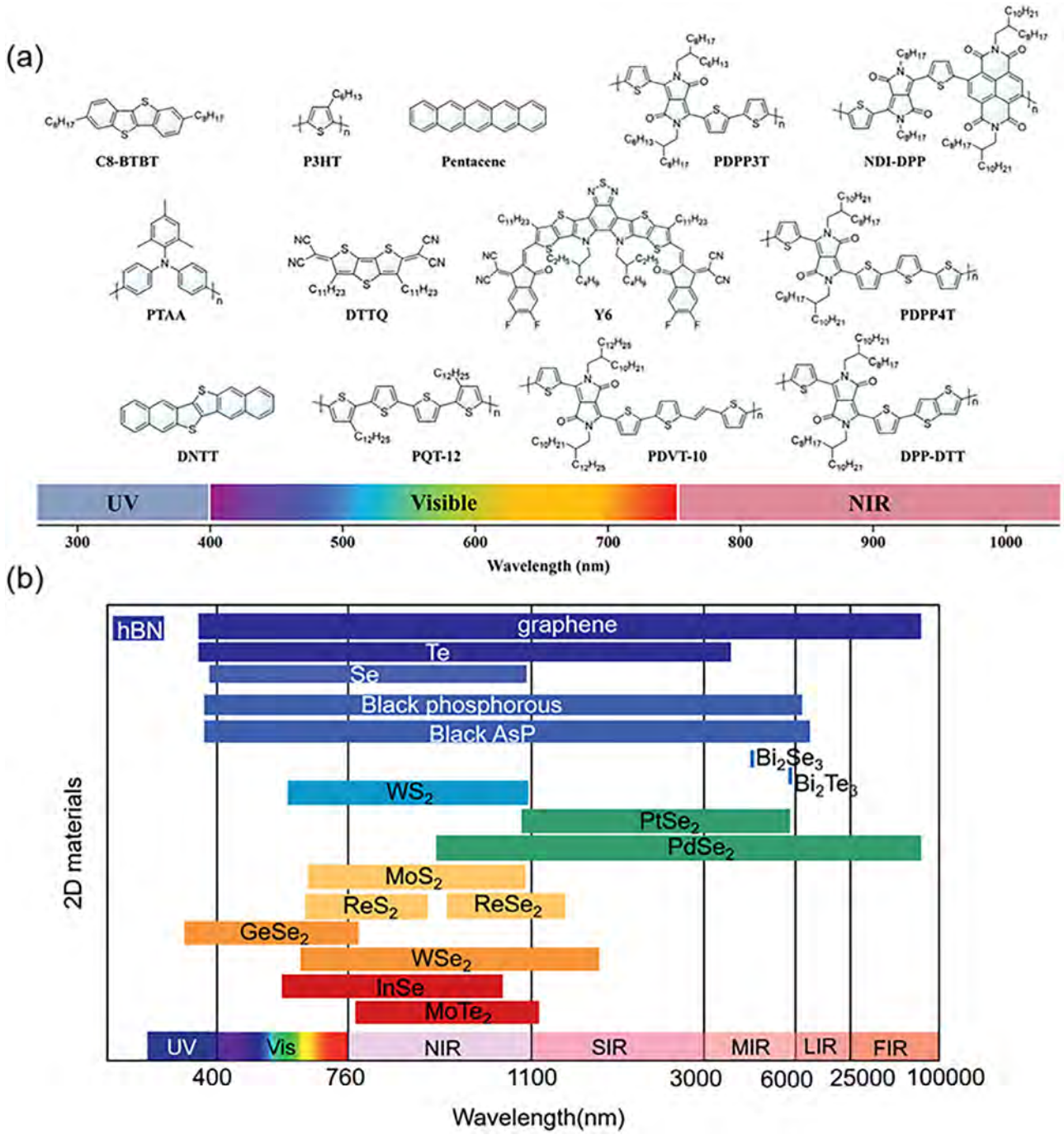


**Figure 3.** a) The molecular structure formulas of organic semiconductor materials and the absorption range.[21] Copyright 2023, Wiley-VCH. b) Response bands corresponding to partial inorganic 2D materials.[22] Copyright 2021, Wiley-VCH.

power consumption and ultrafast optoelectronic neuromorphic response.

The self-assembly allows for finer film thickness control than blade coating and a highly ordered arrangement of molecules in single or fewer layers. Lv et al. realized the lateral epitaxial growth of various 2D organic heterostructures using a vapor-phase growth method after the liquid-phase growth process.[30] Hu's group specializes in self-assembling 2D high-quality organic films using liquid interfaces. Among them, artificial visual systems widely use self-assembled 2D films based on BTBT organic small molecule material systems. The researchers successfully prepared a few-layered 2D C8-BTBT film on a glycerol interface, producing a high photoresponse of $2.3 \times 10^5$ A $W^{-1}$.[31] Then, they utilized a similar fabrication method to prepare a 2D molecular crystal optoelectronic synapse based on 2-decyl-7-phenyl-[1]benzothieno[3,2-b][1]benzothiophene (Ph-BTBT-10).


© 2025 Wiley-VCH GmbH

16136829, 0, Downloaded from https://onlinelibrary.wiley.com/doi/10.1002/smll.202503717 by City University Of Hong Kong, Wiley Online Library on [19/08/2025]. See the Terms and Conditions (https://onlinelibrary.wiley.com/terms-and-conditions) on Wiley Online Library for rules of use; OA articles are governed by the applicable Creative Commons License

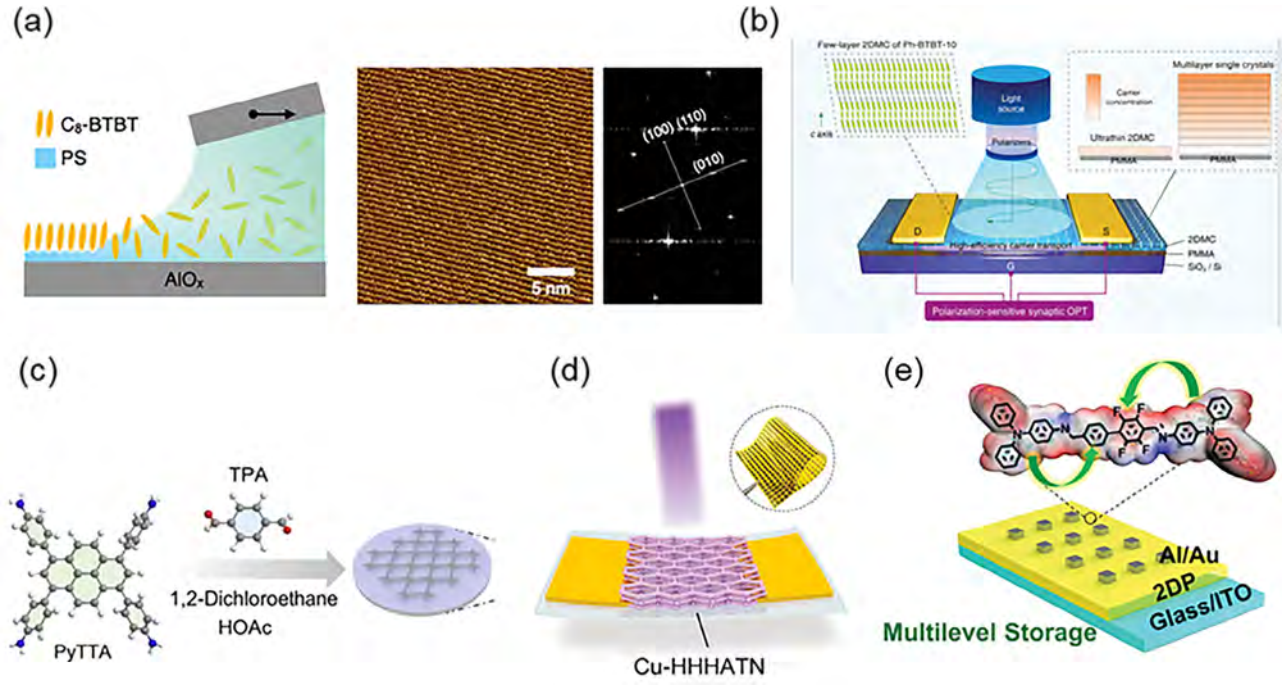


**Figure 4.** a) Schematic of the device structure based on 2D organic semiconductors (left). The corresponding high-resolution atomic force microscopy (AFM) of 2D C8-BTBT films and fast Fourier transform patterns (right).[29] Copyright 2024, Wiley-VCH. b) Schematic structure of the optoelectronic synaptic device based on 2D organic small molecule films.[32] Copyright 2024, Wiley-VCH. c) Schematic of the synthesis of 2D COF films on Si substrates.[35] Copyright 2024, Wiley-VCH. d) MOF-based two-terminal optoelectronic synaptic devices.[36] Copyright 2024, Wiley-VCH. e) Schematic diagram of a 2D polymer film-based visual synaptic device and its carrier transport pathway.[38] Copyright 2024, Wiley-VCH.

Due to the high-quality single organic crystal film, the device showed a high responsivity of $1.47 \times 10^4$ A $W^{-1}$ and effective polarized light detection. This multidimensional information perception capability was applied to noncontact fingerprint detection based on optoelectronic neuromorphic response and demonstrates reliable recognition (Figure 4b).[32]

At present, the most widely used pore-structured materials for visual simulation and optoelectronic neuromorphic response are covalent organic frameworks (COFs) and metal–organic frameworks (MOFs), which are distinguished by their structural composition and bonding mechanisms.[33] The former is a highly organized and porous crystal structure generated by the covalent bonding of organic molecules. The latter is a porous crystal structure formed by metal ions or metal clusters coordinated to organic ligands through coordination bonds. Although the applications of COF and MOF are still mainly focused on catalysis, MOF and COF materials also have significant advantages in photocatalysis due to their unique structures and properties, including broadband response, good carrier-directed transport properties, high specific surface area, and pore structure.[34] Hong et al. fabricated five highly crystalline 2D COF films based on different amino and aldehyde precursors (Figure 4c). Under the light stimulation, the devices realized the synaptic weight tunable characteristic, resulting in the photoconductivity changing from short-term plasticity (STP) to long-term plasticity (LTP).[35] Song et al. prepared a 2D HHHATN:hexahydroxyl-hexaazatrinaphthylene (Cu-HHHATN) COF film for optoelectronic synapses (Figure 4d). Due to the 1.46 eV bandgap and intermediate Fermi energy, the flexible device demonstrated broadband photoresponse ranging from UV to short-wave infrared (370 to 1450 nm).[36] Then, Wang et al. combined HHTP:2,3,6,7,10,11-hexahydroxytriphenylene hydrate (Cu-HHTP) COF film with MXene to realize underwater vision mimic based on light-driven active ion transport. Realization of a mixed ion transport mode due to temperature gradient and photoelectric effect under light using photothermal of MXene and photoelectric of Cu-HHTP properties.[37] In addition, polymer porous 2D films have been used in neuromorphic computing. Liu et al. designed the donor–acceptor–donor–acceptor alternating structure based on fluorine-containing 2D polymer film to realize the efficient capture of carriers, leading to long-term storage of conductivity information (Figure 4e).[38]

### 2.2. TMDs

Since the development of 2D semiconductors, TMDs have been a pivotal branch that is considered one of the most promising high-performance semiconductors to replace silicon-based materials. These materials feature a layered structure where covalent bonds hold the atoms together within each layer while vdW forces act between adjacent layers.[39,40] The diverse arrangements of transition metal atoms and chalcogen elements (like sulfur) contribute to various TMD crystal structures. TMDs exhibit various electronic states, including topological insulators, semiconductors, semi-metals, and superconductors.[41] Additionally, the different bonding configurations and structural arrangements give rise to various crystalline phases of TMDs. Regarding


© 2025 Wiley-VCH GmbH

16136829, 0, Downloaded from https://onlinelibrary.wiley.com/doi/10.1002/smll.202503717 by City University Of Hong Kong, Wiley Online Library on [19/08/2025]. See the Terms and Conditions (https://onlinelibrary.wiley.com/terms-and-conditions) on Wiley Online Library for rules of use; OA articles are governed by the applicable Creative Commons License

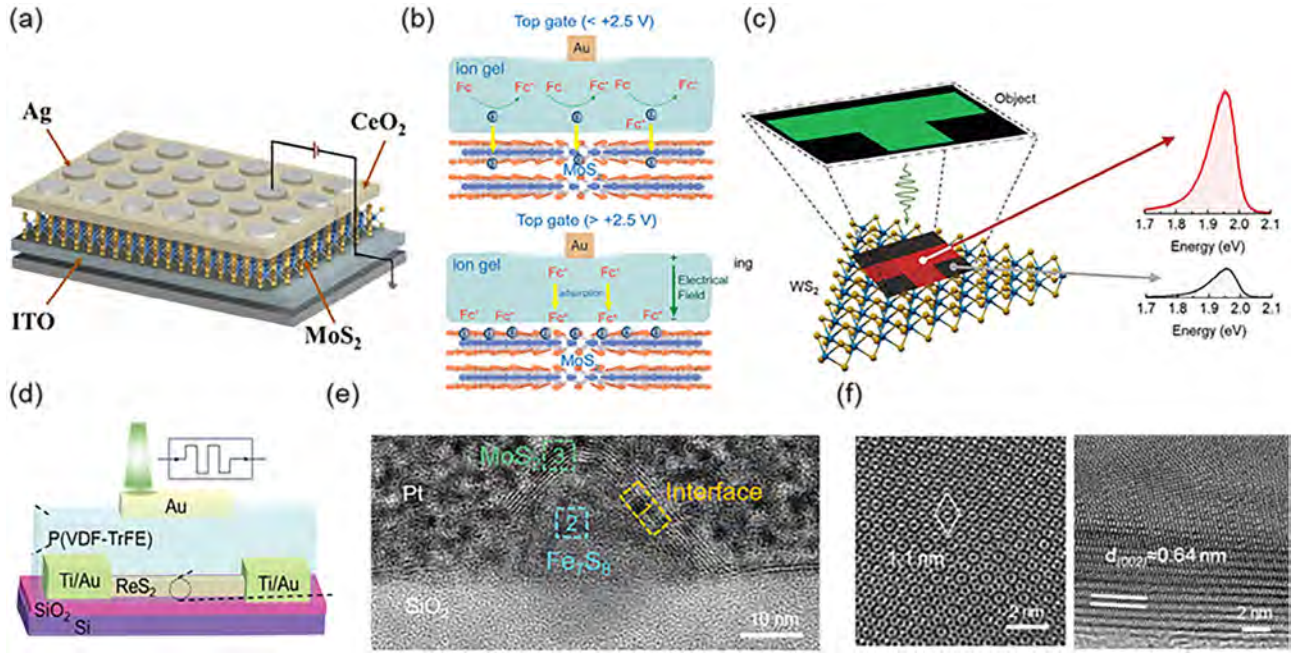


**Figure 5.** a) Schematic diagram of the vertical two-terminal visual synaptic device structure.[48] Copyright 2024, Elsevier. b) Schematic of charge transfer at the $MoS_2$ interface under ion gate modulation.[50] Copyright 2024, Wiley-VCH. c) Schematic of the perception process of $WS_2$-based optical-visual memory arrays.[51] Copyright 2024, Wiley-VCH. d) Schematic of the ferroelectric top-gate and 2D channel device.[54] Copyright 2024, Wiley-VCH. e) Cross-sectional transmission electron microscopy (TEM) image of the heterojunction with wrapped structures.[55] Copyright 2024, Wiley-VCH. f) The high-resolution TEM (HRTEM) image of the multilayer $MoSe_2$ moiré superlattice.[57] Copyright 2024, Wiley-VCH.

material structure, monolayer 2D TMDs mainly have 1H (hexagonal) phase and 1T (trigonal) phase. Among them, the 1T phase forms 1T' and 1T'' phases due to conformational distortions. After different stacking methods, the 1H phase can form 2H and 3R (rhombohedral) phases. The phase transitions are often accompanied by symmetry changes during the stacking process.[42] For the same TMDs, different crystallographic orientations often cause the material to exhibit different properties. Therefore, the multidimensional material properties of TMDs, including corresponding changes in optoelectronic properties with changes in the number of layers, have created broad conditions for applying TMDs in neuromorphic devices.[43] At present, in terms of material composition, TMDs are commonly denoted as MX or $MX_2$, where "M" stands for transition metal (such as Ti, Mo, Ta, Nb, W, or Re), and "X" represents a chalcogen element (such as S, Se, or Te).[44] For visual neuromorphic devices, the optoelectronic response of the material is critical. To ensure the visual response of the device, the material's forbidden bandwidth should be suitable for the target response band. Interestingly, the forbidden bandwidth of some 2D materials decreases as the number of layers increases, allowing for fine-tuning of the bandgap; they also convert from a direct bandgap to an indirect bandgap.[45] Therefore, a suitable material system is essential for TMD-based visual neuromorphic devices.

Currently, widely used material systems can be divided into S and Se according to the chalcogen element. For S element, $MoS_2$, $WS_2$, $ReS_2$, and $F_7S_8$ all have applications in visual neuromorphic devices. Among them, $MoS_2$ is the most widely used material due to its high carrier mobility and excellent photoelectric response.[46] Chai et al. utilized a large-area bilayer $MoS_2$ thin film to fabricate insect-like visual synaptic arrays. Efficient response to ultrafast optical stimuli using energy level defects and interfacial carrier trapping.[47] In order to modulate the optoelectronic response of $MoS_2$ channels, different types of device structures, energy band modulation, and insulating layers are valid approaches. A two-terminal $CeO_2/MoS_2$ heterostructured-optoelectronic channel was prepared by Lin et al. to realize a multifunctional artificial visual system with electrical storage, light sense, and memory, and visual nociceptors (**Figure 5a**).[48] Wang et al. on the other hand, used a ferroelectric insulating layer with $MoS_2$ channel to achieve optoelectronic coupling.[49] Various optoelectronic logic functions can be realized by adjusting the sequence of optoelectronic pulses. The opto-electrochemical channel modulation mechanism can also bind to $MoS_2$ by introducing an ion-gel. Modulation of channel conductance by electrochemical reactions enabled different responses to light stimuli (Figure 5b).[50] The $WS_2$, which also has a hexagonal crystal system structure, has optoelectronic properties similar to $MoS_2$. The bandgap of $WS_2$ is slightly larger than that of $MoS_2$ due to the larger atomic mass (monolayer), resulting in slight differences in detection bands. Lupi et al. adopted monolayers of $WS_2$ to achieve visual memory by laser-induced air environmental desorption/absorption process on the $WS_2$ surface (Figure 5c).[51] Gong et al. utilized $WS_2$ to fabricate the artificial visual recognition system. Combined with the in-sensor reservoir computing (RC) system, the photoresponse's temporal and spatial information was involved in data classification, training, and recognition.[52] In order to expand the perceptual dimension, $ReS_2$, belonging to the triclinic crystal system, has been introduced into the artificial vision system. Unlike other TMDs, the


© 2025 Wiley-VCH GmbH

16136829, 0, Downloaded from https://onlinelibrary.wiley.com/doi/10.1002/smll.202503717 by City University Of Hong Kong, Wiley Online Library on [19/08/2025]. See the Terms and Conditions (https://onlinelibrary.wiley.com/terms-and-conditions) on Wiley Online Library for rules of use; OA articles are governed by the applicable Creative Commons License

crystal in each layer of $ReS_2$ shows an irregular, low-symmetry arrangement. As a result, it exhibits strong anisotropy in electrical, optical, and mechanical properties, making it uniquely suited for different applications (e.g., polarization detection, optical imaging, etc.). Xie et al. realized polarization detection for artificial vision systems using the $ReS_2$ channel.[53] Like the works mentioned above, Dang et al. also utilized the ferroelectric dielectric layer to modulate the conductivity of the $ReS_2$ channel (Figure 5d).[54] Popular materials and some less commonly used TMDs are gradually being developed and assuming a function in artificial visual devices. $F_7S_8$ was adopted as the trapping layer to maintain the photoconductivity in the $MoS_2$ channel during light irradiation (Figure 5e).[55] In practical applications, combinations of different materials can achieve increased functionality and improved performance.[56]

For Se-based TMDs, the bandgap is usually smaller than the corresponding sulfur-based TMDs, making them more suitable for applications in the infrared range, such as infrared photodetectors, infrared solar cells, and so on. At present, widely used Se-based TMDs include $MoSe_2$ and $WSe_2$. Hu's group introduced a multilayer $MoSe_2$ moiré superlattice into an optical synapse to have broadband absorption from 240 to 1700 nm. The formation of moiré stripes in $MoSe_2$, attributed to interlayer lattice mismatch, enhanced the interlayer interactions, leading to the formation of interlayer excitons, further reducing the bandgap. The enhanced NIR photoresponse was realized, and the NIR synaptic functions were achieved (Figure 5f).[57] Gong et al. utilized $WSe_2$ as the channel material to fabricate visible-range artificial visual system arrays. Combined with certain spectrally selective properties, the array demonstrated a good recognition rate in artificial neural networks (ANN).[58] In addition to this, tellurium-based TMDs, such as $MoTe_2$, have also received extensive attention from researchers due to their unique physical and chemical properties. The temperature-induced phase transition properties between the 2H and 1T' phases achieved by $MoTe_2$, resulting in the transformation of the semiconducting and semi-metallic states, enable the modification of the electrical, optical, and mechanical properties of the material.[59,60] Therefore, when combined with the dimension of temperature, the perception space of artificial visual bionic systems can be expanded and closer to different practical application scenarios and actual biological system performance.[61]

### 2.3. Monoelemental 2D Materials

The three most widely recognized material systems in this category are Gr, phosphorus, and tellurium (Te). In terms of atomic structure, Gr consists of a single layer of carbon atoms, which are hybridized by $sp^2$ to form a hexagonal honeycomb lattice. Each carbon atom is bonded to three neighboring carbon atoms by covalent bonds, leaving one unpaired electron free to move in a $\pi$-orbital, forming a $\pi$-bond.[62] The difference is that the phosphorus atom forms a tetrahedral structure with its neighboring phosphorus atoms by $sp^3$ hybridization.[63] Te is usually a tetrahedral structure formed by $sp^3$ hybridization, but Te atoms are arranged differently than phosphorus ones. Te atoms form a helical layered structure with strong orientation through covalent bonds.[64]

With a unique Dirac-cone gapless energy band structure, Gr has very high electrical conductivity and carrier mobility. Due to the specificity of the bandgap and Dirac point, Gr will exhibit some exotic quantum effects when subjected to an external electric field, magnetic field, or light, such as the quantum Hall effect, negative magnetoresistance effect, etc. Gr plays three main roles in visual synaptic devices based on 2D materials: conductive electrodes, carrier trapping, and a portion of the conduction channel.[65,66] Chen et al. utilized monolayer Gr as the trapping layer to realize floating gate modulation. Photogenerated carriers are trapped by Gr through a tunneling effect, leading to a persistent photocurrent in the $ReS_2$ channel.[67] Although Gr has a very high carrier mobility, its light absorption efficiency is very low. Therefore, Gr is not suitable as a solo photoresponsive material. Guo et al. used Gr as the contact channel, while $\pi$-conjugated COFs were the photogating layer. Photoelectrocatalytic reactions in COF effectively modulated the Gr channel's carrier concentration and relaxation time (**Figure 6a**).[68] Gao's group adopted the Gr/$WSe_2$ heterojunction to realize positive and negative photoconductivity (PPC and NPC). Transformation of carrier types in Gr by synergistic modulation of voltage and light intensity (Figure 6b).[69]

As allotropes, black phosphorus (BP) and violet phosphorus (VP) are two of the most widely used phosphorus-based monoelemental 2D materials in current visual neuromorphic devices. Normally, the atoms of both black and violet phosphorus are $sp^3$ hybridized. However, each phosphorus atom in VP forms a triangular conical structure with three surrounding phosphorus atoms, and the stacking structure between different layers is different from that of BP.[70] Unlike TMDs, BP is a direct bandgap semiconductor regardless of the thickness. With excellent light absorption ability, high carrier mobility, and anisotropic properties, BP has great potential for optoelectronic applications.[71] Compared to BP, the advantages of VP are the absorption capacity in the visible light band and relatively better air stability.[72] VP retains the material advantages of BP, including anisotropy and broadband response. At the same time, it alleviates the shortcomings of BP, which is easily oxidized in the air environment.[73] Zhu et al. utilized the infrared absorption of BP and integrated the infrared photodetector unit with an in-memory computing unit. The whole visual system demonstrated object detection and recognition for the mid-wavelength infrared range (Figure 6c).[74] Instead, Shao et al. implemented PPC and NPC visual adaptation using BP and 0D perovskite quantum dots.[75] Liu et al. also used a device-integrated process to combine a VP-$MoS_2$ heterostructure and a single $MoS_2$ channel for VP application. The synaptic properties were realized, including over 60 dB dynamic range, 7-bit distinguishable conductance states, and electro–optical dependent plasticity. (Figure 6d).[76]

As a hot single-atom material in recent years, Te has shown great potential for applications in many fields, including catalysis, semiconductor devices, and photodetectors. Te typically exhibits a semi-metallic property at room temperature with high carrier mobility. Due to the narrow bandgap, Te has an excellent photoelectric response in the infrared spectral region. The 1D chain-like structure of its crystals also endows Te with anisotropy, demonstrating the ability for multimodal detection. Nguyen et al. fabricated an $Al_2O_3$-encapsulated Te/$ReS_2$ P–N junction to realize logical operations based on optoelectronic


© 2025 Wiley-VCH GmbH

16136829, 0, Downloaded from https://onlinelibrary.wiley.com/doi/10.1002/smll.202503717 by City University Of Hong Kong, Wiley Online Library on [19/08/2025]. See the Terms and Conditions (https://onlinelibrary.wiley.com/terms-and-conditions) on Wiley Online Library for rules of use; OA articles are governed by the applicable Creative Commons License

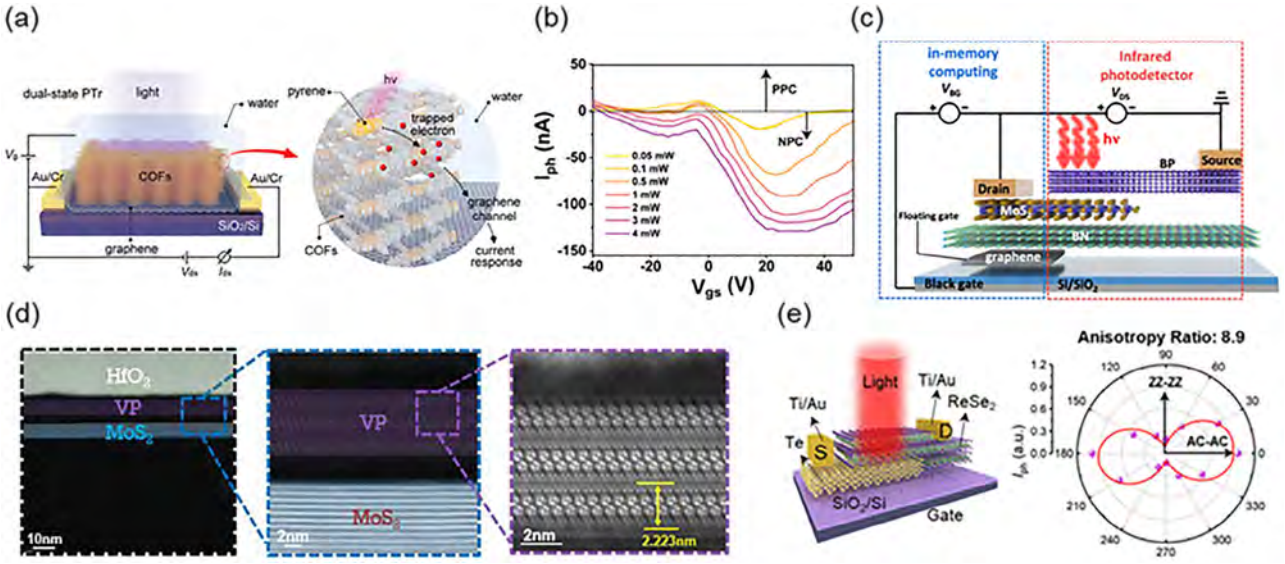


**Figure 6.** a) Schematic of the COF/Gr heterojunction and carrier transport for photoelectrocatalytic reactions.[68] Copyright 2024, Wiley-VCH. b) The bidirectional photocurrent with different light intensities and gate voltages.[69] Copyright 2024, Wiley-VCH. c) The device structure combines with the infrared photodetector and in-memory computing units.[74] Copyright 2024, Springer Nature. d) Cross-sectional HAADF scanning transmission electron microscope (STEM) images of the heterojunction.[76] Copyright 2023, Wiley-VCH. e) Schematic structure of a polarization-detecting heterojunction device and polar diagram of normalized photocurrent as a function of polarization angle.[78] Copyright 2025, American Chemical Society.

synergy, including inverter and AND/OR gates.[77] In the same materials structure, Chen et al. exploited the infrared detection properties and crystal anisotropy of Te to achieve a high anisotropy ratio detection (8.9) and broad spectral photoresponse (Figure 6e).[78]

### 2.4. MXenes

MXenes are a new class of 2D inorganic materials composed of transition metal carbides, nitrides, or carbon-nitrides with the general chemical formula $M_{a-1}X_aT_b$. MXenes have a layered structure similar to that of Gr, which could be regulated by the chemical and physical properties at the nanoscale level.[79] MXenes have good electrical conductivity, a large specific surface area, and abundant functional groups on the surface, and they have been widely used in photoelectrocatalysis.[80] The optoelectronic performance of MXenes has been a hot area of research in recent years. Specifically, MXenes can absorb a wide spectral range and prolong carrier lifetime due to their 2D structure and abundant surface groups. The narrower bandgap also contributes to the fast transport of photogenerated carriers. Chai's group used the MXene/VP vdW heterojunctions to construct the optoelectronic synapse for vision-olfactory crossmodal perception. The device realized the synaptic behaviors with only light pulses and responded in different humidity and gas conditions, which is highly relevant to the hydrophilicity and rich surface groups of MXene (**Figure 7**).[81]

The current strategies for realizing neuromorphic responses using MXene are generally divided into four categories: carrier trapping and de-trapping, energy band structure matching, interlayer ion transport, and metal filament formation.[82,83] For $Ti_3C_2T_x$-based devices, oxidation under air conditions and the formation of $TiO_2$ on the surface are unavoidable. Oxygen vacancies formed during oxidation can form photocarrier trapping sites to realize the carrier trapping and release process under different light illumination. Moreover, stimulated by only light irradiation, vacancies tend to cause a pronounced and persistent photoconductive effect. In addition to oxygen vacancies, surface groups, such as hydroxyl groups ($OH^-$), can also effectively modulate the photoconductivity of MXene-based devices. This charged group

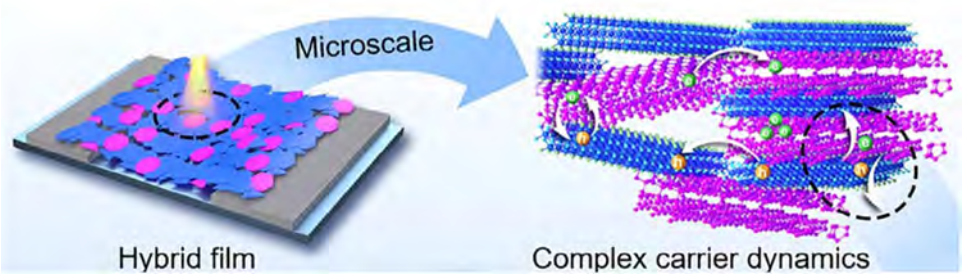


**Figure 7.** Schematic of MXene/VP hybrid films and photogenerated carrier transport.[81] Copyright 2024, Springer Nature.


© 2025 Wiley-VCH GmbH

16136829, 0, Downloaded from https://onlinelibrary.wiley.com/doi/10.1002/smll.202503717 by City University Of Hong Kong, Wiley Online Library on [19/08/2025]. See the Terms and Conditions (https://onlinelibrary.wiley.com/terms-and-conditions) on Wiley Online Library for rules of use; OA articles are governed by the applicable Creative Commons License

can accelerate the carriers' release process trapped by MXene vacancies, leading to rapid conductance reduction and breaking the persistent photoconductivity effect.[84] Therefore, the humidity, which is directly related to the density of $OH^-$, can also be an important stimulus source. Energy band design is an important strategy for optoelectronic neuromorphic devices. MXene's excellent conductivity implies a narrow bandgap with metallic or semi-metallic properties. In some neuromorphic device designs, it is often used as a carrier trapping layer to realize the effect of the floating gate. Chen's group utilized the $CsPbBr_3$-MXene hybrid floating gate layer to realize the long-term storage of optical signals in the organic channel.[85] In contrast to this strategy, Shen et al. introduced phenylsulfonic acid groups to change the bandgap of metalloid $Ti_3C_2T_x$ MXene. About 1.53 eV bandgap imparted semiconducting properties and broadband response to the device, showing potential in a flexible visual sensory–neuromorphic system.[86]

The multilayer structure of MXene is held together by vdW forces. The spacing of the layers can be dynamically changed by the humidity environment (water absorption), the type of groups, and other factors. Thus, driven by voltage, the layer-to-layer gap becomes a channel for ion movement, which makes the ion gate widely used in MXene-based neuromorphic devices.[87] By adjusting the relative magnitude of the gate and source–drain voltages, Zhang et al. induced ions to move and separate between the MXene layers, forming an electric double layer and regulating the ITO channel conductance.[88] Metal filament formation can be generally divided into vertical and planar structures. Like most top and bottom electrode memristors, forming Ag conducting filaments is an important working principle of the device. Among them, MXene was often required to form the channel with some oxide layer, such as $TiO_x$, $SiO_2$, $HfO_2$, etc.[89–91] Park's group realized the formation and annihilation of Cu conducting filaments on the surface of MXene. This planar two-terminal structure enabled gradual resistive switching dynamics under the principle of surface functional groups inducing the formation of a Cu-conducting channel.[92]

### 2.5. Perovskite

A large class of 2D perovskites consists of alternating stacks of inorganic metal halide octahedral layers and organic/inorganic spacer layers. The structure is derived from conventional 3D chalcogenides, where the 3D structure is separated into a 2D layered structure by introducing bulky organic cations.[93] The structure of 2D chalcogenides can be represented by the chemical formula $(RNH_3)_2MX_4$, where R stands for the organic cation. The typical structures include the Ruddlesden-Popper phase (RP phase) and the Dion-Jacobson phase (DJ phase). Compared with 3D structures, 2D perovskites have higher carrier mobility, better stability, and wider light absorption range, which are suitable for optoelectronic neuromorphic devices.[94] 2D Ruddlesden-Popper perovskite was adopted to fabricate the 2D artificial optoelectronic synapses for neuromorphic vision sensors. The synaptic device demonstrated an ultralow electrical power consumption of 0.145 fJ when triggered by a light spike (**Figure 8**a,b).[95] Recently, Kim et al. utilized the Dion-Jacobson 2D perovskite channel to achieve highly linear and symmetrical conductance changes. A $7 \times 7$ array demonstrated exceptional fabrication yield and minimal operational variability. 2D DJ-phase perovskite's advantage of environmental stability was fully utilized, showcasing impressive moisture resistance for up to 7 months.[96]

The other class of materials consists of oxides. The 2D oxide perovskites usually have a layered structure, and the chemical formula can usually be expressed as $A_{n-1}B_nO_{3n+1}$. For oxide 2D materials, both air and thermal stability are superior. Also, the persistent photoconductive effect due to oxygen vacancies is well-suited for some visual synaptic applications. Chen et al. prepared $Ca_2Nb_3O_{10}$ nanosheets using calcination–exfoliation to construct a flexible UV optoelectronic neuromorphic device (Figure 8c,d).[97] Wang et al. fabricated plane two-terminal devices with a 2D $CaTa_2O_7$ channel. UV illumination induced interfacial carrier trapping and modulated the activity of the metal conductive filaments inside the channel.[98]

### 2.6. Other Compounds

In addition to some of the material systems mentioned above, many interesting 2D materials have been synthesized and applied to in-sensor computing neuromorphic vision. Overall, the new material systems are designed to give unique optoelectronic properties to the devices.[99] Therefore, we will summarize some unique material systems here. The first thing to mention is bismuth oxyselenide ($Bi_2O_2Se$), exhibiting a tetragonal crystal structure with the I4/mmm space group.[100] The material has a stratified configuration characterized by the periodic stacking of cationic $[Bi_2O_2]^{2+}$ layers and anionic $Se^{2-}$ sheets along the crystallographic *c*-axis, forming an ordered heterostructure through electrostatic interlayer interactions.[101,102] A bandgap of ≈0.8 eV confers $Bi_2O_2Se$ semimetallic properties and demonstrates the potential to achieve high mobility. As photodetectors, $Bi_2O_2Se$-based devices possess three general mechanisms of operation, including the photoconductive effect, the photothermoelectric effect, and the bolometric effect.[100] Ren et al. used the $Bi_2O_2Se$ channel to fabricate a self-powered broadband optical synapse. The Se vacancy-induced persistent photoconductivity effectively mimicked the multiple visual responses (**Figure 9**a).[103,104] Moreover, the low symmetry crystal structure and the displacement of $Bi^{2+}$ ions make $Bi_2O_2Se$ a ferroelectric semiconductor material. This ferroelectric and optoelectronic coupling material presents new ideas for developing in-sensor computing visual devices (Figure 9b).[105] In addition to $Bi_2O_2Se$, 2D ferroelectric semiconductors include $CuInP_2S_6$ (CIPS) and $\alpha$-$In_2Se_3$. CIPS can be used both as a 2D ferroelectric channel material and as a strong room-temperature ferroelectric layer to modulate the transport properties of other materials.[106] Shang et al. fabricated the synaptic devices based on the CIPS channel. By modulating the out-of-plane ferroelectric polarization of channel materials, photogenerated carrier transport can be efficiently enhanced (Figure 9c,d).[107] Depending on the crystal structure, 2D $In_2Se_3$ has different material properties, including the paraelectric ($\beta$), ferroelectric ($\alpha$), and antiferroelectric ($\beta'$) phases.[108] Similar to previous material choices, materials in the ferroelectric phase have unique advantages in neuromorphic computation. Ferroelectric polarization, particularly the remanent polarization, provides a new dimension for regulating the channel state.[109] Yang's group utilized


© 2025 Wiley-VCH GmbH

16136829, 0, Downloaded from https://onlinelibrary.wiley.com/doi/10.1002/smll.202503717 by City University Of Hong Kong, Wiley Online Library on [19/08/2025]. See the Terms and Conditions (https://onlinelibrary.wiley.com/terms-and-conditions) on Wiley Online Library for rules of use; OA articles are governed by the applicable Creative Commons License

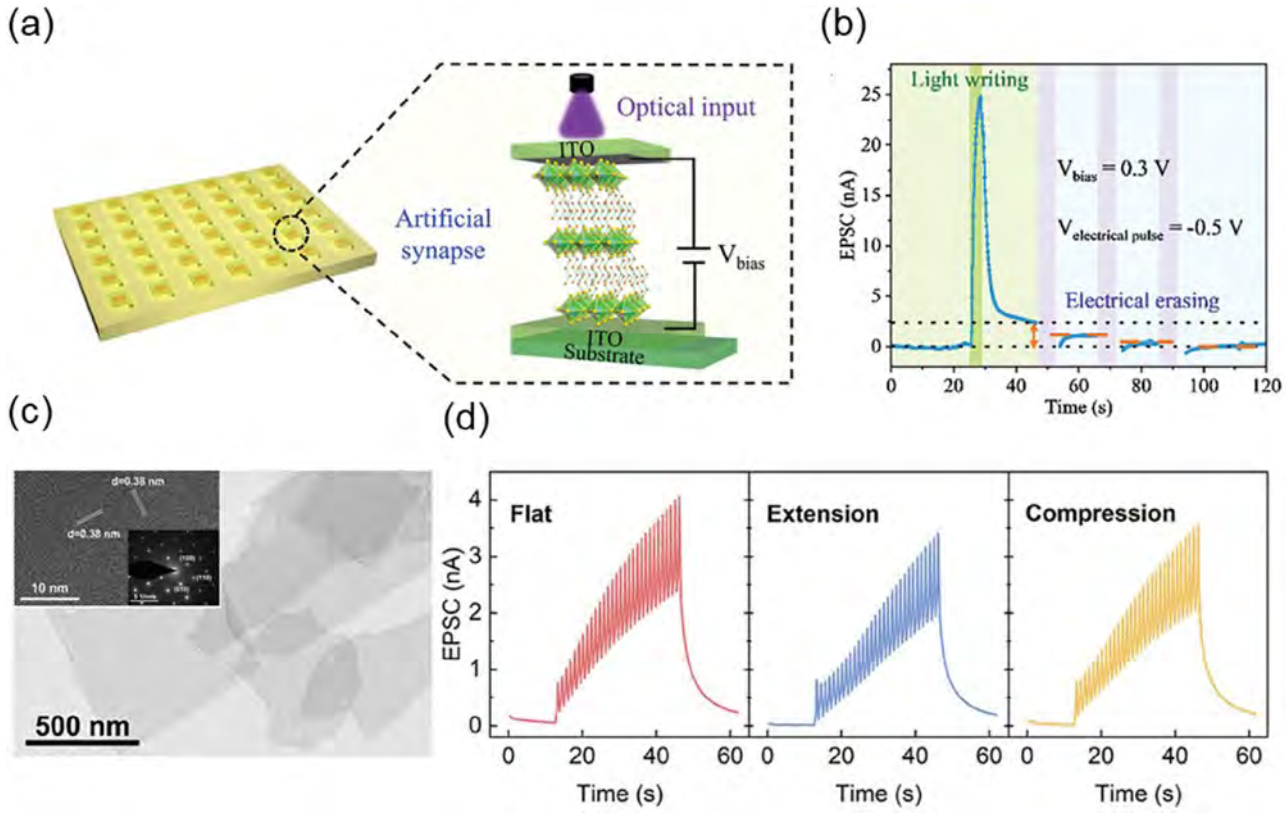


**Figure 8.** a) Schematic of the vertical device structure and array based on 2D perovskites.[95] Copyright 2024, Wiley-VCH. b) I–T curves for optical signal writing and electrical signal erasure of the device.[96] Copyright 2024, Wiley-VCH. c) The SEM image of the $Ca_2Nb_3O_{10}$ nanosheets, and the inset is the corresponding HRTEM image.[97] Copyright 2024, Wiley-VCH. d) UV response of flexible devices under different bending conditions.[97] Copyright 2024, Wiley-VCH.

the $\alpha$-$In_2Se_3$ channel for neuromorphic computing with optoelectronic coupling. Combined with the RC system, a high noise level recognition task and a temporal signal prediction task were completed.[110]

## 3. Working Mechanisms of Neuromorphic and Optoelectronic Visual Systems

State-of-the-art 2D material systems manifest atomic-level precision in layer engineering, coupled with gate-tunable quantum transport and programmable phase transitions. The absence of interlayer covalent bonding enables defect-suppressed heterointerfaces, a critical enabler for next-generation neuromorphic architectures. In order to better utilize the advantages of the material and to target the design of the device structure, multiple working mechanisms of artificial visual systems are studied.[111] Notably, the dangling bond-free nature of 2D heterostructures facilitates carrier transport across atomic interfaces, which is a prerequisite for super-fast and ultralow power consumption optical neuromorphic circuits.

### 3.1. Energy Band Engineering

Energy band engineering is currently one of the most effective means of realizing optoelectronic synapses. Currently, there are two main directions in the development of energy band engineering; one is to form different types of optoelectronic heterojunctions by combining different materials.[112] Photogenerated carriers are separated by the built-in electric field at the heterojunction and transported into the target material.[113] Generally, in order to prolong the carrier lifetime, the carrier recombination time is increased by corresponding material selection. In this structure, PN junction, Schottky junction, quantum well, superlattice, and so on are reported to be used in optoelectronic synaptic devices.[114] Another way to achieve modulation of carrier dynamics is to change the crystal structure of the channel to create a potential barrier in the homogeneous material. The main approaches are to introduce crystal deformation or asymmetric capacitive coupling. Li et al. utilized localized strain engineering to change the crystal structure of $Bi_2O_2Se$, causing differences in energy bands of homogeneous channels. The band structure of the suspended $Bi_2O_2Se$ channel area would bend upward, leading to the back-to-back built-in electric field. Combined with this flexoelectric effect, the visual synaptic behaviors were successfully realized.[115] Du et al. introduced the electrostriction effect into the $MoS_2$ channel. The semi-floating $MoS_2$ would produce lattice stretching under the source/drain (S/D) voltage regulation, resulting in a type-I heterojunction in the homogenous channel.[116]

A heterojunction structure can generally be divided into two categories according to the position of the electrodes relative to


© 2025 Wiley-VCH GmbH

16136829, 0, Downloaded from https://onlinelibrary.wiley.com/doi/10.1002/smll.202503717 by City University Of Hong Kong, Wiley Online Library on [19/08/2025]. See the Terms and Conditions (https://onlinelibrary.wiley.com/terms-and-conditions) on Wiley Online Library for rules of use; OA articles are governed by the applicable Creative Commons License

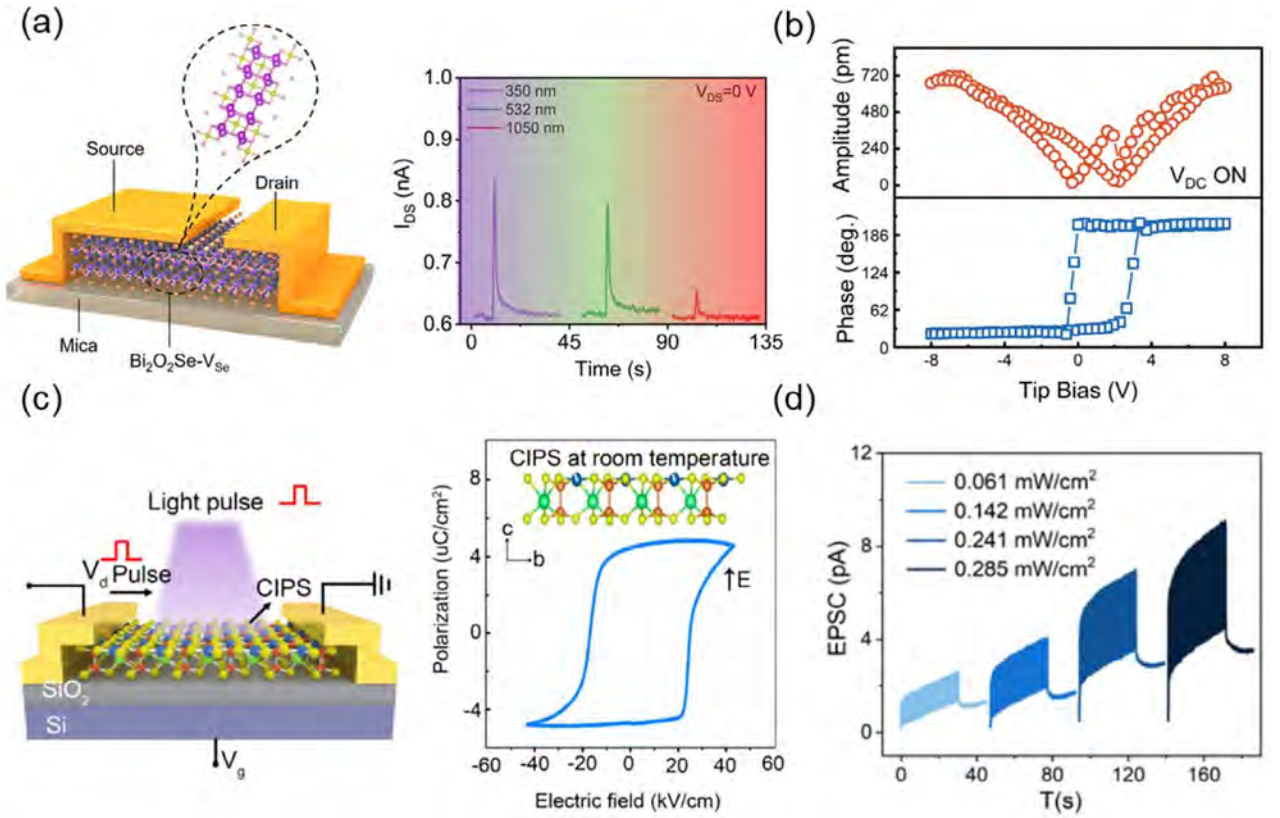


**Figure 9.** a) Schematic of the Se vacancy-doped $Bi_2O_2Se$ optical synaptic device and the self-power synaptic response.[103] Copyright 2024, American Chemical Society. b) Piezoelectric hysteresis loops with the application of a DC voltage to thin Bi2O2Se nanosheets.[105] Copyright 2023, Wiley-VCH. c) Schematic of optoelectronic synaptic devices based on ferroelectric 2D materials and the corresponding P–E hysteresis loop testing.[107] Copyright 2024, American Chemical Society. d) The synaptic photoresponse with different 450 nm light pulses.[107] Copyright 2024, American Chemical Society.

the channel. One type is where both S/D electrodes contact the same channel, and the other is where the electrodes contact separate materials.[117,118] Cao et al. combined $GeO_x$-coated MXene nanosheets with n-type solution-processed zinc tin oxide to construct a bulk heterojunction. The S/D electrodes were in direct contact with the hybrid film, and the multilevel energy band structure caused the transport and trapping of photogenerated carriers, prolonging carrier lifetime (**Figure 10a**).[119] Xu et al. used the methylammonium lead iodide ($MAPbI_3$) perovskite as the light absorption layer. The device realized bidirectional photoconductivity by modulating the energy band structure of the type-I heterojunction by gate voltage ($V_G$) (Figure 10b,c).[120] Moreover, the device preparation strategy of Zhang et al. was to use epitaxial growth to prepare a three-layer vertical structure (SnSe/InSe/GaN). GaN served as a substrate for epitaxial growth and as one end of the optoelectronic heterojunctions. By switching the material contacted by the S/D electrodes, the energy band structure of the acting heterojunction also changes, and different visual adaptation effects are realized.[121]

### 3.2. Trap State

Carrier trapping and de-trapping are widespread during the operation of optoelectronic devices. Carriers are bound by defect states in the material (e.g., impurities, lattice defects, surface states, etc.), making it difficult for photogenerated carriers to recombine.[122] 2D materials have many advantages regarding surface state and material properties, including a large surface-to-volume ratio, ultrathin structure, clean interface without dangling bonds, and high carrier mobility. However, some defects are inevitably introduced during material transfer and device preparation. Therefore, implementing the carrier trap and release process in a controlled manner is crucial for achieving visual neural devices.

Current approaches to achieving stable reconfigurable neuromorphic devices using trap and de-trap processes focus on introducing functional layer interfaces. As a necessary functional layer for three-terminal field effect transistor (FET) devices, the insulating layer is rich in surface states that provide the basic conditions for carrier trapping. From the utilization of $Al_2O_3$ to realize the interface trapping of carriers to the adoption of electron beam irradiation to realize the area trapping of photogenerated carriers, the oxide insulating layer has been widely used due to its surface defect state and strong dielectric effect (**Figure 11a**).[123] Due to this regional irradiation, photogenerated carrier trapping in the $SiO_2$ layer results in localized n-type doping in the $MoS_2$ channel, transforming its transport properties from isotropic to anisotropic (Figure 11b,c).[124] In addition to that, Chen et al. combined lattice strain engineering, anisotropic channeling, and


© 2025 Wiley-VCH GmbH

16136829, 0, Downloaded from https://onlinelibrary.wiley.com/doi/10.1002/smll.202503717 by City University Of Hong Kong, Wiley Online Library on [19/08/2025]. See the Terms and Conditions (https://onlinelibrary.wiley.com/terms-and-conditions) on Wiley Online Library for rules of use; OA articles are governed by the applicable Creative Commons License

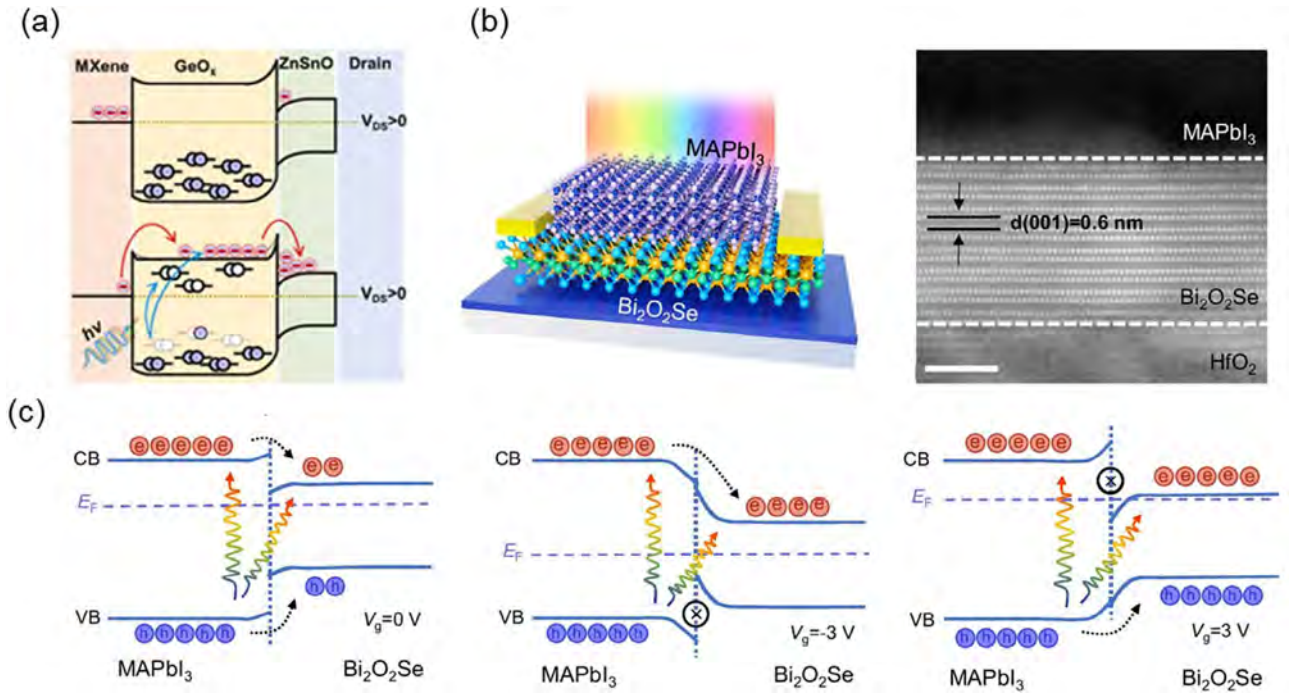


**Figure 10.** a) Schematic of the energy band diagram of the heterojunction and the corresponding carrier dynamics.[119] Copyright 2023, Elsevier. b) Schematic of the device structure with the perovskite light-absorbing layer and the corresponding cross-sectional HRTEM image.[120] Copyright 2024, Springer Nature. c) Structural changes and photogenerated carrier transport in type-I heterojunctions at different $V_G$.[120] Copyright 2024, Springer Nature.

insulating layer trapping with multiple modulation mechanisms. Wrinkled anisotropic $ReS_2$ channels were realized by preparing a patterned $Si_3N_4$ insulating layer. The wrinkled structure facilitated the photogenerated carrier trapping/de-trapping process at the $ReS_2$/dielectric layer interface, realizing reconfigurable and non-volatile behaviors of the devices (Figure 11d,e).[125] Tan et al. used the silicon-rich silicon nitride (sr-$SiN_x$) as the trapping dielectric layer for a broadband in-sensor computing visual system.[126] Although insulating layer materials have many conveniences and advantages, defects and insulating properties have contradictions and trade-offs. Therefore, some trapping functional materials can also be prepared as an interpolation layer between the insulating and the channel layers. Liu et al. used $PbI_2$ as a carrier trapping layer between $MoS_2$ and $SiO_2$ to realize the device's high storage performance and fast read/write speeds (Figure 11f).[127]

In general, the introduction of the trap state follows several main strategies. If the trap state is introduced above the channel material, it aims to realize the trapping effect on the photogenerated carriers. In this device structure, the carrier of the trap state can be some surface defect state, such as introducing some defects by plasma etching or using oxidation to generate a nanoscale oxide layer on the channel surface. It can also be some specific optical structures or some light-absorbing materials. For optoelectronic synapses, the surface trap functional layer should affect the optoelectronic performance of the channel material as little as possible. Therefore, introducing additional light-absorbing materials on the channel surface should be considered in terms of the coverage area, the light transmittance, and other factors. In this case, quantum dots and other micro-sized materials such as COF, MOF, and metal nanoparticles are good choices. If a trap state is introduced underneath the channel material, it is often desired to enable carrier trapping and release under the modulation of the $V_G$. As a classical carrier trapping material, oxides are widely used in optoelectronic neuromorphic devices because of their abundant defect states, wide bandgap (easier to form deep/shallow trap energy levels), and interfacial states generated upon contact with semiconductors. In addition, some materials prone to vacancy defects, such as Se- and I-chemicals, can serve as effective carriers of defective states. Moreover, lattice strain is also a means of generating carrier trapping for 2D materials, which are only a few nanometers thick. Fabricating repetitive microstructures using methods such as etching allows the 2D material channels to generate periodic strains. This strain alters the energy band structure of the corresponding channel, thus creating a periodic energy band change structure within the same channel, similar to the energy well structure of a superlattice.

For the analysis of trap state, rigorous controlled experiments are an effective way to verify it. By comparing the performance changes before and after the same device, it can be effectively seen whether the trap state is successfully introduced and functioning. For quantitative analysis, the effect of the defective state on the device performance can be visualized by testing the device's output and transfer characteristic curves under light and non-light conditions, including threshold voltage, saturation current, hysteresis window, and so on. The corresponding parameters can be extracted to calculate the defect density of the device's states and analyze carrier trapping. Certainly, density functional theory (DFT), as a first-principles computational method, also


© 2025 Wiley-VCH GmbH

16136829, 0, Downloaded from https://onlinelibrary.wiley.com/doi/10.1002/smll.202503717 by City University Of Hong Kong, Wiley Online Library on [19/08/2025]. See the Terms and Conditions (https://onlinelibrary.wiley.com/terms-and-conditions) on Wiley Online Library for rules of use; OA articles are governed by the applicable Creative Commons License

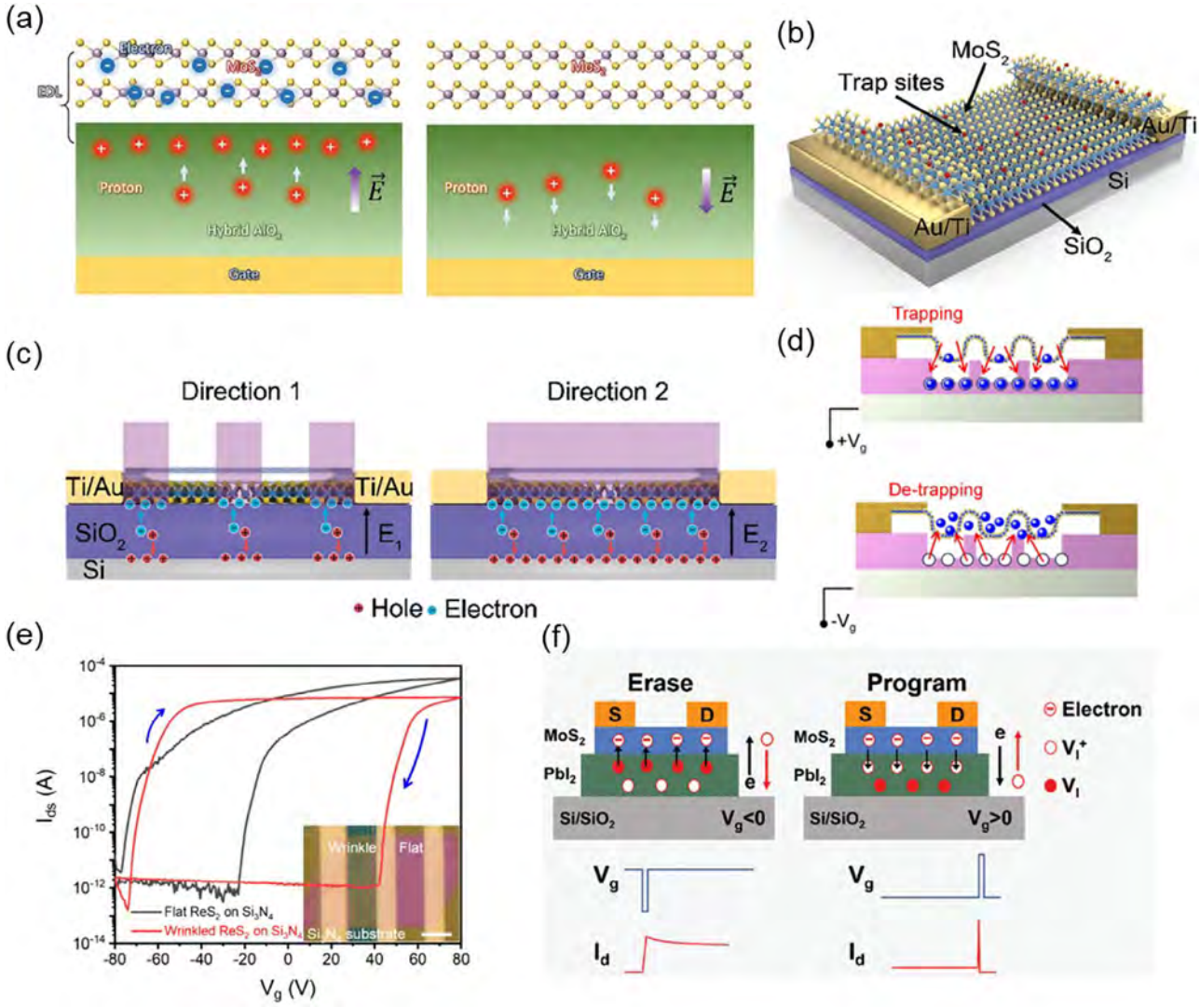


**Figure 11.** a) Charge trapping in the dielectric layer at different gate voltages.[123] Copyright 2024, Wiley-VCH. b) Schematic diagram of a device structure with ultraviolet/ozone-induced defects.[124] Copyright 2024, Wiley-VCH. c) Two different modes of the light-induced channel doping.[124] Copyright 2024, Wiley-VCH. d) Schematic of carrier trapping/de-trapping at the interface with the wrinkled structure.[125] Copyright 2024, American Chemical Society. e) Transfer characteristic curves for two different contact interfaces.[125] Copyright 2024, American Chemical Society. f) Carrier trapping and de-trapping processes in $PbI_2$ modulated by $V_G$.[127] Copyright 2024, Wiley-VCH.

allows for the direct computation and analysis of defect states, interface behavior, and capture centers in neuromorphic devices.

### 3.3. Floating Gate

Although it has similarities with the carrier trap in some processes, a floating gate is a charge storage structure. The charge can be retained for long time without easy leakage and has better storage stability. In phototransistor devices, the charge storage characteristics of the floating gate modulate the photovoltaic response. Therefore, to ensure the long-term stability of the carriers after the floating gate captures them, an insulating layer is generally required to isolate the floating gate from the channel material. Li et al. adopted the classical $ReS_2$/h-BN/Gr (channel/isolation/floating gate) floating gate device structure to realize photoelectrical hybrid modulations (**Figure 12**a).[128] The advantages of 2D materials are fully utilized in this device structure. The ultrathin structure, high carrier concentration, and clean interface allow the carriers to tunnel efficiently and rapidly through the BN isolation layer under voltage, resulting in low operation power consumption (±8 V/2 ms), long retention (>1000 s), and stable endurance (>1000 times). After the floating gate captured the carriers, the optoelectronic response of the channel was modulated accordingly, and the inheritance of the synaptic weight conductance also occurred. In addition to Gr, oxides can also be used as floating gate layers. Chai's group fabricated the oxide-stacked structure to serve as dielectric and floating gate layers. In this $Al_2O_3/HfO_2/Al_2O_3$ sandwich structure, the carriers were driven by the $V_G$ and light irradiation, tunneled through the


© 2025 Wiley-VCH GmbH

16136829, 0, Downloaded from https://onlinelibrary.wiley.com/doi/10.1002/smll.202503717 by City University Of Hong Kong, Wiley Online Library on [19/08/2025]. See the Terms and Conditions (https://onlinelibrary.wiley.com/terms-and-conditions) on Wiley Online Library for rules of use; OA articles are governed by the applicable Creative Commons License

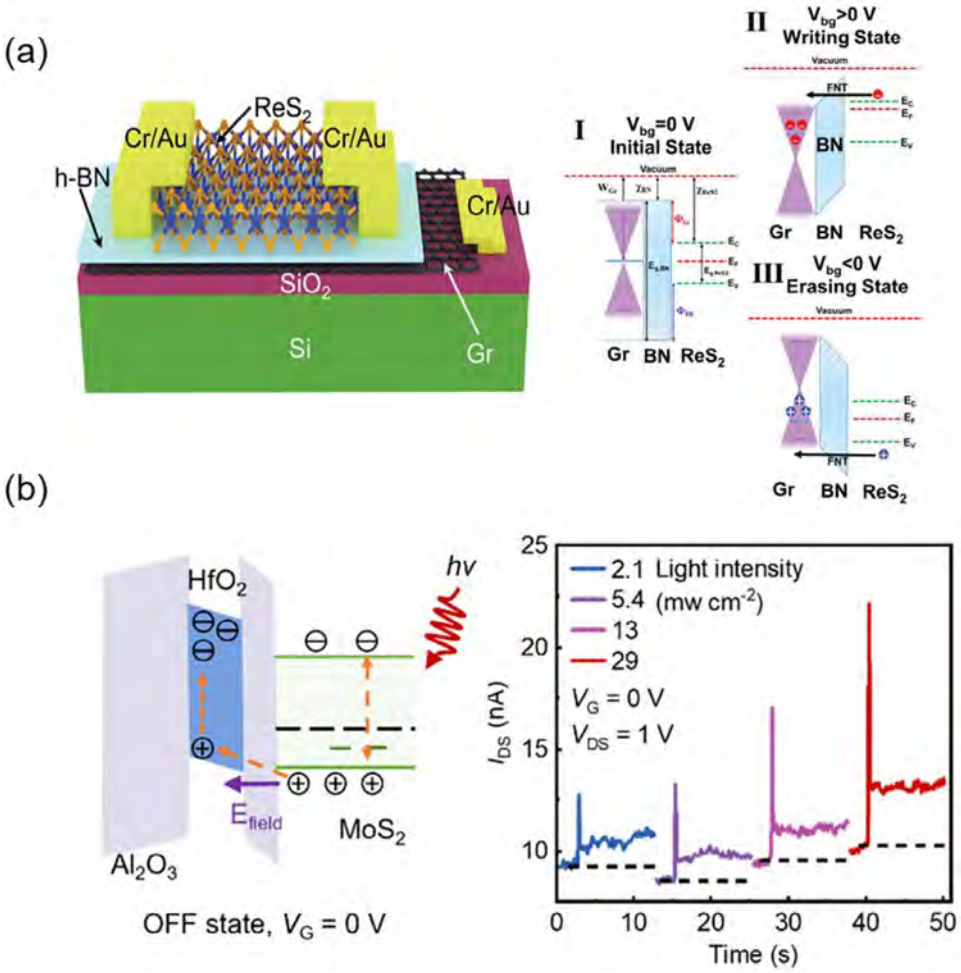


**Figure 12.** a) Structural schematic of the Gr floating gate-based device and $V_G$-regulated carrier tunneling floating gate modulation process.[128] Copyright 2024, Wiley-VCH. b) Schematic of the energy bands of the floating gate structure without applied $V_G$ regulation and the device response under different light illumination.[129] Copyright 2024, American Chemical Society.

$Al_2O_3$, and finally captured by $HfO_2$. Because the carriers preserved in the floating gate persist for a long time, the floating gate can still apply an electric field to the channel after the $V_G$ is removed, resulting in a different ground state (Figure 12b).[129]

### 3.4. Ferroelectric Polarization

The application of ferroelectric polarization in visual neural devices has received increasing attention, mainly because the unique properties of ferroelectric materials can mimic the behavior of neurons to a certain extent, providing different advantages from conventional materials.[130] Ferroelectric materials can exhibit spontaneous polarization in response to an applied electric field.[131] It can maintain this polarized state for a long time until the application of an opposing electric field reverses it. Here, coercive field and remanent polarization are the two important performance parameters to focus on. For different types of ferroelectric materials, a high coercive field means greater stability and higher immunity to interference. High remanent polarization indicates that the ferroelectric material remains strongly polarized after removing the external electric field. This property is similar to the "memory" ability of neurons. Therefore, ferroelectric materials provide an incomparably stable electrical regulation mechanism that enables more stable and effective optoelectronic coupling regulation.[132,133]

For visual synapses based on 2D materials, there are three general mechanisms of ferroelectric modulation. The first is the ferroelectric 2D semiconductor. As mentioned above, this class of materials is ideal for realizing low-complexity ferroelectric, optoelectronic modulated artificial vision chips because of the specificity of the lattice structure, which inherently possesses ferroelectric and semiconductor properties. Wu et al. selected $\alpha$-$In_2Se_3$ as the channel material to construct an in-sensor computing device (**Figure 13a**).[134] The room-temperature ferroelectric properties of the material allowed the channel conductance to continue accumulating in response to electrical pulses' stimulation. The ferroelectric polarization was also affected by light stimulation, and the excitatory post-synaptic current (EPSC) and relaxation time of the device increased significantly under progressively increasing light stimulation. In addition, stacking the 3R phase allows some materials that are not ferroelectric to achieve


© 2025 Wiley-VCH GmbH

16136829, 0, Downloaded from https://onlinelibrary.wiley.com/doi/10.1002/smll.202503717 by City University Of Hong Kong, Wiley Online Library on [19/08/2025]. See the Terms and Conditions (https://onlinelibrary.wiley.com/terms-and-conditions) on Wiley Online Library for rules of use; OA articles are governed by the applicable Creative Commons License

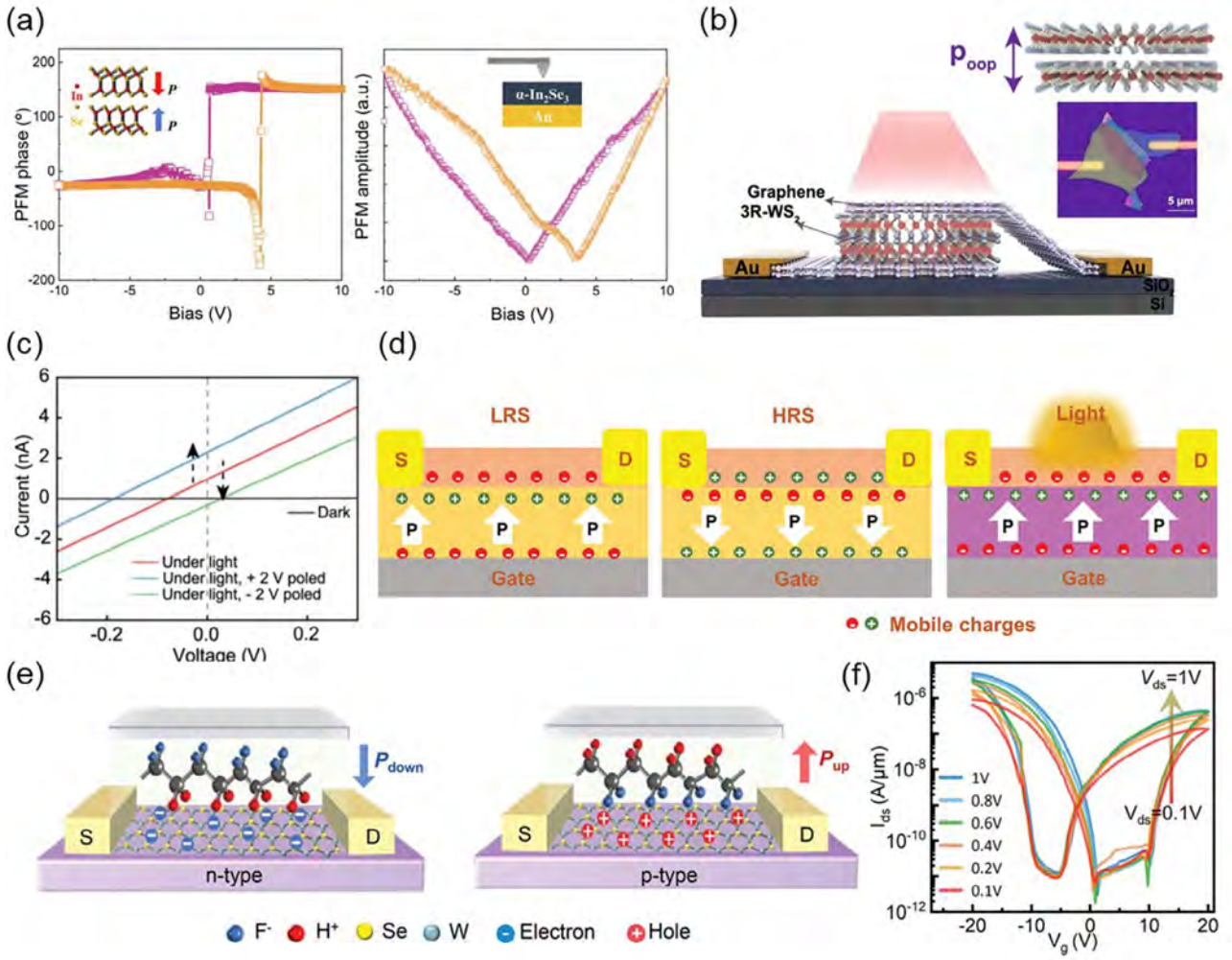


**Figure 13.** a) Piezoelectric force microscopy (PFM) phase and amplitude measured with the $\alpha$-$In_2Se_3$/Au structure.[134] Copyright 2024, Elsevier. b) Schematic of the device based on the Gr/3R-$WS_2$/Gr sandwich structure.[138] Copyright 2025, Springer Nature. c) The I–V curves for positive and negative photovoltaic effects under different poled voltages.[139] Copyright 2025, Springer Nature. d) Modulation of channel high/low resistance states and coupling with optoelectronic response using 2D ferroelectric materials.[139] Copyright 2024, Wiley-VCH. e) Schematic of thferroelectric polymer modulated bipolar channel.[140] Copyright 2022, Wiley-VCH. f) Transfer characteristic curves for bipolar devices with different $V_{DS}$.[140] Copyright 2022, Wiley-VCH.

slip-stacked ferroelectricity.[135–137] Gong et al. utilized the 3R stacked $WS_2$ to realize reconfigurable and nonvolatile ferroelectric bulk photovoltaics. Gr/3R stacked $WS_2$/Gr sandwich structure can modulate the contact barriers of Gr/semiconductor layers by changing the direction of the ferroelectric polarization, further enabling different built-in electric field and photocurrent directions (Figure 13b,c).[138] The second is using ferroelectric 2D materials to modulate other 2D channels. For such devices, the 2D ferroelectric layers must have a strong remanent polarization strength, a suitable coercive field, and a high Curie temperature. Wang et al. chose the CIPS as the 2D ferroelectric layer to modulate the 2D $SnS_2$ channel. The complete vdW contact device promoted the ability of ferroelectric regulation, leading to prolonged retention time (>$10^4$ s) and finer conductance changes (Figure 13d).[139] In particular, a ferroelectric optoelectronic reservoir computing system was introduced to realize high recognition accuracy. The last category is using other ferroelectric insulating layers to modulate 2D materials. This structure is consistent with a typical ferroelectric FET device. Chai et al. adopted classical ferroelectric polymer material, poly(vinylidene fluoride-co-trifluoroethylene) (P(VDF-TrFE)), to fabricate reconfigurable synaptic devices with $WSe_2$ channel (Figure 13e,f).[140]

The corresponding summarization of working mechanisms is shown in **Table 1**. We have added a summary of the arrayed devices here to demonstrate which material systems are easier to achieve large-area array-based fabrication.

## 4. Specific Neuromorphic Optoelectronic Response and Function

Machine vision uses computers and sensors to simulate a human visual system designed to acquire images or video data from a camera or other sensor and analyze it. With the continuous progress of computer technology, image processing algorithms,


© 2025 Wiley-VCH GmbH

16136829, 0, Downloaded from https://onlinelibrary.wiley.com/doi/10.1002/smll.202503717 by City University Of Hong Kong, Wiley Online Library on [19/08/2025]. See the Terms and Conditions (https://onlinelibrary.wiley.com/terms-and-conditions) on Wiley Online Library for rules of use; OA articles are governed by the applicable Creative Commons License

**Table 1.** The summary of optoelectronic synaptic devices with different working mechanisms.

| Compound | Working mechanisms | Multibit memory | Memory window | Working wavelength | Duration time | Array size | Refs. |
|---|---|---|---|---|---|---|---|
| $Ga_2O_3/MoS_2$ | Band engineering | LTP | / | 405 nm | 10 s | 16 × 16 | [113] |
| $Bi_2O_2Se$ | Band engineering | LTP | / | 405 nm | / | / | [115] |
| $MoS_2$ | Band engineering | / | / | 450–800 nm | / | / | [116] |
| $MoSe_2/MoS_2$ | Band engineering | 7 states | 5 V | / | $>10^4$ s | / | [117] |
| $CrSBr/PtS_2$ | Band engineering | LTP | 10 V | 365 nm | / | / | [118] |
| $ZTO/MXene/GeO_x$ | Band engineering | LTP | 2 V | 4450/520/660 nm | / | / | [119] |
| $MAPbI_3/Bi_2O_2Se$ | Band engineering | / | / | 300–1500 nm | / | 3 × 3 | [120] |
| SnSe/InSe/GaN | Band engineering | LTP | / | 365/532/800 nm | / | / | [121] |
| $MoS_2$ | Trap states | LTP | 4.9 V | / | 1000 s | / | [123] |
| $MoS_2$ | Trap states | LTP | 64 V | 400/480/650 nm | / | / | [124] |
| $ReS_2$ | Trap states | 16 states | 96.9 V | 473/532/635 nm | 1000 s | / | [125] |
| $MoS_2$ | Trap states | LTP | 5 V | 385/520/980 nm | 1000 s | 3 × 3 | [126] |
| $MoS_2/PbI_2$ | Trap states | 8 states | 120 V | / | $>10^4$ s | / | [127] |
| $ReS_2$/h-BN/Gr | Floating gate | LTP | 82 V | 532 nm | 1000 s | / | [128] |
| $MoS_2$ | Floating gate | LTP | 6 V | 660 nm | 2000 s | / | [129] |
| $\alpha$-$In_2Se_3$ | Ferroelectric polarization | LTP | 4.2 V | 450 nm | / | / | [134] |
| $MoS_2$ | Ferroelectric polarization | / | 6 V | / | / | / | [135] |
| $MoS_2$ | Ferroelectric polarization | LTP | 7 V | / | 10 years | / | [136] |
| $WS_2$ | Ferroelectric polarization | LTP | / | 445/525/623 nm | / | / | [138] |
| $SnS_2$/h-BN/CIPS | Ferroelectric polarization | LTP | 18.4 V | 359/457 nm | 10 years | / | [139] |

and hardware equipment, the development of machine vision has been speeding up and is being widely used in various industries. However, as the amount of data collected grows geometrically, large computing resources are urgently demanded. Near-sensor and in-sensor computing are the next major steps in solving machine vision problems. Near-sensor computing, where the processor is integrated near the sensor, is relatively easy to implement. This layout can reduce the data transmission distance, reduce the latency and bandwidth requirements, and realize partial data processing without sending all the data to the remote processing device.[141] In-sensor computing, on the other hand, is a higher-level implementation of near-sensor computing. Unlike the physical architecture, where the processing unit is adjacent to the sensor but independent of it, integrating the computing function directly inside the sensor can significantly reduce data transmission requirements and achieve ultrahigh performance and low power consumption.[142] Therefore, in order to further enhance the coupling of deep learning algorithms and device architectures, it is important to propose new training methods under new physical architectures with some special, integrated, bionic optoelectronic neuromorphic responses.[143]

### 4.1. Positive and Negative Photoconductivity

PPC and NPC are increasingly used in optical neural devices. Conventional silicon/III-V photodiodes tend to produce only positive photoconductance under light. While the switching of positive/negative photoconductance can lead to bi-directional modulation of synaptic weights in a single device, reducing device complexity and increasing hardware density. In fact, the two different photoconductivities mimic perceptual processes in the biological visual system. Optic rod and cone cells activate in response to light to convert photons into electrical signals. Horizontal cells regulate signaling between photoreceptors and bipolar cells through lateral connections to achieve signal suppression. Simulating the NPC and PPC responses in the biological vision system can improve the efficiency and accuracy of the device in perception, signal transmission, and data processing. Specifically, the synergistic effect of different photoconductivities can realize light adaptation and dynamic range adjustment, edge enhancement and feature extraction, pulse coding, and energy-saving computation, which are strongly related to in-sensor computing. Currently, the responsivity of negative and positive photoconductivity based on 2D materials has exceeded $10^4$ and $10^{10}$ A $W^{-1}$, much larger than the positive responsivity of conventional detectors in the visible/NIR band. Due to the low dark current and low defect state density of 2D devices, the detectivity of the devices can also exceed $10^{12}$ Jones.[144–146]

Numerous ways exist to realize NPC and PPC, including energy band engineering, changing carrier types, and doping.[147,148] Lin et al. fabricated $CeO_2/MoS_2$ heterojunction to realize bidirectional optoelectronic neuromorphic response. The choice of $MoS_2$-based heterojunction can effectively ensure the


© 2025 Wiley-VCH GmbH

16136829, 0, Downloaded from https://onlinelibrary.wiley.com/doi/10.1002/smll.202503717 by City University Of Hong Kong, Wiley Online Library on [19/08/2025]. See the Terms and Conditions (https://onlinelibrary.wiley.com/terms-and-conditions) on Wiley Online Library for rules of use; OA articles are governed by the applicable Creative Commons License

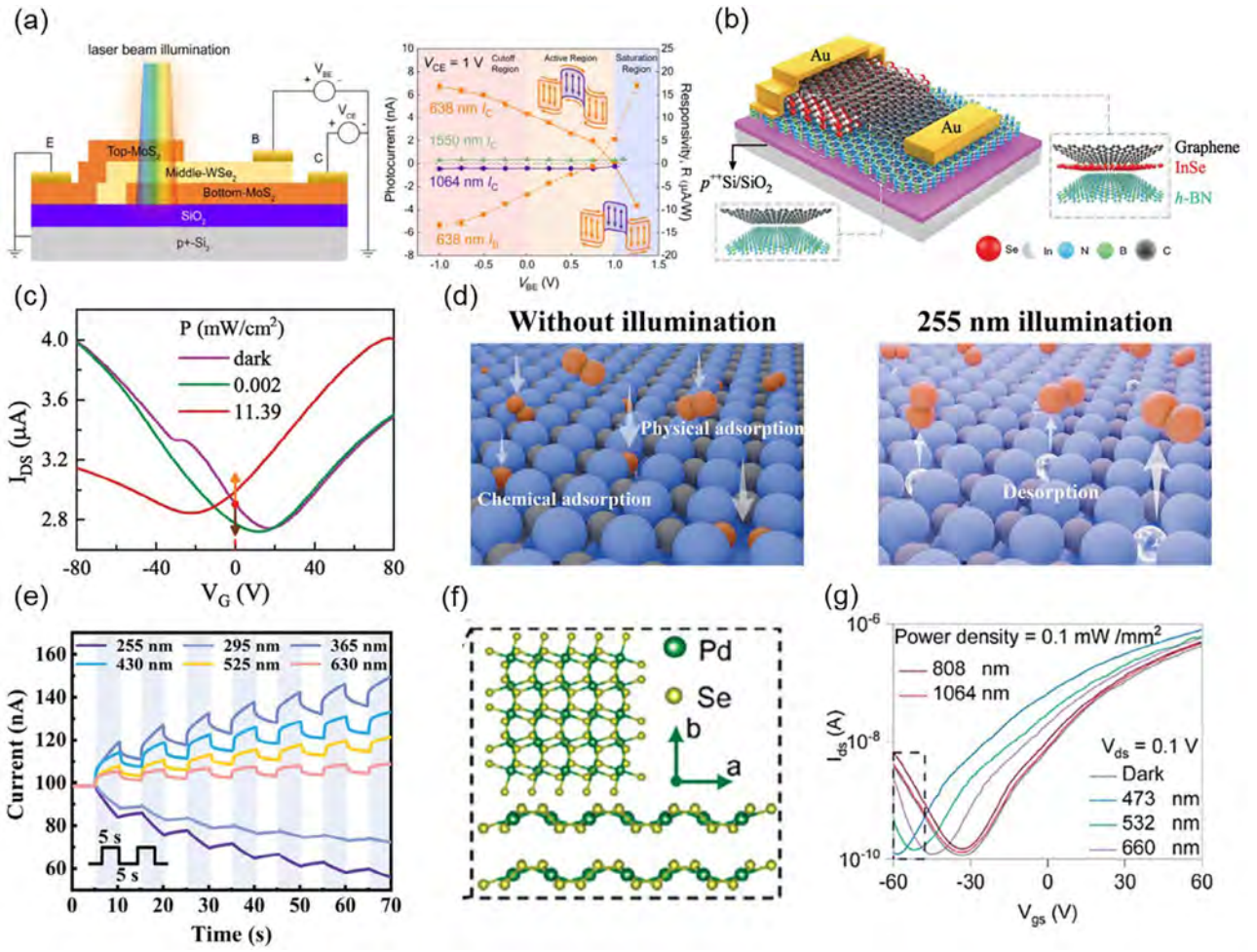


**Figure 14.** a) Schematic of a 2D stacked sandwich device structure and the corresponding photocurrent and responsivity regulated by the $V_{BE}$.[149] Copyright 2025, American Chemical Society. b) Schematic of the device structure and material.[150] Copyright 2024, Wiley-VCH. c) The transfer characteristic curves for NPC and PPC effects under different gate voltages and light intensities.[150] Copyright 2024, Wiley-VCH. d) Gas molecular adsorption and desorption processes by UV irradiation.[151] Copyright 2025, Wiley-VCH. e) NPC and PPC responsees under different wavelength irradiation.[151] Copyright 2025, Wiley-VCH. f) Anisotropic crystal structure of $PdSe_2$.[152] Copyright 2024, Wiley-VCH. g) NPC and PPC transfer characteristic curves under different $V_G$ conditions.[152] Copyright 2024, Wiley-VCH.

device's response in the visible wavelength band.[48] Zhu et al. introduced a sandwich structure based on $MoS_2/WSe_2/MoS_2$ for switching photoconductivity. The three metal electrodes contacted different layers of the sandwich structure and were defined as the emitter (E), base (B), and collector (C). The 638 and 1550 nm lasers produced PPC response in the presence of energy band structure, but the 1064 nm laser generated NPC response. Visible light had enough energy to produce photogenerated carriers and transport them across the energy band potential barriers. The heat from the 1550 nm light can also lead to the injection of hot electrons. However, only 1060 nm light can realize unidirectional photogenerated carrier separation and injection. Holes were continuously injected into the $WS_2$ base region, resulting in a decrease in photocurrent (**Figure 14a**).[149] As an important feature of Gr, electrons and holes can conduct in Gr channels. Therefore, different responses of NPC and PPC can be realized by injecting different types of carriers into the channel by electric field or heterojunction. Gao et al. fabricated the device based on the Gr channel, where the $V_G$ and InSe modulated channel carrier types. The increase or decrease of certain carriers in the Gr channel can be realized by controlling $V_G$ and light intensity (Figure 14b,c).[150] For some materials prone to generating vacancies or adsorbing gas molecules in the atmosphere, the NPC effect can be realized by introducing defects or doping on the surface. Liu et al. utilized the mechanism of gas adsorption and surface doping to realize NPC and PPC on the SnSe channel. The combined effect of Se vacancies and adsorption of oxygen molecules (act as electron acceptors to attract electrons) led to an increase in both hole concentration and carrier lifetime in the SnSe channel. When the UV laser irradiated the channel, it caused the desorption of oxygen molecules, and a large number of electrons entered the SnSe channel, resulting in NPC (Figure 14d,e).[151] Jiang et al. utilized a similar oxygen molecule adsorption/desorption mechanism to implement NPC and PPC switching on the $PdSe_2$ channel and achieved negative photoresponsivity of $-7.8 \times 10^3$ A $W^{-1}$ (Figure 14f,g).[152]


© 2025 Wiley-VCH GmbH

16136829, 0, Downloaded from https://onlinelibrary.wiley.com/doi/10.1002/smll.202503717 by City University Of Hong Kong, Wiley Online Library on [19/08/2025]. See the Terms and Conditions (https://onlinelibrary.wiley.com/terms-and-conditions) on Wiley Online Library for rules of use; OA articles are governed by the applicable Creative Commons License

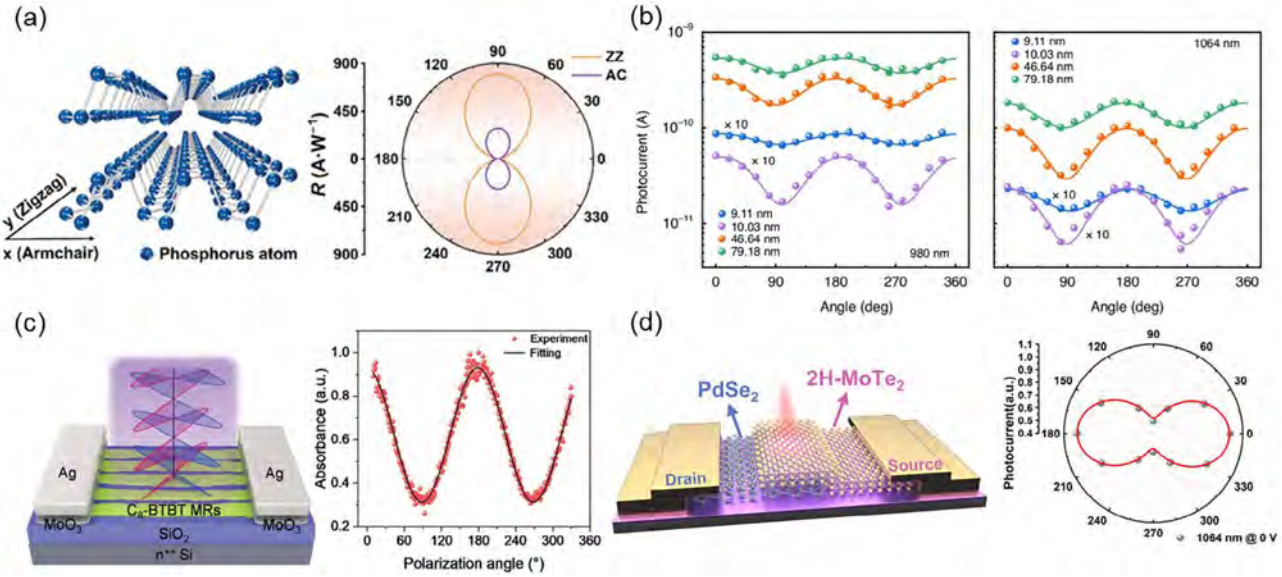


**Figure 15.** a) Crystal structure of BP, including both Armchair and Zigzag crystal orientations. Responsivity in polar coordinates with relation to crystal orientations.[155] Copyright 2024, Wiley-VCH. b) Photocurrent versus polarization angle of different thicknesses of $WSe_2$.[156] Copyright 2025, Springer Nature. c) Schematic of the device based on polarization detection of 2D organic small molecules and angle-dependent light absorption.[157] Copyright 2025, Wiley-VCH. d) Schematic of the device based on the heterojunction of crystalline anisotropic 2D materials and self-power polarization detection.[159] Copyright 2024, American Chemical Society.

### 4.2. Polarized Light Response

Machine vision aims to go beyond a single biological vision and perceive the external environment in all directions. Polarized light is widely present in nature and is perceived by many organisms other than humans. For example, bees use polarized light for navigation. Currently, the mainstream sensors are intrinsically isotropic and non-selective for polarized light, and generally require external polarizers or micromachined polarization arrays to achieve polarized light detection.[153] Meanwhile, polarized light detection is of unique significance in artificial visual synaptic devices, extending the dimensionality of traditional light sensing and providing a bionic vision system with multimodal information processing closer to biological perceptual capabilities. The reception of polarized light can enhance visual perception, such as distinguishing surface features and enhancing object contrast in hazy, complex lighting conditions. At the same time, after integrating the information processing unit, the angle information brought by polarized light can construct a detailed 3D space.[154] Therefore, polarized light detection is an important performance index for in-sensor computing visual systems. 2D materials have unique advantages in the field of polarized light detection. Some anisotropic 2D materials effectively resolve polarized light at different angles.[70] BP, highlighted in the previous monoelemental 2D materials section, is one of the star materials for polarization detection. Hao et al. utilized BP to fabricate polarized photodetectors with a polarization ratio (PR) of 118.4 (**Figure 15a**).[155] Liu et al. integrated the amplification and polarization-sensitive units into one broadband polarization detection system. $MoS_2$-based FET could amplify signals from $WSe_2$-based infrared polarization detectors (Figure 15b).[156] In addition to inorganic materials shining, organic single crystals also show potential for applications in the polarization field.[32] Pan et al. fabricated biomimetic polarization-sensitive organic phototransistors based on C8-BTBT single crystal with a high dichroic ratio (DR) of over $10^5$ (Figure 15c).[157] Although BP and 2D organic single crystals have performance advantages in polarization detection, weak air stability still poses a big problem in subsequent applications. Thus, a heterojunction is an effective means of combining the characteristics of different materials. The folded structure of $PdSe_2$ breaks the crystal symmetry, resulting in optical and electrical anisotropy. 2D polarized heterojunction detectors with varying performance characteristics can be prepared by combining $PdSe_2$ with other 2D materials.[158] Che et al. utilized $PdSe_2/MoTe_2$ heterojunction to prepare a self-powered broadband photodetector with linear and circular polarized light detection capability. The built-in electric field at the heterojunction interface conferred a polarized optical response to the device under self-power conditions (Figure 15d).[159] In addition to the material, breakthroughs can also be sought in preparation. Deng et al. prepared the $MoS_2$/Gr planar heterojunction by curling it into a 3D heterojunction. The 3D resonant microcavity structure allowed the material, which is not inherently polarization-detectable, to achieve a polarization response and a series of visual synaptic behaviors.[160]

### 4.3. Multi-Spectrum Selection

In multi-spectrum selection, the response range is an important basis. Mainstream complementary metal-oxide-semiconductor (CMOS) image sensors are limited by the silicon bandgap and operate in a wavelength range from about the visible to the end of the NIR. In contrast, various 2D materials, such as BP, can cover a wider range of wavelengths, which can detect the NIR to the mid-IR.[153] Meanwhile, the heterojunction structure


© 2025 Wiley-VCH GmbH

16136829, 0, Downloaded from https://onlinelibrary.wiley.com/doi/10.1002/smll.202503717 by City University Of Hong Kong, Wiley Online Library on [19/08/2025]. See the Terms and Conditions (https://onlinelibrary.wiley.com/terms-and-conditions) on Wiley Online Library for rules of use; OA articles are governed by the applicable Creative Commons License

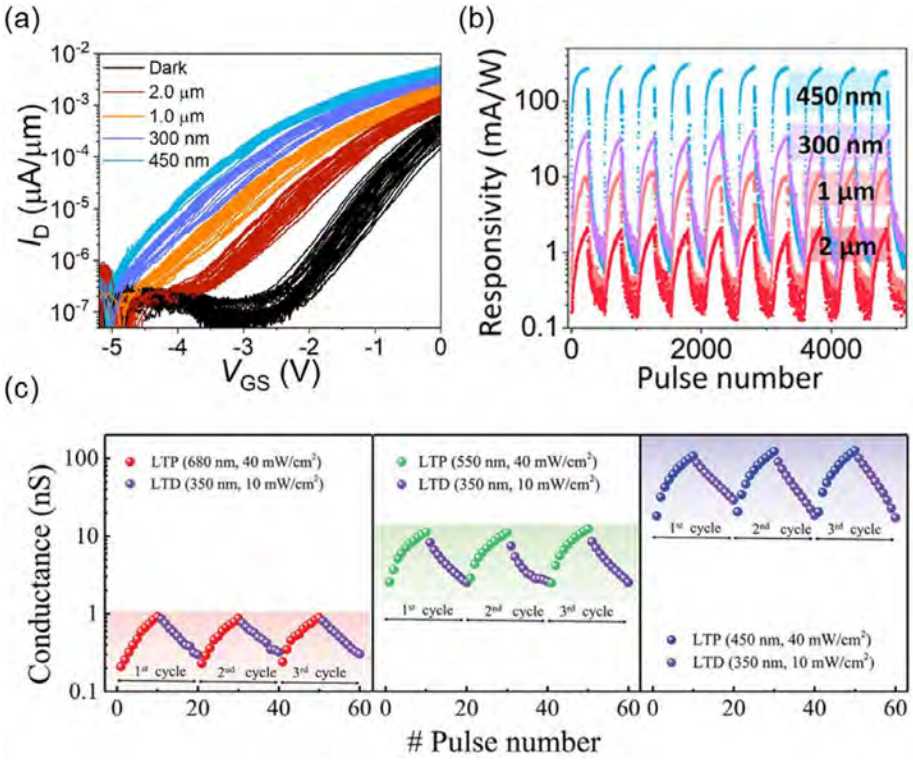


**Figure 16.** a) Spectrally selective transfer characteristic curves under different light stimuli.[163] Copyright 2024, Springer Nature. b) Visual neuromorphic response with significant wavelength correlation.[164] Copyright 2022, American Chemical Society. c) Significant conductance differences in LTP are realized in different wavelengths of visible light.[167] >Copyright 2025, Wiley-VCH.

based on 2D materials can extend the detection band further. The bandgap of 2D materials can often be tuned by the number of layers, stress, or electric field; this property gives 2D devices potential for multi-band imaging or tunable spectral detection.[161] For a single device, spectrally selective characterization is achieved by perceiving and processing optical signals in different wavelength ranges. The strong response to a certain wavelength band can significantly enhance the visual neural device's specific perception ability, computational efficiency, and adaptability in complex environments. Significant advantages in some special application scenarios, such as feature recognition in complex environments and strong interference conditions. Spectrally selective devices have broad application potential in the multispectral artificial retina, multispectral fusion sensing, feature enhancement, material identification, cancer screening, etc. 2D materials exhibit significant advantages in spectral selection due to their unique atomic-level thickness and electronic structure. The bandgap properties of 2D materials, including direct/indirect bandgap and bandgap width, can be tuned by thickness. In the meantime, the selective enhancement of certain band identification can also be realized by preparing heterojunctions with expanded response bands. Sun's group introduced a floating-gate heterojunction structure to enhance short-wavelength light perception in visual synaptic devices. Only photons carrying sufficient energy can excite photogenerated carrier tunneling and be captured by the floating gate, resulting in a spectral distinction.[162] Roy's group provided another idea for spectral selection. The infrared-sensitive $PtTe_2$/Si was the gate electrode and integrated into the optoelectronic synaptic device based on the $MoS_2$ channel. When infrared light irradiated the device, $PtTe_2$/Si acted as an infrared sensing unit, generating electron–hole pairs, resulting in a photogating effect. Slow carrier recombination can apply a slowly decaying voltage to the channel, modulating the conductance in the $MoS_2$ channel. When UV light irradiated the device, $MoS_2$, an excellent optoelectronic material, would sense and produce a stronger response (**Figure 16**a,b).[163,164] In summary, in order to achieve spectral selection, enhancement of the perception for specific band light can be achieved by material selection, for example, by selecting a 2D material with a relatively large bandgap.[165,166] It is also possible to enhance the response to a particular band using different sensing units or operating principles. Finally, there are other approaches, such as introducing nano-antennas or grating structures on the surface of 2D materials to enhance the absorption of specific wavelengths using surface plasmon resonance (Figure 16c).[167]

The corresponding summarization of specific neuromorphic optoelectronic response is shown in **Table 2**. For responsivity and detectivity, the positive value represents PPC and the negative value represents NPC.

## 5. The Applications of 2D Artificial Optoelectronic Synapses

Recent years have witnessed remarkable advancements in artificial intelligence (AI), with algorithmic innovations progressing


© 2025 Wiley-VCH GmbH

16136829, 0, Downloaded from https://onlinelibrary.wiley.com/doi/10.1002/smll.202503717 by City University Of Hong Kong, Wiley Online Library on [19/08/2025]. See the Terms and Conditions (https://onlinelibrary.wiley.com/terms-and-conditions) on Wiley Online Library for rules of use; OA articles are governed by the applicable Creative Commons License

**Table 2.** The summary of optoelectronic synaptic devices with different specific responsse.

| Compound | Responsivity | Working wavelength | Specific response | Detectivity [Jones] | Refs. |
|---|---|---|---|---|---|
| $CeO_2/MoS_2$ | / | 520/580/620 nm | PPC/NPC | / | [48] |
| $MoS_2$/h-BN/$PdSe_2$ | / | 520/1550 nm | PPC/NPC | / | [147] |
| $MoS_2$/Ge | 24.9/−0.4 A $W^{-1}$ | 532/1550 nm | PPC/NPC | $7.9 \times 10^{11}$/$-1.3 \times 10^{10}$ | [148] |
| Gr/InSe/h-BN | 13/$-1.1 \times 10^4$ A $W^{-1}$ | 405/637 nm | PPC/NPC | / | [150] |
| SnSe | / | 365/430/525/630 nm | PPC/NPC | / | [151] |
| $PdSe_2$ | 181/$-7.8 \times 10^3$ A $W^{-1}$ | 473/1064 nm | PPC/NPC | $5.2 \times 10^{10}$/$-2.3 \times 10^{12}$ | [152] |
| BP | 802.42 A $W^{-1}$ | 615–865 nm | Polarized light response | / | [155] |
| $WSe_2$/ $MoS_2$ | / | 980/1064 nm | Polarized light response | / | [156] |
| C8-BTBT | $1.6 \times 10^5$ A $W^{-1}$ | 365 nm | Polarized light response | $1.66 \times 10^{13}$ | [157] |
| $PdSe_2/NbSe_2$ | 27 mA $W^{-1}$ | 405–980 nm | Polarized light response | $9.8 \times 10^7$ | [158] |
| $PdSe_2/MoTe_2$ | 243 mA $W^{-1}$ | 375–2200 nm | Polarized light response | $6.46 \times 10^{10}$ | [159] |
| $Gr/MoS_2$ | $10^5$ A $W^{-1}$ | 395/590/660 nm | Polarized light response | $4.59 \times 10^{11}$ | [160] |
| $WSe_2$-GaN | / | 310/405/532/655 nm | Multi-spectrum selection | / | [162] |
| $PtTe_2/MoS_2$ | / | 300 $nm^{-2}$ μm | Multi-spectrum selection | / | [163] |
| $TeSeO_x$ | 1500 A $W^{-1}$ | 365/565/660 nm | Multi-spectrum selection | / | [165] |

at an unprecedented pace. While these software-based developments continue to transform various aspects of human society, significant challenges persist in hardware implementation, constrained by fundamental physical limitations of conventional computing architectures. Emerging as a promising solution, neuromorphic engineering draws inspiration from biological neural networks to develop novel computing paradigms. This approach fundamentally differs from von Neumann's architectures by implementing in-memory computing strategies that effectively mitigate the memory–processor bottleneck through integrated storage and processing capabilities. The development of artificial synaptic devices capable of weight modulation via optoelectronic stimulation demonstrates particular potential, mimicking neuroplasticity mechanisms observed in biological systems. Such adaptive characteristics enable hardware-level learning and information retention, positioning neuromorphic technologies as critical enablers for next-generation computing applications spanning intelligent robotics, autonomous systems, and neuroprosthetic interfaces.

### 5.1. Logic Operation

Under the von Neumann architecture, logical operations, AND, OR, NOT, and XOR, remain indispensable as the cornerstone of binary data processing, enabling decision-making, arithmetic computations, and precise control in digital systems. Deeply rooted in classical Boolean algebra, these operations underpin hardware functionality and algorithmic execution, from register manipulation to memory management.[168] However, as computing architectures evolve beyond traditional paradigms, the integration of logic operations with neuromorphic devices emerges as a promising pathway to reconcile energy efficiency with computational scalability. Neuromorphic systems, inspired by biological neural networks, inherently adopt an event-driven model, activating computations only upon receiving input pulses, a stark contrast to the continuous clock-driven mechanisms of conventional logic circuits.[169] This paradigm shift minimizes redundant energy expenditure while enabling asynchronous, parallel processing across distributed neurons and synapses. Such parallelism not only realizes the brain's capacity for concurrent task execution but also amplifies computational throughput for real-time complex problems.

Visual neuromorphic devices can produce pronounced conductance changes in response to light signals based on $V_G$ modulation. Therefore, the implementation of logical operations is generally divided into optoelectronic co-stimulation or stimulation with different wavelength lights. The core idea is the specificity of the device's response to stimuli. Optoelectronic synergistic logic operations are generally relatively common because most devices have large differences in conductance changes modulated by optical and electrical stimuli, respectively (**Figure 17a**).[170] Nguyen et al. utilized 450 nm laser light and $V_G$ to realize different logic operations based on a 2D Te/$ReS_2$ device. Synergistic logical operations of AND and OR were realized by varying the stimulus intensity.[77] Similarly, Sahu et al. also took advantage of the property that ultrathin 2D materials are sensitive to $V_G$ modulation. They combined it with UV light stimulation to realize two logic operations based on the $MoS_2$ channel.[171] For devices with only optical inputs, the spectrum-selective property is an important mechanism for realizing all-optical logic operations (Figure 17b).[172] Three all-optical logic operations modulated by infrared and visible light using the NPC and PPC effects of $PdSe_2$ in an air environment were realized.[152] Sun's group constructed an asymmetric ferroelectric heterostructure based on $MoS_2$ channels, half of which comprised $MoS_2$/CIPS. The devices showed conductance responses of different intensities to UV and visible light stimuli, realizing logical operations of AND and OR. With an external triboelectric nanogenerator input module, NOR and NAND logic operations can also be realized (Figure 17c,d).[173] Introducing ferroelectric regulation is also an important idea for realizing complex logic. Wang et al. also fabricated a 2D ferroelectric optoelectronic transistor and introduced two different visible lights to realize OR and AND operation under $V_G$ modulation.[49]


© 2025 Wiley-VCH GmbH

16136829, 0, Downloaded from https://onlinelibrary.wiley.com/doi/10.1002/smll.202503717 by City University Of Hong Kong, Wiley Online Library on [19/08/2025]. See the Terms and Conditions (https://onlinelibrary.wiley.com/terms-and-conditions) on Wiley Online Library for rules of use; OA articles are governed by the applicable Creative Commons License

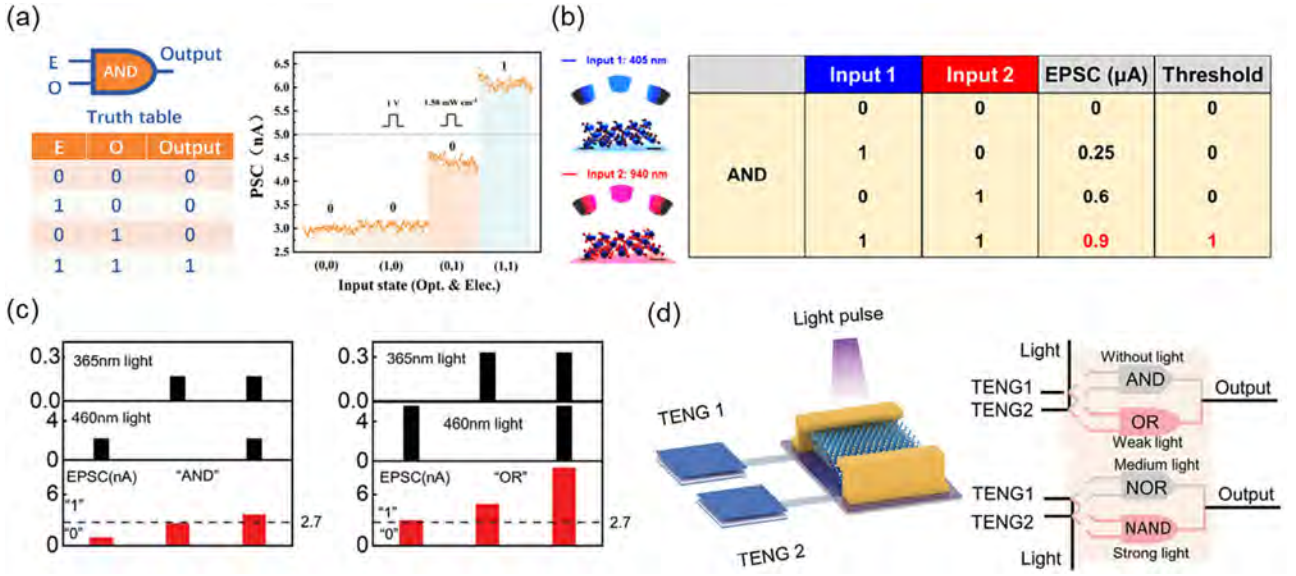


**Figure 17.** a) A truth table for AND logic gates and a current realization that relies on electrical and optical responses.[170] Copyright 2023, Wiley-VCH. b) AND logic operation was realized by using two different light irradiations.[172] Copyright 2024, American Chemical Society. c) Logic operation of AND and OR by combining visible and UV light.[173] Copyright 2024, Wiley-VCH. d) With two TENGs connected, the hybrid perception device can realize four types of logic operations.[173] Copyright 2024, Wiley-VCH.

### 5.2. Image Recognition

Visual perception emerges as a dominant channel for environmental interpretation across diverse species in the intricate tapestry of life's sensory systems. From the compound eye mosaics of flying insects to the binocular precision of raptors, organisms have evolved sophisticated optical mechanisms to decode light patterns into survival-critical data.[174] Depending on the environment in which they live, different biological systems evolve visual perception systems that are biased toward different abilities. Abyssal organisms, for example, have a spectral sensitivity biased toward blue bioluminescent wavelengths, and their tubular eyes maximize photon capture in the dark. Humans derive more than 80% of their information from the visual system. The mammalian cerebral cortex spends more than 30% of its time on visual processing, a neural investment that exceeds all other senses combined.[175,176] Thus, the reception of light information is not just an observation but a fundamental framework for ecological interaction and evolutionary success.

Image perception is dividing an image into multiple pixel points, with each device taking on the task of sensing one pixel point. Image perception is dividing an image into numerous pixel points, with each device taking on the task of sensing one pixel point. Therefore, the two-terminal structure of the upper and lower electrodes has an advantage in large-area arraying. Shen's group fabricated a $MoS_2$/ZnO vertical heterojunction for the flexible optoelectronic visual system. The 25 × 10 device array demonstrated the efficient storage of light signals with different intensities, frequencies, and exposure times.[177] Similarly, Kumar et al. adopted a solution to prepare a vertical two-terminal device based on the $MoS_2$ channel. The devices showed superior signal storage capacity under optoelectronic synergistic modulation.[178] In general, heterojunction is a typical strategy for this class of devices to realize signal sensing and storage functions.[179] Wang et al. targeted the mid-infrared band, which is difficult for the human eye to recognize. Signals in the infrared band were visualized using AsP and $MoTe_2$ heterojunction (**Figure 18a,b**).[180] The strategy of Huang et al. was to introduce discontinuous $NbS_2$ capture centers on the $MoS_2$ channel surface. Photogenerated carrier trapping realized efficient optical information storage in 10 × 10 $MoS_2$ arrays (Figure 18c).[181] Lee et al. utilized the metal vacancy between $LaAlO_3/SrTiO_3$ heterostructures to realize the efficient trapping of photogenerated carriers. Switching from short-range to long-range memory was realized by adjusting the ratio of components, and image memory was then realized in a 5 × 5 synapse array (Figure 18d).[182] In addition, some complex device structures can be introduced to realize the coupling with other functions. Zhang et al. proposed an artificial visual perception and recognition system based on the fusion of 2D heterojunction and plasma enhancement techniques. Ag nanograting's localized surface plasmon resonance effect enhances the device's optoelectronic response and dynamic range (180 dB).[183] Chen et al. even directly fabricated the device shape into a fiber to realize the integration with a wearable visual sensing system. The $TiO_{2-x}$ and $MoS_2$ arrays, which are directly grown on flexible carbon nanotube fiber, realized effective recognition and memory of ultraviolet signals through carrier separation of heterojunctions.[184]

### 5.3. Hybrid Perception System

Multimodal perception is realized on the one hand from the material's properties, exploiting the material's ability to perceive the specificity of information in different dimensions. On the other hand, it combines different external circuits and integrates some other components to realize the coupling of optoelectronic


© 2025 Wiley-VCH GmbH

16136829, 0, Downloaded from https://onlinelibrary.wiley.com/doi/10.1002/smll.202503717 by City University Of Hong Kong, Wiley Online Library on [19/08/2025]. See the Terms and Conditions (https://onlinelibrary.wiley.com/terms-and-conditions) on Wiley Online Library for rules of use; OA articles are governed by the applicable Creative Commons License

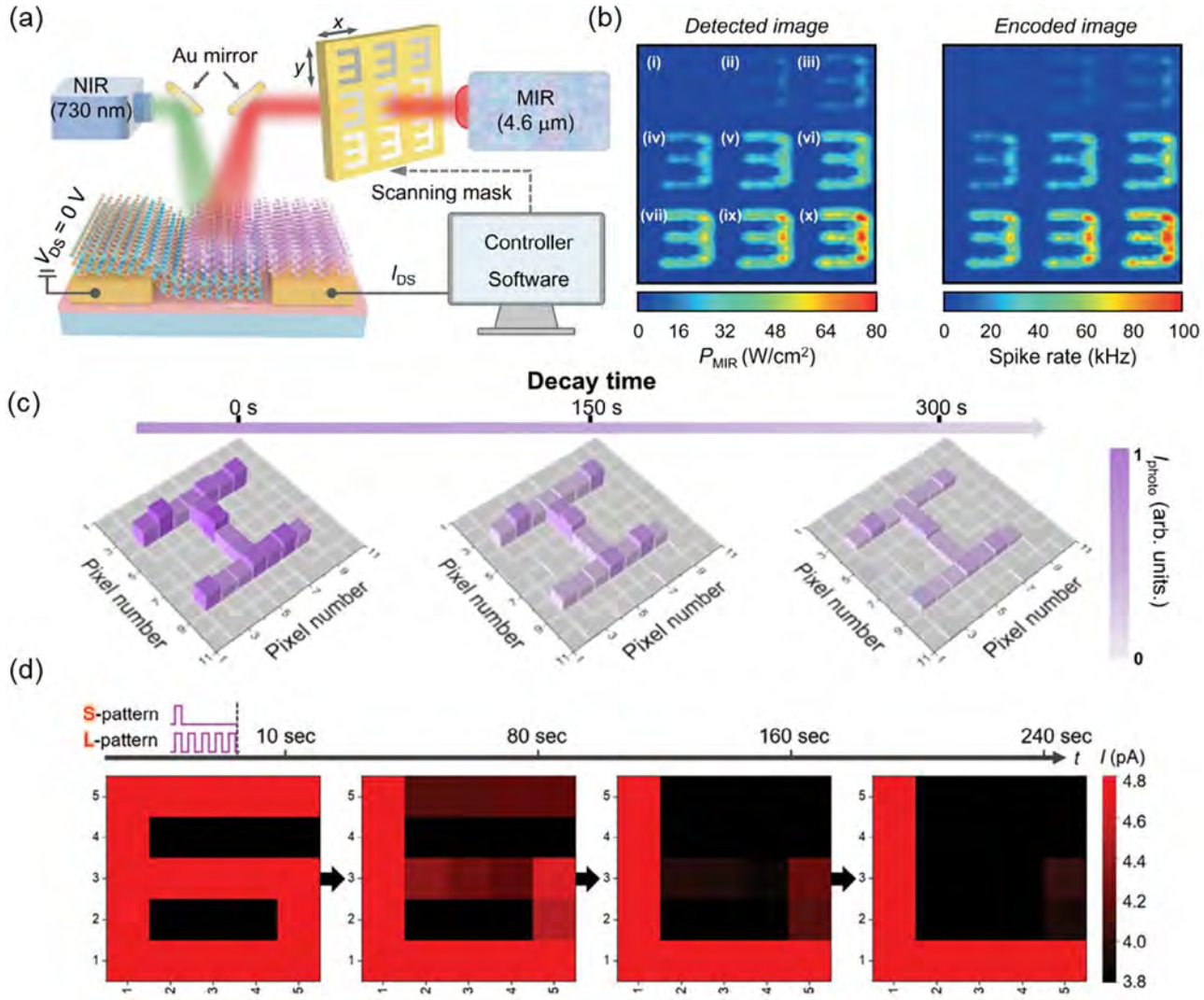


**Figure 18.** a) Schematic diagram of thdevice structure and graphical perception test.[180] Copyright 2023, Springer Nature. b) Pattern perception with different light intensities and different frequencies.[180] Copyright 2023, Springer Nature. c) Graphical perception and memory of the "H" shape on a 10 × 10 device array.[181] Copyright 2023, Springer Nature. d) Long-term and short-term memory for graphics under different impulse conditions.[182] Copyright 2024, Wiley-VCH.

and other perceptions.[185] The photoelectric response of most 2D semiconductors can effectively change the channel's carrier concentration and surface potential. Thus, when the photoelectric response is combined with gas and stress detection, multimodal sensing and enhanced sensing capabilities can be achieved simultaneously.[186]

The abundance of surface groups is very important in gas detection. Therefore, organic materials are an important carrier for gas detection, especially porous organic semiconductor materials.[187] In addition to COF and MOF, which are widely used for gas sensing, some 2D materials susceptible to gas surface doping are also effective platforms for gas-optoelectronic coupling. Chai's group used a combination of MXene and VP to take advantage of MXene's hydrophilicity and VP's gas surface doping, respectively. Visual-olfactory crossmodal perception was realized in gas and humidity environments (**Figure 19**a,b).[81] Song et al. used the assembly of multicomponent membrane scaffold proteins on Gr to prepare front-end olfactory receptors. The adsorption of different gases generates an accumulation of electrical potential that drives the back-end device.[188] In addition to gases, stress is an important source of information. Especially in robotics, medical devices, and wearable technology, force sensing can give devices tactile function and is the basis for highly dynamic feedback and adaptive control of delicate, intelligent systems.[189] There are two general types of stress perception and modulation; one is that it applies stress to the material itself. Yoo et al. imparted different stresses to the $SnSe_2$ channel by different bending styles and strengths to achieve piezo strain-driven enhancement of the optoelectronic synaptic response (Figure 19c).[190] Another way is to connect an external stress-sensing unit to regulate the device's photoelectric response. Chen et al. configured two triboelectric nanogenerator units for the same $MoTe_2$ channel to achieve different types of homojunction in the same channel. The


© 2025 Wiley-VCH GmbH

16136829, 0, Downloaded from https://onlinelibrary.wiley.com/doi/10.1002/smll.202503717 by City University Of Hong Kong, Wiley Online Library on [19/08/2025]. See the Terms and Conditions (https://onlinelibrary.wiley.com/terms-and-conditions) on Wiley Online Library for rules of use; OA articles are governed by the applicable Creative Commons License

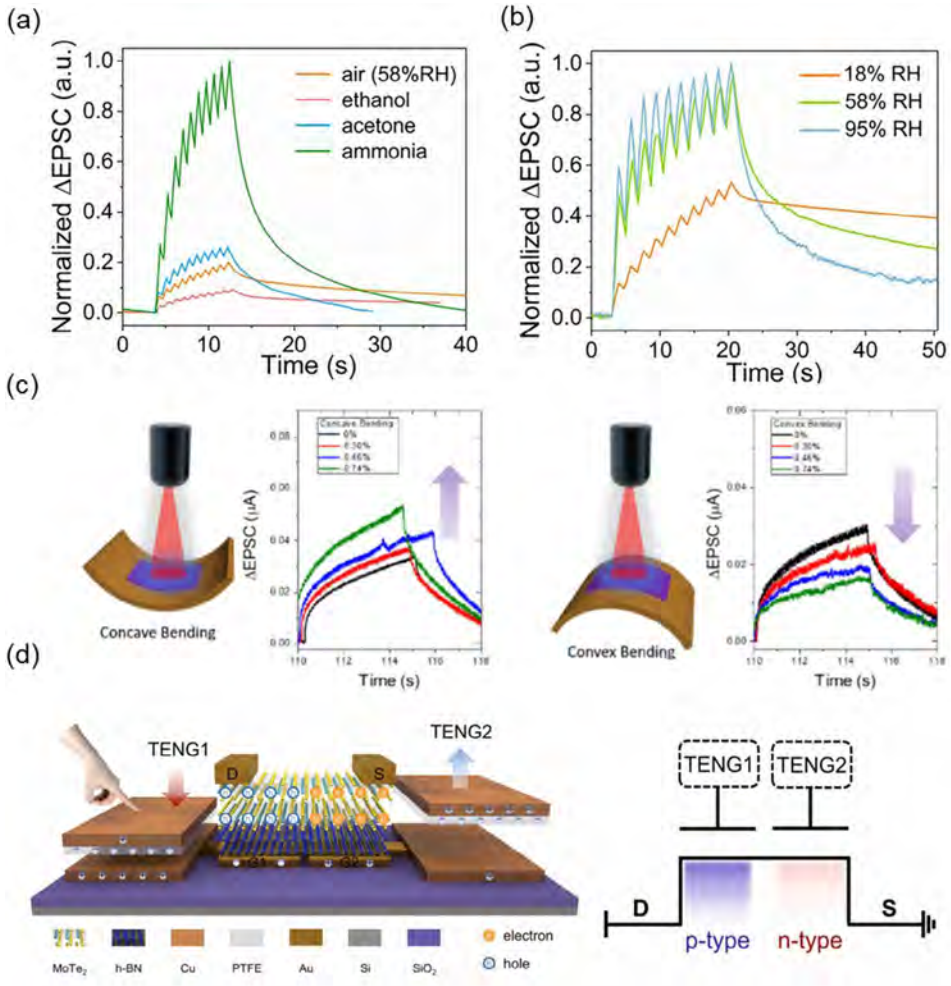


**Figure 19.** a) Optoelectronic neuromorphic response of devices under different gas atmospheres.[81] Copyright 2024, Springer Nature. b) Optoelectronic neuromorphic response of devices under different humidity conditions.[81] Copyright 2024, Springer Nature. c) Visual LTP response of the device under different strain modes.[190] Copyright 2024, American Chemical Society. d) Schematic structure of the device with integrated strain sensing and its channel type modulation.[191] Copyright 2025, Elsevier.

electrostatic charge generated by the triboelectric nanogenerator can control the type and concentration of charge carriers in the corresponding channel, thus enabling different reconfigurable photovoltaic effects under light conditions (Figure 19d).[191] This multimodal cross-sensing enables the device to resemble a biological organ more closely. It significantly improves the ability of artificial devices to co-sense and integrate information. In some exceptional cases, such as when one of the sensing modalities is disturbed, the multimodal complementarity can enhance the reliability and environmental adaptability of the bionic device.

### 5.4. Neural Network

Since the concept of neuromorphic engineering was proposed in the 1980s, neuromorphic computing combined with deep learning has gradually evolved toward brain-inspired computing. Unlike von Neumann architectures' storage-computation separation and serial computation, neuromorphic computing enables human brain-like asynchronous, distributed computation. At the hardware level, neuromorphic computing requires hardware that can break through the von Neumann bottleneck by not distinguishing between memory and computational units. At the hardware level, neuromorphic computing requires hardware that can perform highly parallel in-place operations in an event-driven (spike-based) manner without distinguishing between memory and computational units, thereby breaking the von Neumann bottleneck.[192] At the software level, current neural network architectures contain several parts: ANN, spiking neural networks (SNN), and RC. ANN-based feedforward neural networks (FNN), multi-layer perceptron (MLP), recurrent neural networks (RNN), and convolutional neural networks (CNN) are the widely used current architectures.[193] In general, this class of architectures consists of an input layer, a hidden layer, and an output layer, and each neuron computes the output using a weighted summation and activation function.[194] ANN is a broad computational architecture that can be applied to most deep learning tasks, but is accompanied by high computational resource consumption.[195,196]


© 2025 Wiley-VCH GmbH

16136829, 0, Downloaded from https://onlinelibrary.wiley.com/doi/10.1002/smll.202503717 by City University Of Hong Kong, Wiley Online Library on [19/08/2025]. See the Terms and Conditions (https://onlinelibrary.wiley.com/terms-and-conditions) on Wiley Online Library for rules of use; OA articles are governed by the applicable Creative Commons License

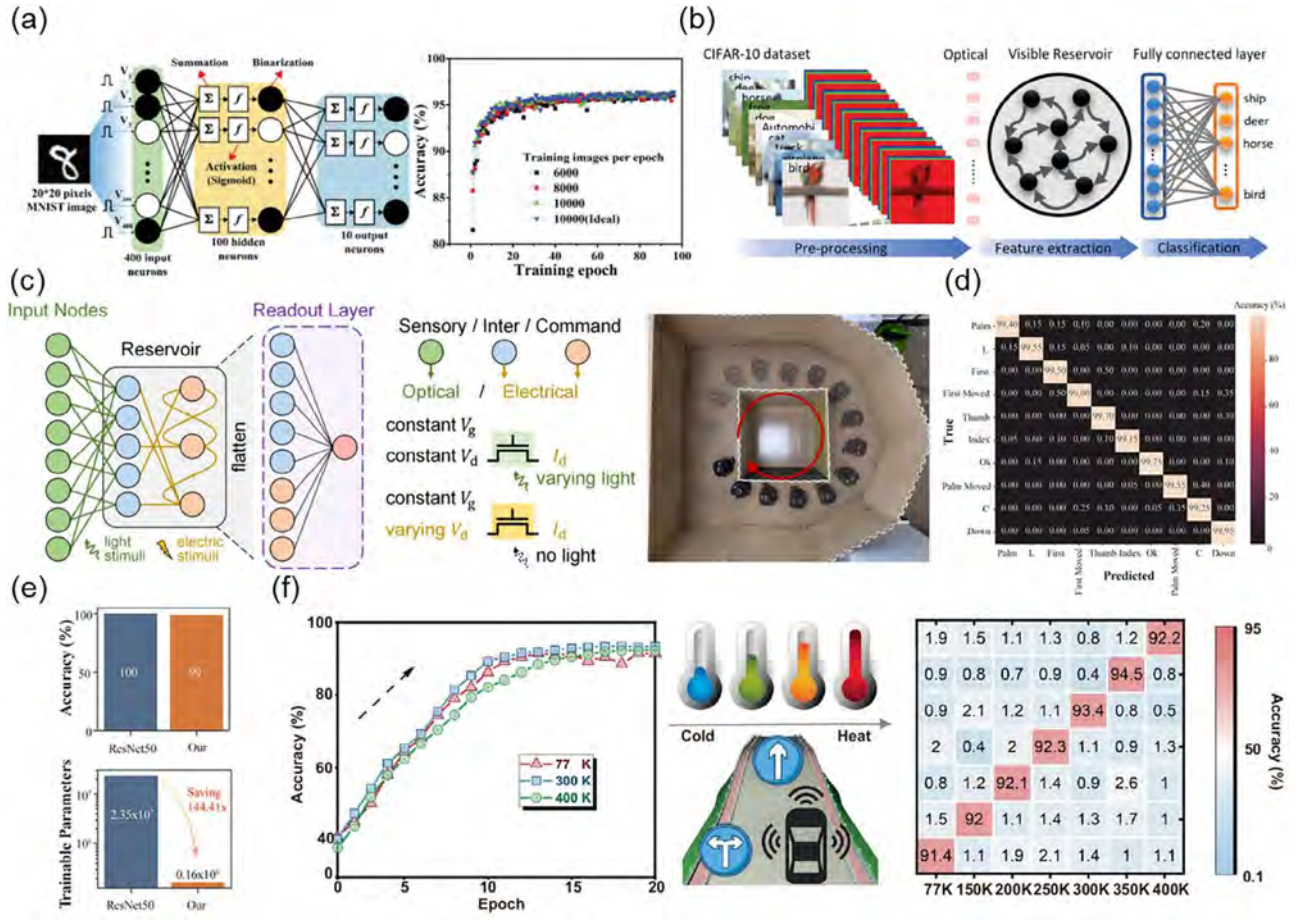


**Figure 20.** a) Three-layer ANN for the MNIST pattern recognition and recognition rate with different training epochs.[198] Copyright 2024, Wiley-VCH. b) Schematic diagram of ORNN-based color image classification operation with the dataset, RGB color preprocessing, RC layer, and fully connected layer.[201] Copyright 2024, Wiley-VCH. c) Schematic of the multimode RC system and experimental trajectories for obstacle avoidance.[202] Copyright 2024, American Chemical Society. d) Confusion matrix classification of event-based hand movement test sets.[203] Copyright 2024, Wiley-VCH.e) Difference between two different algorithmic architectures regarding recognition accuracy and resource share.[203] Copyright 2024, Wiley-VCH. f) Recognition accuracy based on SNN at different temperatures and the corresponding confusion matrix for trajectory recognition at different temperatures.[204] Copyright 2024, Springer Nature.

The RC system consists of an input layer, a reservoir, and an output layer, but only the weights of the output layer are trained. Therefore, RC is more efficient and suitable for low-power hardware and streaming computation of time series tasks. SNN is the closest to a biological nervous system, simulating real neurons' pulse (spike) behavior with event-driven computation.[197] Therefore, its computation is based on discrete events rather than continuous values, which makes it suitable for low-power and real-time computing tasks.[194]

Weng et al. utilized a fully connected three-layer ANN for the Modified National Institute of Standards and Technology (MNIST) pattern recognition. Due to the linear and symmetric changes in the conductance, the recognition accuracy can reach ≈96% (**Figure 20a**).[198] An et al. also constructed a simple three-layer ANN neural network based on the long-term potentiation and depression curves of optoelectronic synaptic devices to recognize handwritten digits.[199] Chen's group introduced more device variables into the ANN algorithm. The advantages of heterojunctions in photoconductivity response were verified by comparing the linearity of photoconductivity changes with different channel materials.[85] Zhai et al. combined 3D structured lattice-strained floating-gate optoelectronic synaptic transistors with ANN. High recognition of graphic targets due to UV-to-visible band response.[200] Yang et al. utilized 2D ferroelectric materials to modulate the bipolar channel and realized multiple optoelectronic responses under p- and n-type conditions. By constructing an optical RNN, efficient recognition of color images and low operating power consumption were achieved (Figure 20b).[201] RC is more advantageous when dealing with the computation of time-series data, especially dynamic system modeling, signal processing, and time-series prediction. Zhou et al. implemented fast feedback for dynamic vehicle lane-keeping by incorporating optoelectronic signals into the RC system (Figure 20c).[202] Tan's group also coupled the optoelectronic response into the $MoS_2$ channel via ferroelectric modulation of CIPS. Bringing optoelectronic response with temporal characteristics into an RC system saved 144 times the computing power than CNN architectures with similar performance (Figure 20d,e).[203] Yao et al. took


© 2025 Wiley-VCH GmbH

16136829, 0, Downloaded from https://onlinelibrary.wiley.com/doi/10.1002/smll.202503717 by City University Of Hong Kong, Wiley Online Library on [19/08/2025]. See the Terms and Conditions (https://onlinelibrary.wiley.com/terms-and-conditions) on Wiley Online Library for rules of use; OA articles are governed by the applicable Creative Commons License

**Table 3.** The summary of optoelectronic synaptic devices with different applications.

| Compound | Applications | Multimodal response | Neuromorphic response | Array size | Refs. |
|---|---|---|---|---|---|
| $SnSe/MoS_2$ | Logic AND gate | Optoelectronic | EPSC/LTP | / | [170] |
| $MoS_2$ | Logic AND/OR gate | Optoelectronic | EPSC/LTP/PPF | / | [171] |
| $TeO_2$ | Logic AND gate | Optoelectronic | EPSC/LTP/PPF | / | [172] |
| $MoS_2$/CIPS | Logic AND/OR/NOR/NAND gate | Optoelectronic/Triboelectric | EPSC/LTP/PPF | / | [173] |
| P3HT/GaAs | Image recognition | Optoelectronic | EPSC/LTP/PPF | 3 × 3 | [174] |
| $N:ZnO/MoS_2$ | Image recognition | Optoelectronic | EPSC/LTP/LTD/PPF | 25 × 10 | [177] |
| $MoS_2$ | Image recognition | Optoelectronic | LTM | / | [178] |
| $Fe_7S_8/MoS_2$ | Image recognition | Optoelectronic | EPSC/LTP/LTD/PPF engineering | 10 × 10 | [179] |
| $AsP/MoTe_2$ | Image recognition | Optoelectronic | LTP | / | [180] |
| $NbS_2/MoS_2$ | Image recognition | Optoelectronic | EPSC/LTP/LTD/PPF | 10 × 10 | [181] |
| LAO/STO | Image recognition | Optoelectronic | EPSC/LTP/PPF | 5 × 5 | [182] |
| $WSe_2/MoS_2$ | Image recognition | Optoelectronic | EPSC/LTP | 3 × 3 | [183] |
| $TiN_xO_{2-x}/MoS_2$ | Image recognition | Optoelectronic | EPSC/LTP | / | [184] |
| $MoTe_2$ | Hybrid perception | Optoelectronic/Triboelectric | EPSC/LTP | / | [185] |
| MXene/VP | Hybrid perception | Optoelectronic/Gas/Humidity | EPSC/LTP/LTD/PPF | / | [81] |
| $SnSe_{2-x}$ | Hybrid perception | Optoelectronic/Stress | EPSC/LTP/PPF | / | [190] |
| $MoS_2/Ta_2NiS_5$ | Three-layer neural network. | Optoelectronic | EPSC/LTP/LTD | / | [199] |
| $CsPbBr_3$/MXene | ANN | Optoelectronic | EPSC/LTP | / | [85] |
| $MoS_2$/Gr | ANN | Optoelectronic | EPSC/PPF/LTP | / | [200] |
| $WSe_2$/Gr/CIPS | ORNN | Optoelectronic/ Ferroelectric | EPSC/LTP/LTD/PPF | / | [201] |
| $\alpha$-$In_2Se_3$ | RC | Optoelectronic/ Ferroelectric | EPSC/LTP/LTD/STDP | / | [202] |
| $MoS_2$/CIPS | RC | Optoelectronic/ Ferroelectric | EPSC/LTP/LTM | / | [203] |

advantage of the SNN's low power consumption and processing of dynamic timing data in autonomous driving. Pulse timing-dependent plasticity of optoelectronic neuromorphic devices stabilized under different temperature conditions offers the potential for developing autonomous driving hardware under complex temperature conditions (Figure 20f).[204] In addition to a single device matching a single algorithm, targeted matching of multiple algorithms can be achieved by integrating different functional units. Yang's group integrated memristor units into a phototransistor array to be compatible with machine learning and bioinspired neural network architectures. The multi-phototransistor-one-memristor array architecture can effectively utilize optical RNN and optical SNN to integrate spatial and spatiotemporal information and enhance the recognition of multiple types of information.[205]

The corresponding summarization of applications is shown in **Table 3**.

## 6. Summary and Outlook

The von Neumann architecture, as the core of traditional computing, has been the foundational design of modern computers, guiding their evolution for decades. However, its inherent separation of storage and processing leads to inefficiencies in data transfer, known as the von Neumann bottleneck. This issue becomes increasingly problematic as artificial intelligence proliferates and data streams grow exponentially. Consequently, a new paradigm inspired by the human brain has emerged: neuromorphic computing. This approach, modeled after biological neural networks, addresses the bottleneck through event-driven, pulse-computing, and integrated storage-computing techniques. By gradually overcoming data transfer speed limitations and significantly reducing the power consumption associated with high-throughput computing, neuromorphic computing is poised to complement and eventually supplant the von Neumann architecture, fueled by advancements in deep learning algorithms and neuromorphic hardware. It is anticipated that architectural transitions will progress from near-sensor computing to in-sensor computing. Currently, near-sensor computing, which positions computational units adjacent to storage devices, effectively mitigates big data retrieval and transmission pressures in certain applications, such as autonomous vehicle computing. As a transitional phase, the shift from near-sensor to in-sensor computing can be achieved by integrating computational units within sensors deeply aligned with neuromorphic computing principles. Thus, continuous innovation in software and hardware development for neuromorphic computing is crucial.

The selection of material systems is vital to achieving these goals. 2D materials are emerging as promising alternatives to traditional silicon-based materials, demonstrating exceptional performance and scalability across various domains. In recent years, 2D materials have shown immense potential for visual neuromorphic computing applications. Their atomic-level thickness confines electron transport to ultrathin planes, exhibiting remarkable transport capabilities. From the inception of high-performance devices with full vdW contacts to the current lattice slide stacking enabled by twistronics, 2D materials have proven their scalability for high-performance devices. For visual neuromorphic devices, the multimodal perception properties of


© 2025 Wiley-VCH GmbH

16136829, 0, Downloaded from https://onlinelibrary.wiley.com/doi/10.1002/smll.202503717 by City University Of Hong Kong, Wiley Online Library on [19/08/2025]. See the Terms and Conditions (https://onlinelibrary.wiley.com/terms-and-conditions) on Wiley Online Library for rules of use; OA articles are governed by the applicable Creative Commons License

2D materials, such as anisotropic transport, opto-thermoelectric coupling, opto-ferroelectric coupling, and polarization detection, pave the way for developing smarter artificial visual perception systems.

After more than a decade of development, the future of neuromorphic computing will depend on breakthroughs in novel synaptic components. The successive introduction of systems such as Neurogrid, SpiNNaker, BrainScaleS, and others demonstrates the urgency of realizing the vision of low-power, large-scale digital modeling of the human-like brain.[206] Important reasons are the continued explosive growth in global computing demand, increased carbon emissions, and the vast application promise of neuromorphic computing. In recent years, with the rise of AI applications (e.g., big model training), electricity use by big data analytics centers is expected to grow by 160% by 2030, raising its share of global electricity use to 3–4%. Correspondingly, $CO_2$ emissions are projected to double between 2022 and 2030.[207,208] Today, the algorithmic architecture of neuromorphic computing is constantly improving and evolving iteratively at an astonishing rate. Neuromorphic computing has a promising future in edge AI and IoT due to low power and real-time advantages. It is suitable for tasks in low-resource and low-power environments, such as dynamic scene sensing for smart cameras and biosignal processing for wearable devices.[209] Also, neuromorphic computing can be used for event-driven visual or auditory sensing to detect motion and sound efficiently without consuming too much energy. In addition, real-time sensing and adaptive control are important application scenarios in robotics and autonomous systems. Although computational models such as SNNs are available to enable naturally low-energy computation, power consumption and data transfer remain huge obstacles in the future due to current hardware architectures and sensing components. Overall, 2D material systems have many advantages over other materials as the most promising alternative to silicon-based carriers for next-generation computing architectures today: excellent optoelectronic properties; vdW contacts; multimodal sensing capabilities; and scalability and programmability. Compared with traditional silicon-based and metal-oxide materials, the photoelectric response performance of 2D materials has obvious advantages in responsivity, detectivity, and response band. As a semiconductor material, its carrier mobility and environmental stability are superior to organic semiconductor materials. The vdW contacts not only bring clean interfaces to 2D materials, offering the possibility of mechanical exfoliation preparation, but also bring more efficient contacting methods to all kinds of heterojunction devices based on 2D materials, reducing scattering and trapping of carriers during transport. At the same time, this non-covalent interaction can give the interface a sliding capacity in the face of stress action, releasing the shear forces acting on the lattice. 2D materials with different lattice stacking patterns can exhibit different responses to different stimuli, such as thermoelectric, photoelectric, ferroelectric, and anisotropic. A multimodal reaction means the number of units sensing/processing analog signals can be reduced. One device can process different signals or be modularly replaced as required. It is also feasible to reduce the delays incurred by the inter-calling of information and the costs associated with producing different devices.[210] Therefore, in-sensor computing devices based on 2D materials can be designed and prepared in an oriented way to achieve some specific perceptual and computational goals. The most suitable materials can be selected, the most appropriate atomic layer thicknesses can be used (to find a balance between the various properties), different 2D materials can be selected for non-destructive stacking, and so on. This modular scalability and programmability are also difficult for other material systems.

Despite their promise, 2D materials face challenges in visual neuromorphic computing. Foremost is the need for large-area integration methods compatible with the CMOS fabrication process. While chemical vapor deposition and molecular beam epitaxy allow for large-scale growth of high-quality 2D films, the variety of materials and substrate choices remains limited. Additionally, improving the air stability of certain 2D materials is crucial, as difficult-to-control air/semiconductor oxidation interfaces can compromise device array homogeneity and long-term stability. Power consumption also poses a significant hurdle for AI development. Although efforts have been made to reduce the power consumption of individual pulse responses to levels below those of human neurons, reports on low-power devices based on array operations are scarce. Due to their thickness and carrier concentration, 2D materials have substantial advantages in controlling device power consumption. Leveraging the intrinsic properties of 2D materials to modulate conductance offers a power consumption benefit over using external functional layers. For instance, employing ferroelectric 2D semiconductors for information storage modulation consumes considerably less power than using ferroelectric insulating layers. Thus, the power consumption issue presents both a challenge and an opportunity for 2D material systems. For the future direction, arrayization, chip-on-chip, and multimodality are important foundations for realizing in-sensor computing chips. It is already possible to realize high-density preparation of existing chip architectures using $MoS_2$ as a carrier.[211] The next step should be the realization of CMOS process-compatible 2D heterostructures and hybrid integration technologies to achieve higher device density and energy efficiency.[212] For optoelectronic in-sensor computing based on 2D materials, the sensing dimensions have been extended from optoelectronics to force, magnetism, and heat. On the one hand, the combination of sparse pulse training and event-driven sensors is continuously promoted for future development. On the other hand, the decoupling of analog signals under different stimuli is realized. The former is further to reduce the power consumption of system sensing and training, and the latter is to avoid crosstalk of signals under multimodal sensing and erroneous synaptic weight adjustment during training.

As neuromorphic computing rapidly advances, visual neural perception systems based on 2D materials are revolutionizing device architectures. Some research focuses on achieving in-sensor computing with single devices or small arrays, exploring complex material combinations, exotic optoelectronic phenomena, and intricate modulated coupling methods. Other researchers aim to realize chip-based large-scale integration, requiring simple material structures and well-homogenized regulatory mechanisms. By integrating the enhanced neuromorphic computing paradigm, evolved from CNNs, with multiple architectures, a multimodal, low-power in-sensor computing visual system is believed to be realized eventually.


© 2025 Wiley-VCH GmbH

16136829, 0, Downloaded from https://onlinelibrary.wiley.com/doi/10.1002/smll.202503717 by City University Of Hong Kong, Wiley Online Library on [19/08/2025]. See the Terms and Conditions (https://onlinelibrary.wiley.com/terms-and-conditions) on Wiley Online Library for rules of use; OA articles are governed by the applicable Creative Commons License

## Acknowledgements

The authors acknowledge a fellowship award from the Research Grants Council of the Hong Kong Special Administrative Region, China (CityU RFS2021-1S04), the Innovation and Technology Fund (MHP/126/21) from the Innovation and Technology Commission of the Hong Kong Special Administrative Region, China, the Shenzhen Municipality Science and Technology Innovation Commission (Project No. JCYJ20230807114910021), and Guangdong Basic and Applied Basic Research Fund (Project no. 2024A1515011922).

## Conflict of Interest

The authors declare no conflict of interest.

## Author Contributions

P.X. wrote, reviewed, and edited the original and final draft, visualized the study, and performed validation. D.L. performed editing and validation. W.W. performed visualization and literature collation. J.C.H. performed conceptualization, acquired resources and funds, supervised the study, and wrote, reviewed, and edited the final draft.

## Keywords

2D semiconductor, artificial synapse, neuromorphic computing, optoelectronic device

Received: March 23, 2025
Revised: June 18, 2025
Published online:

[1] W. Deng, X. Yan, L. Wang, N. Yu, W. Luo, L. Mai, *Nano. Energy.* **2024**, *128*, 109861.
[2] Y. Joo, E. Hwang, H. Hong, S. Cho, H. Yang, *Adv. Electron. Mater.* **2023**, *9*, 2300211.
[3] N. Ilyas, J. Wang, C. Li, D. Li, H. Fu, D. Gu, X. Jiang, F. Liu, Y. Jiang, W. Li, *Adv. Funct. Mater.* **2022**, *32*, 2110976.
[4] J. Ma, H. Liu, N. Yang, J. Zou, S. Lin, Y. Zhang, X. Zhang, J. Guo, H. Wang, *Adv. Mater.* **2022**, *34*, 2202371.
[5] S. Zhu, T. Xie, Z. Lv, Y.-B. Leng, Y.-Q. Zhang, R. Xu, J. Qin, Y. Zhou, V. A. L. Roy, S.-T. Han, *Adv. Mater.* **2024**, *36*, 2301986.
[6] M. A. Zidan, J. P. Strachan, W. D. Lu, *Nat. Electron.* **2018**, *1*, 22.
[7] C. Choi, G. J. Lee, S. Chang, Y. M. Song, D.-H. Kim, *ACS Nano* **2024**, *18*, 1241.
[8] G. Feng, X. Zhang, B. Tian, C. Duan, *InfoMat* **2023**, *5*, 12473.
[9] N. Li, S. Zhang, Y. Peng, X. Li, Y. Zhang, C. He, G. Zhang, *Adv. Funct. Mater.* **2023**, *33*, 2305589.
[10] C. Liu, T. Liu, Z. Zhang, Z. Sun, G. Zhang, E. Wang, K. Liu, *Nat. Nanotechnol.* **2024**, *19*, 907.
[11] X. Yan, Z. Zheng, V. K. Sangwan, J. H. Qian, X. Wang, S. E. Liu, K. Watanabe, T. Taniguchi, S.-Y. Xu, P. Jarillo-Herrero, Q. Ma, M. C. Hersam, *Nature* **2023**, *624*, 551.
[12] L. Mennel, J. Symonowicz, S. Wachter, D. K. Polyushkin, A. J. Molina-Mendoza, T. Mueller, *Nature* **2020**, *579*, 62.
[13] L. Liu, Y. Zhang, Y. Yan, *Nanoscale Horiz.* **2023**, *8*, 1301.
[14] M. M. Rehman, Y. A. Samad, J. Z. Gul, M. Saqib, M. Khan, R. A. Shaukat, R. Chang, Y. Shi, W. Y. Kim, *Prog. Mater Sci.* **2025**, *152*, 101471.
[15] Q. Ren, C. Zhu, S. Ma, Z. Wang, J. Yan, T. Wan, W. Yan, Y. Chai, *Adv. Mater.* **2024**, *37*, 2407476.
[16] D. Akinwande, C. Huyghebaert, C.-H. Wang, M. I. Serna, S. Goossens, L.-J. Li, H. S. P. Wong, F. H. L. Koppens, *Nature* **2019**, *573*, 507.
[17] H. Liu, J. Wu, J. Ma, X. Yan, N. Yang, X. He, Y. He, H. Zhang, T.-H. Hsu, J. H. Qian, J. Guo, M. C. Hersam, H. Wang, *Nat. Electron.* **2024**, *7*, 876.
[18] M.-Y. Tsai, C.-T. Huang, C.-Y. Lin, M.-P. Lee, F.-S. Yang, M. Li, Y.-M. Chang, K. Watanabe, T. Taniguchi, C.-H. Ho, W.-W. Wu, M. Yamamoto, J.-L. Wu, P.-W. Chiu, Y.-F. Lin, *Nat. Electron.* **2023**, *6*, 755.
[19] J. Chen, W. Xu, *eScience* **2023**, *3*, 100178.
[20] Y. Ren, L. Sun, Y. Xie, S. Gao, Y. Du, M. Zhang, X. Wu, X. Zhu, F. Yang, W. Hu, *J. Mater. Chem. C.* **2024**, *12*, 9455.
[21] Z. Guo, J. Zhang, X. Liu, L. Wang, L. Xiong, J. Huang, *Adv. Funct. Mater.* **2023**, *33*, 2305508.
[22] Q. Qiu, Z. Huang, *Adv. Mater.* **2021**, *33*, 2008126.
[23] X.-M. Dong, C. Chen, Y.-X. Li, H.-C. Sun, B. Liu, Z.-F. Li, K.-L. Wang, Z.-X. He, M.-N. Yu, W. Huang, J.-Q. Liu, *ACS. Nano.* **2025**, *19*, 5718.
[24] S. Wang, H. Chen, T. Liu, Y. Wei, G. Yao, Q. Lin, X. Han, C. Zhang, H. Huang, *Angew. Chem., Int. Ed.* **2023**, *62*, 202213733.
[25] H. Chen, Y. Cai, Y. Han, H. Huang, *Angew. Chem., Int. Ed.* **2024**, *63*, 202313634.
[26] P. Xie, T. Liu, J. Sun, J. Yang, *Adv. Funct. Mater.* **2022**, *32*, 2200843.
[27] J. Zhang, Y. Zhong, H. Jiang, Z. Zhao, H. Wang, R. Wang, Z. Chen, Q. Liang, X. Wang, F. Sun, Y. Xing, X. Duan, H. Li, L.-W. Feng, M. Zhu, H. Sun, G. Wang, *Adv. Mater.* **2025**, https://doi.org/10.1002/adma.202417452.
[28] M. Li, M. Liu, F. Qi, F. R. Lin, A. K. Y. Jen, *Chem. Rev.* **2024**, *124*, 2138.
[29] S. Duan, X. Zhang, Y. Xi, D. Liu, X. Zhang, C. Li, L. Jiang, L. Li, H. Chen, X. Ren, W. Hu, *Adv. Mater.* **2024**, *36*, 2405030.
[30] Q. Lv, X.-D. Wang, Y. Yu, C.-F. Xu, Y.-J. Yu, X.-Y. Xia, M. Zheng, L.-S. Liao, *Nat. Chem.* **2024**, *16*, 201.
[31] L. Zhang, X. Tian, J. Yao, X. Song, S. Yang, S. Guo, Y. Wang, B. Li, X. Ren, Y. Sun, F. Yang, R. Li, W. Hu, *J. Mater. Chem. C.* **2021**, *9*, 8834.
[32] M. Dong, Y. Zhang, J. Zhu, X. Zhu, J. Zhao, Q. Zhao, L. Sun, Y. Sun, F. Yang, W. Hu, *Adv. Mater.* **2024**, *36*, 2409550.
[33] F. Cui, V. García-López, Z. Wang, Z. Luo, D. He, X. Feng, R. Dong, X. Wang, *Chem. Rev.* **2025**, *125*, 445.
[34] H. Wei, J. Liu, Y. Ni, X. Hu, X. Lv, L. Yang, G. He, Z. Xu, J. Gong, C. Jiang, D. Feng, W. Xu, *Nano Lett.* **2024**, *24*, 15379.
[35] J. Hong, M. Liu, Y. Liu, S. Shang, X. Wang, C. Du, W. Gao, C. Hua, H. Xu, Z. You, Y. Liu, J. Chen, *Angew. Chem., Int. Ed.* **2024**, *63*, 202317876.
[36] J. Song, C.-K. Liu, V. Piradi, C. Chen, Y. Zhu, X. Zhu, L. Li, W.-Y. Wong, F. Yan, *Adv. Sci.* **2024**, *11*, 2305551.
[37] L. Wang, Y. Zhang, Y. Chen, L. Jiang, *ACS. Nano.* **2024**, *18*, 9043.
[38] L. Liu, W. Ji, W. He, Y. Cheng, R. Hao, P. Hao, H. Dong, X. Ding, S. Lei, B. Han, W. Hu, *Adv. Mater.* **2024**, *36*, 2405328.
[39] J. Chen, M.-Y. Sun, Z.-H. Wang, Z. Zhang, K. Zhang, S. Wang, Y. Zhang, X. Wu, T.-L. Ren, H. Liu, L. Han, *Nano-Micro. Lett.* **2024**, *16*, 264.
[40] L. Liao, E. Kovalska, J. Regner, Q. Song, Z. Sofer, *Small* **2024**, *20*, 2303638.
[41] K. C. Kwon, J. H. Baek, K. Hong, S. Y. Kim, H. W. Jang, *Nano-Micro. Lett.* **2022**, *14*, 58.
[42] J.-W. Zhao, H.-Y. Wang, L. Feng, J.-Z. Zhu, J.-X. Liu, W.-X. Li, *Chem. Rev.* **2024**, *124*, 164.
[43] D. Kim, J. Pandey, J. Jeong, W. Cho, S. Lee, S. Cho, H. Yang, *Chem. Rev.* **2023**, *123*, 11230.
[44] X. Chia, A. Y. S. Eng, A. Ambrosi, S. M. Tan, M. Pumera, *Chem. Rev.* **2015**, *115*, 11941.
[45] R. Dutta, A. Bala, A. Sen, M. R. Spinazze, H. Park, W. Choi, Y. Yoon, S. Kim, *Adv. Mater.* **2023**, *35*, 2303272.
[46] M. Dang, X. Duan, C. Liu, S. Zhang, X. Hong, W. Niu, P. Luo, B. Jiang, T. Bu, L. Tang, W. Jiang, D. Wan, X. Zou, L. Liao, X. Liu, *Appl. Phys. Lett.* **2024**, *124*, 123502.

 © 2025 Wiley-VCH GmbH

16136829, 0, Downloaded from https://onlinelibrary.wiley.com/doi/10.1002/smll.202503717 by City University Of Hong Kong, Wiley Online Library on [19/08/2025]. See the Terms and Conditions (https://onlinelibrary.wiley.com/terms-and-conditions) on Wiley Online Library for rules of use; OA articles are governed by the applicable Creative Commons License

[47] J. Chen, Z. Zhou, B. J. Kim, Y. Zhou, Z. Wang, T. Wan, J. Yan, J. Kang, J.-H. Ahn, Y. Chai, *Nat. Nanotechnol.* **2023**, *18*, 882.
[48] Y. Lin, W. Wang, R. Li, J. Kim, C. Zhang, H. Kan, Y. Li, *Nano. Energy.* **2024**, *121*, 109267.
[49] Y. Wang, T. Zhou, Y. Cui, M. Xu, M. Zhang, K. Tang, X. Chen, H. Tian, C. Yin, J. Huang, C. Yan, X. Wang, *Adv. Funct. Mater.* **2024**, *34*, 2400039.
[50] Y. Wang, B. Han, M. Mayor, P. Samorì, *Adv. Mater.* **2024**, *36*, 2307359.
[51] F. F. Lupi, G. Milano, A. Angelini, M. Rosero-Realpe, B. Torre, E. Kozma, C. Martella, C. Grazianetti, *Adv. Funct. Mater.* **2024**, *34*, 2403158.
[52] Y. Gong, X. Xing, X. Wang, R. Duan, S.-T. Han, B. K. Tay, *Adv. Funct. Mater.* **2024**, *34*, 2406547.
[53] D. Xie, G. Gao, B. Tian, Z. Shu, H. Duan, W.-W. Zhao, J. He, J. Jiang, *Adv. Mater.* **2023**, *35*, 2212118.
[54] Z. Dang, F. Guo, Y. Zhao, K. Jin, W. Jie, J. Hao, *Adv. Funct. Mater.* **2024**, *34*, 2400105.
[55] Y. Deng, S. Liu, X. Ma, S. Guo, B. Zhai, Z. Zhang, M. Li, Y. Yu, W. Hu, H. Yang, Y. Kapitonov, J. Han, J. Wu, Y. Li, T. Zhai, *Adv. Mater.* **2024**, *36*, 2309940.
[56] F. Huang, C. Ke, J. Li, L. Chen, J. Yin, X. Li, Z. Wu, C. Zhang, F. Xu, Y. Wu, J. Kang, *Adv. Sci.* **2023**, *10*, 2302813.
[57] H. Yang, Y. Hu, X. Zhang, Y. Ding, S. Wang, Z. Su, Y. Shuai, P. Hu, *Adv. Funct. Mater.* **2024**, *34*, 2308149.
[58] Y. Gong, P. Xie, X. Xing, Z. Lv, T. Xie, S. Zhu, H.-H. Hsu, Y. Zhou, S.-T. Han, *Adv. Funct. Mater.* **2023**, *33*, 2303539.
[59] Z. Wang, B. J. Wieder, J. Li, B. Yan, B. A. Bernevig, *Phys. Rev. Lett.* **2019**, *123*, 186401.
[60] B. Su, Y. Huang, Y. H. Hou, J. Li, R. Yang, Y. Ma, Y. Yang, G. Zhang, X. Zhou, J. Luo, Z.-G. Chen, *Adv. Sci.* **2022**, *9*, 2101532.
[61] Y. Xiao, W. Li, X. Lin, Y. Ji, Z. Chen, Y. Jiang, Q. Liu, X. Tang, Q. Liang, *Adv. Electron. Mater.* **2023**, *9*, 2300388.
[62] M. J. Allen, V. C. Tung, R. B. Kaner, *Chem. Rev.* **2010**, *110*, 132.
[63] J. Liu, S. Zhang, Y. Guo, Q. Wang, *Sci. Rep.* **2016**, *6*, 37528.
[64] F. Calavalle, M. Suárez-Rodríguez, B. Martín-García, A. Johansson, D. C. Vaz, H. Yang, I. V. Maznichenko, S. Ostanin, A. Mateo-Alonso, A. Chuvilin, I. Mertig, M. Gobbi, F. Casanova, L. E. Hueso, *Nat. Mater.* **2022**, *21*, 526.
[65] M. Zhang, Z. Chi, G. Wang, Z. Fan, H. Wu, P. Yang, J. Yang, P. Yan, Z. Sun, *Adv. Mater.* **2022**, *34*, 2205679.
[66] L. Liu, C. Liu, L. Jiang, J. Li, Y. Ding, S. Wang, Y.-G. Jiang, Y.-B. Sun, J. Wang, S. Chen, D. W. Zhang, P. Zhou, *Nat. Nanotechnol.* **2021**, *16*, 874.
[67] Y. Chen, Y. Kang, H. Hao, X. Xie, J. Zeng, T. Xu, C. Li, Y. Tan, L. Fang, *Adv. Funct. Mater.* **2023**, *33*, 2209781.
[68] Q. Guo, D. Ji, Q. Wang, L. Peng, C. Zhang, Y. Wu, D. Kong, S. Luo, W. Liu, G. Chen, D. Wei, Y. Liu, D. Wei, *Adv. Mater.* **2024**, *36*, 2406345.
[69] H. Tang, T. Anwar, M. S. Jang, G. Tagliabue, *Adv. Sci.* **2024**, *11*, 2309876.
[70] Y. Shen, P. Hou, *Small* **2025**, *21*, 2405709.
[71] L. Dong, B. Xue, G. Wei, S. Yuan, M. Chen, Y. Liu, Y. Su, Y. Niu, B. Xu, P. Wang, *Adv. Sci.* **2024**, *11*, 2403665.
[72] L. Dong, S. Yuan, G. Wei, P. Zhu, S. Ma, B. Xu, Y. Yang, *Small* **2024**, *20*, 2306998.
[73] W. Ahmad, A. Abbas, U. Younis, J. Zhang, S. H. Aleithan, Z. Wang, *Adv. Funct. Mater.* **2024**, *34*, 2410723.
[74] Y. Zhu, Y. Wang, X. Pang, Y. Jiang, X. Liu, Q. Li, Z. Wang, C. Liu, W. Hu, P. Zhou, *Nat. Commun.* **2024**, *15*, 6015.
[75] H. Shao, W. Wang, Y. Zhang, B. Gao, C. Jiang, Y. Li, P. Xie, Y. Yan, Y. Shen, Z. Wu, R. Wang, Y. Ji, H. Ling, W. Huang, J. C. Ho, *Adv. Mater.* **2025**, *37*, 2414261.
[76] X. Liu, S. Wang, Z. Di, H. Wu, C. Liu, P. Zhou, *Adv. Sci.* **2023**, *10*, 2301851.
[77] D. A. Nguyen, Y. Jo, T. U. Tran, M. S. Jeong, H. Kim, H. Im, *Small. Methods.* **2021**, *5*, 2101303.
[78] M. Chen, Z. Wu, Z. Qiu, J. Peng, W. Gao, M. Yang, L. Huang, J. Yao, Y. Zhao, Z. Zheng, Y. Ni, J. Li, *Nano. Lett.* **2025**, *25*, 3002.
[79] K. Huang, Z. Li, J. Lin, G. Han, P. Huang, *Chem. Soc. Rev.* **2018**, *47*, 5109.
[80] G. Murali, J. K. Reddy Modigunta, Y. H. Park, J.-H. Lee, J. Rawal, S.-Y. Lee, I. In, S.-J. Park, *ACS. Nano.* **2022**, *16*, 13370.
[81] H. Ma, H. Fang, X. Xie, Y. Liu, H. Tian, Y. Chai, *Nano-Micro Lett.* **2024**, *16*, 104.
[82] H. Teixeira, C. Dias, A. V. Silva, J. Ventura, *ACS Nano.* **2024**, *18*, 21685.
[83] Y. Li, G. Ding, Y. Zhai, Z. Lv, Y. Yan, S. Xue, K. Zhou, M. Zhang, Y. Zhang, Q.-J. Sun, Y. Liu, V. A. L. Roy, Y. Zhou, S.-T. Han, *Small.* **2025**, 2410914.
[84] D. Tan, Z. Zhang, H. Shi, N. Sun, Q. Li, S. Bi, J. Huang, Y. Liu, Q. Guo, C. Jiang, *Adv. Mater.* **2024**, *36*, 2407751.
[85] Y. Dai, G. Chen, W. Huang, C. Xu, C. Liu, Z. Huang, T. Guo, H. Chen, *Sci. China Mater.* **2024**, *67*, 2246.
[86] C. Hu, Z. Wei, L. Li, G. Shen, *Adv. Funct. Mater.* **2023**, *33*, 2302188.
[87] T. Mei, W. Liu, F. Sun, Y. Chen, G. Xu, Z. Huang, Y. Jiang, S. Wang, L. Chen, J. Liu, F. Fan, K. Xiao, *Angew. Chem., Int. Ed.* **2024**, *63*, 202401477.
[88] X. Zhang, S. Wu, R. Yu, E. Li, D. Liu, C. Gao, Y. Hu, T. Guo, H. Chen, *Matter* **2022**, *5*, 3023.
[89] X. Lian, X. Shen, M. Zhang, J. Xu, F. Gao, X. Wan, E. Hu, Y. Guo, J. Zhao, Y. Tong, *Appl. Phys. Lett.* **2019**, *115*, 063501.
[90] J. Huang, S. Yang, X. Tang, L. Yang, W. Chen, Z. Chen, X. Li, Z. Zeng, Z. Tang, X. Gui, *Adv. Mater.* **2023**, *35*, 2303737.
[91] J. Fang, Z. Tang, X.-C. Lai, F. Qiu, Y.-P. Jiang, Q.-X. Liu, X.-G. Tang, Q.-J. Sun, Y.-C. Zhou, J.-M. Fan, J. Gao, *ACS Appl. Mater. Interfaces.* **2024**, *16*, 31348.
[92] J. H. Ju, S. Seo, S. Baek, D. Lee, S. Lee, T. Lee, B. Kim, J.-J. Lee, J. Koo, H. Choo, S. Lee, J.-H. Park, *Small* **2021**, *17*, 2102595.
[93] D. Hao, Z. Yang, J. Huang, F. Shan, *Adv. Funct. Mater.* **2023**, *33*, 2211467.
[94] B. Li, F. Xia, B. Du, S. Zhang, L. Xu, Q. Su, D. Zhang, J. Yang, *Adv. Sci.* **2024**, *11*, 2310263.
[95] Y. Wang, Y. Zha, C. Bao, F. Hu, Y. Di, C. Liu, F. Xing, X. Xu, X. Wen, Z. Gan, B. Jia, *Adv. Mater.* **2024**, *36*, 2311524.
[96] S. J. Kim, I. H. Im, J. H. Baek, S. Choi, S. H. Park, D. E. Lee, J. Y. Kim, S. Y. Kim, N.-G. Park, D. Lee, J. J. Yang, H. W. Jang, *Nat. Nanotechnol.* **2025**, *20*, 83.
[97] J. Chen, X. Liu, Q. Zhu, X. Fang, W. Xu, *Adv. Funct. Mater.* **2024**, *34*, 2402684.
[98] Y. Wang, S. Chen, X. Cheng, W. Chen, Z. Xiong, Z. Lv, C. Wu, L. Wang, G. Zhang, X. Zhu, L. Luo, S.-T. Han, *Adv. Funct. Mater.* **2024**, *34*, 2309807.
[99] X. Feng, R. Cheng, L. Yin, Y. Wen, J. Jiang, J. He, *Adv. Mater.* **2024**, *36*, 2304708.
[100] M. Li, P. Chen, Y. Zhao, M. Zhao, H. Leng, Y. Wang, S. Ali, F. Raziq, X. Wu, J. Yi, H. Xiao, L. Qiao, *InfoMat.* **2024**, *6*, 12539.
[101] M. Kang, H.-J. Chai, H. B. Jeong, C. Park, I.-y. Jung, E. Park, M. M. Çiçek, I. Lee, B.-S. Bae, E. Durgun, J. Y. Kwak, S. Song, S.-Y. Choi, H. Y. Jeong, K. Kang, *ACS. Nano.* **2021**, *15*, 8715.
[102] M. T. Hossain, T. Jena, P. K. Giri, *Small. Struct.* **2024**, *5*, 2300511.
[103] X. Ren, X. He, Z. Duan, X. An, Y. Li, F. Gao, J. Zhang, P. Hu, *ACS. Photonics.* **2024**, *11*, 4990.
[104] X. Ren, X. He, X. Li, Y. Li, F. Gao, J. Zhang, P. Hu, *Adv. Opt. Mater.* **2024**, *12*, 2302852.
[105] W. Wang, Y. Meng, Y. Zhang, Z. Zhang, W. Wang, Z. Lai, P. Xie, D. Li, D. Chen, Q. Quan, D. Yin, C. Liu, Z. Yang, S. Yip, J. C. Ho, *Adv. Mater.* **2023**, *35*, 2210854.


© 2025 Wiley-VCH GmbH

16136829, 0, Downloaded from https://onlinelibrary.wiley.com/doi/10.1002/smll.202503717 by City University Of Hong Kong, Wiley Online Library on [19/08/2025]. See the Terms and Conditions (https://onlinelibrary.wiley.com/terms-and-conditions) on Wiley Online Library for rules of use; OA articles are governed by the applicable Creative Commons License

[106] W. Ci, P. Wang, W. Xue, H. Yuan, X. Xu, *Adv. Funct. Mater.* **2024**, *34*, 2316360.
[107] Z. Shang, L. Liu, G. Wang, H. Xu, Y. Cui, J. Deng, Z. Lou, Y. Yan, J. Deng, S.-T. Han, T. Zhai, X. Wang, L. Wang, X. Wang, *ACS. Nano.* **2024**, *18*, 30530.
[108] W. Han, X. Zheng, K. Yang, C. S. Tsang, F. Zheng, L. W. Wong, K. H. Lai, T. Yang, Q. Wei, M. Li, W. F. Io, F. Guo, Y. Cai, N. Wang, J. Hao, S. P. Lau, C.-S. Lee, T. H. Ly, M. Yang, J. Zhao, *Nat. Nanotechnol.* **2023**, *18*, 55.
[109] Y.-R. Jeon, D. Kim, C. Biswas, N. D. Ignacio, P. Carmichael, S. Feng, K. Lai, D.-H. Kim, D. Akinwande, *Adv. Mater.* **2025**, *37*, 2413178.
[110] K. Liu, T. Zhang, B. Dang, L. Bao, L. Xu, C. Cheng, Z. Yang, R. Huang, Y. Yang, *Nat. Electron.* **2022**, *5*, 761.
[111] A. Wali, S. Das, *Adv. Funct. Mater.* **2024**, *34*, 2308129.
[112] P. Xie, D. Li, S. Yip, J. C. Ho, *Appl. Phys. Rev.* **2024**, *11*, 011303.
[113] R. Li, W. Wang, Y. Li, S. Gao, W. Yue, G. Shen, *Nano. Energy* **2023**, *111*, 108398.
[114] H. Xu, Y. Xue, Z. Liu, Q. Tang, T. Wang, X. Gao, Y. Qi, Y. P. Chen, C. Ma, Y. Jiang, *Small. Sci.* **2024**, *4*, 2300213.
[115] Y. Li, L. Wang, Y. Ouyang, D. Li, Y. Yan, K. Dai, L. Shang, J. Zhang, L. Zhu, Y. Li, Z. Hu, *Mater. Today* **2024**, *83*, 12.
[116] X. Du, Y. Wang, Y. Cui, G. Rao, J. Huang, X. Chen, T. Zhou, C. Wu, Z. Yang, H. Cui, Y. Zhao, J. Xiong, *Nat. Electron.* **2024**, *7*, 984.
[117] Y. Jeong, H. J. Lee, J. Park, S. Lee, H.-J. Jin, S. Park, H. Cho, S. Hong, T. Kim, K. Kim, S. Choi, S. Im, *Npj. 2D. Mater. Appl.* **2022**, *6*, 23.
[118] M. A. Khan, M. F. Khan, M. Nasim, E. Elahi, M. Rabeel, M. Asim, A. Rehmat, M. H. Pervez, S. Rehman, H. Kim, J. Eom, *Adv. Funct. Mater.* **2024**, *34*, 2410974.
[119] Y. Cao, T. Zhao, C. Liu, C. Zhao, H. Gao, S. Huang, X. Li, C. Wang, Y. Liu, E. G. Lim, Z. Wen, *Nano Energy* **2023**, *112*, 108441.
[120] L. Xu, J. Liu, X. Guo, S. Liu, X. Lai, J. Wang, M. Yu, Z. Xie, H. Peng, X. Zou, X. Wang, R. Huang, M. He, *Nat. Commun.* **2024**, *15*, 9011.
[121] Y. Zhang, L. Li, Y. Lin, X. Miao, H. Lei, Y. Pan, *Nano. Energy* **2025**, *133*, 110511.
[122] D. D. Kumbhar, Y. Je, S. Hong, D. Lee, H. Kim, M. J. Kwon, S.-Y. Cho, D.-H. Lee, D.-H. Lim, S. Kim, J. H. Park, *Adv. Funct. Mater.* **2024**, *34*, 2311994.
[123] J. Oh, S. Park, S. H. Lee, S. Kim, H. Lee, C. Lee, W. Hong, J.-H. Cha, M. Kang, J. H. Jin, S. G. Im, M. J. Kim, S.-Y. Choi, *Adv. Sci.* **2024**, *11*, 2308847.
[124] L. Liu, P. Gao, M. Zhang, J. Dou, C. Liu, T. Shi, H. Huang, C. Wang, H. He, Z. Chen, Y. Chai, J. Wang, X. Zou, L. Liao, J. Wang, P. Zhou, *Adv. Sci.* **2024**, *11*, 2408210.
[125] Y. Chen, Z. Wang, J. Du, C. Si, C. Jiang, S. Yang, *ACS. Nano.* **2024**, *18*, 30871.
[126] F. Tan, Y. Cao, W. Sang, Z. Han, H. Li, T. Wang, W. Songlu, Y. Gan, Y. Yu, X. Zhang, T. Liu, D. Xiang, *Mater. Today* **2024**, *81*, 23.
[127] C. Liu, J. Pan, Q. Yuan, C. Zhu, J. Liu, F. Ge, J. Zhu, H. Xie, D. Zhou, Z. Zhang, P. Zhao, B. Tian, W. Huang, L. Wang, *Adv. Mater.* **2024**, *36*, 2305580.
[128] W. Li, J. Li, T. Mu, J. Li, P. Sun, M. Dai, Y. Chen, R. Yang, Z. Chen, Y. Wang, Y. Wu, S. Wang, *Small* **2024**, *20*, 2311630.
[129] S. Ma, Y. Zhou, T. Wan, Q. Ren, J. Yan, L. Fan, H. Yuan, M. Chan, Y. Chai, *Nano. Lett.* **2024**, *24*, 7091.
[130] F. Yang, H. K. Ng, X. Ju, W. Cai, J. Cao, D. Chi, A. Suwardi, G. Hu, Z. Ni, X. R. Wang, J. Lu, J. Wu, *Adv. Funct. Mater.* **2024**, *34*, 2310438.
[131] A. V. Papavasileiou, M. Menelaou, K. J. Sarkar, Z. Sofer, L. Polavarapu, S. Mourdikoudis, *Adv. Funct. Mater.* **2024**, *34*, 2309046.
[132] C. Chen, Y. Zhou, L. Tong, Y. Pang, J. Xu, *Adv. Mater.* **2025**, *37*, 2400332.
[133] Q. Liu, S. Cui, R. Bian, E. Pan, G. Cao, W. Li, F. Liu, *ACS Nano* **2024**, *18*, 1778.
[134] G. Wu, L. Xiang, W. Wang, C. Yao, Z. Yan, C. Zhang, J. Wu, Y. Liu, B. Zheng, H. Liu, C. Hu, X. Sun, C. Zhu, Y. Wang, X. Xiong, Y. Wu, L. Gao, D. Li, A. Pan, S. Li, *Sci. Bull.* **2024**, *69*, 473.
[135] H. Jiang, L. Li, Y. Wu, R. Duan, K. Yi, L. Wu, C. Zhu, L. Luo, M. Xu, L. Zheng, X. Gan, W. Zhao, X. Wang, Z. Liu, *Adv. Mater.* **2024**, *36*, 2400670.
[136] T. H. Yang, B.-W. Liang, H.-C. Hu, F.-X. Chen, S.-Z. Ho, W.-H. Chang, L. Yang, H.-C. Lo, T.-H. Kuo, J.-H. Chen, P.-Y. Lin, K. B. Simbulan, Z.-F. Luo, A. C. Chang, Y.-H. Kuo, Y.-S. Ku, Y.-C. Chen, Y.-J. Huang, Y.-C. Chang, Y.-F. Chiang, T.-H. Lu, M.-H. Lee, K.-S. Li, M. Wu, Y.-C. Chen, C.-L. Lin, Y.-W. Lan, *Nat. Electron.* **2024**, *7*, 29.
[137] R. Bian, R. He, E. Pan, Z. Li, G. Cao, P. Meng, J. Chen, Q. Liu, Z. Zhong, W. Li, F. Liu, *Science* **2024**, *385*, 57.
[138] Y. Gong, R. Duan, Y. Hu, Y. Wu, S. Zhu, X. Wang, Q. Wang, S. P. Lau, Z. Liu, B. K. Tay, *Nat. Commun.* **2025**, *16*, 230.
[139] P. Wang, J. Li, W. Xue, W. Ci, F. Jiang, L. Shi, F. Zhou, P. Zhou, X. Xu, *Adv. Sci.* **2024**, *11*, 2305679.
[140] Y. Zhou, Y. Wang, F. Zhuge, J. Guo, S. Ma, J. Wang, Z. Tang, Y. Li, X. Miao, Y. He, Y. Chai, *Adv. Mater.* **2022**, *34*, 2107754.
[141] F. Zhou, Y. Chai, *Nat. Electron.* **2020**, *3*, 664.
[142] J. Wang, N. Ilyas, Y. Ren, Y. Ji, S. Li, C. Li, F. Liu, D. Gu, K.-W. Ang, *Adv. Mater.* **2024**, *36*, 2307393.
[143] J. K. Lappalainen, F. D. Tschopp, S. Prakhya, M. McGill, A. Nern, K. Shinomiya, S.-y. Takemura, E. Gruntman, J. H. Macke, S. C. Turaga, *Nature* **2024**, *634*, 1132.
[144] C. Liu, J. Guo, L. Yu, J. Li, M. Zhang, H. Li, Y. Shi, D. Dai, *Light Sci. Appl.* **2021**, *10*, 123.
[145] C. Zhu, H. Liu, W. Wang, L. Xiang, J. Jiang, Q. Shuai, X. Yang, T. Zhang, B. Zheng, H. Wang, D. Li, A. Pan, *Light Sci. Appl.* **2022**, *11*, 337.
[146] H. Jiang, H. Ji, Z. Ma, D. Yang, J. Ma, M. Zhang, X. Li, M. Wang, Y. Li, X. Chen, D. Wu, X. Li, C. Shan, Z. Shi, *Light Sci. Appl.* **2024**, *13*, 316.
[147] Z.-A. Li, C. Pan, P. Wang, Y. Yang, W. Yu, Y. Zhao, G. Ruan, C. Wang, J. Mei, P. Zeng, X. Wang, Z. Ni, B. Cheng, S.-J. Liang, F. Miao, *ACS. Nano.* **2025**, *19*, 6263.
[148] Y. Zhang, B. Wang, Z. Han, X. Shi, N. Zhang, T. Miao, D. Lin, Z. Jiang, M. Liu, H. Guo, J. Zhang, H. Hu, L. Wang, *ACS. Photonics.* **2023**, *10*, 1575.
[149] Z. Zhu, L. Liu, S. Deng, N. Xu, *ACS. Nano.* **2025**, *19*, 3645.
[150] Z. Gao, R. Jiang, M. Deng, C. Zhao, Z. Hong, L. Shang, Y. Li, L. Zhu, J. Zhang, J. Zhang, Z. Hu, *Adv. Mater.* **2024**, *36*, 2401585.
[151] Z. Liu, Y. Wang, Y. Zhang, S. Sun, T. Zhang, Y.-J. Zeng, L. Hu, F. Zhuge, B. Lu, X. Pan, Z. Ye, *Adv. Mater.* **2025**, *37*, 2410783.
[152] J. Jiang, W. Xu, Z. Sun, L. Fu, S. Zhang, B. Qin, T. Fan, G. Li, S. Chen, S. Yang, W. Ge, B. Shen, N. Tang, *Small* **2024**, *20*, 2306068.
[153] N. Higashitarumizu, S. Wang, S. Wang, H. Kim, J. Bullock, A. Javey, *Nano Lett.* **2024**, *24*, 13107.
[154] R. Lu, Y. Li, H. Song, J. Jiang, *Adv. Funct. Mater.* **2025**, *35*, 2423770.
[155] Y. Hao, T. Hang, C. Chen, C. Zhang, Y. Chen, C. Yu, S. Wu, J. Yang, Z. Yang, X. Li, G. Cao, *Adv. Funct. Mater.* **2024**, *35*, 2416475.
[156] Z. Liu, M. Liu, L. Qi, N. Zhang, B. Wang, X. Sun, R. Zhang, D. Li, S. Li, *Light. Sci. Appl.* **2025**, *14*, 68.
[157] J. Pan, S. Chen, S. Chen, J. Wang, M. Su, R. Jia, J. Jie, X. Zhang, *Adv. Mater.* **2025**, *37*, 2415530.
[158] C. Su, M. Li, H. Yan, Y. Zhang, H. Li, W. Fan, W. Bai, X. Liu, Q. Wang, S. Yin, *ACS Appl. Mater. Interfaces.* **2025**, *17*, 5213.
[159] M. Che, B. Wang, X. Zhao, Y. Li, C. Chang, M. Liu, Y. Du, L. Qi, N. Zhang, Y. Zou, S. Li, *ACS. Nano.* **2024**, *18*, 30884.
[160] Y. Li, Y. Zhang, Y. Wang, J. Sun, Q. You, M. Zhu, L. Li, T. Deng, *Adv. Funct. Mater.* **2024**, *34*, 2302288.
[161] A. Chaves, J. G. Azadani, H. Alsalman, D. R. da Costa, R. Frisenda, A. J. Chaves, S. H. Song, Y. D. Kim, D. He, J. Zhou, A. Castellanos-


© 2025 Wiley-VCH GmbH

16136829, 0, Downloaded from https://onlinelibrary.wiley.com/doi/10.1002/smll.202503717 by City University Of Hong Kong, Wiley Online Library on [19/08/2025]. See the Terms and Conditions (https://onlinelibrary.wiley.com/terms-and-conditions) on Wiley Online Library for rules of use; OA articles are governed by the applicable Creative Commons License

Gomez, F. M. Peeters, Z. Liu, C. L. Hinkle, S.-H. Oh, P. D. Ye, S. J. Koester, Y. H. Lee, P. Avouris, X. Wang, T. Low, *npj 2D Mater. Appl.* **2020**, *4*, 29.
[162] Z. Su, Y. Yan, M. Sun, Z. Xuan, H. Cheng, D. Luo, Z. Gao, H. Yu, H. Zhang, C. Zuo, H. Sun, *Adv. Funct. Mater.* **2024**, *34*, 2316802.
[163] M. M. Islam, M. S. Rahman, H. Heldmyer, S. S. Han, Y. Jung, T. Roy, *NPJ. 2D. Mater. Appl.* **2024**, *8*, 21.
[164] M. M. Islam, A. Krishnaprasad, D. Dev, R. Martinez-Martinez, V. Okonkwo, B. Wu, S. S. Han, T.-S. Bae, H.-S. Chung, J. Touma, Y. Jung, T. Roy, *ACS. Nano.* **2022**, *16*, 10188.
[165] A. Rani, M. J. Sultan, W. Ren, A. Bag, H. J. Lee, N.-E. Lee, T. G. Kim, *Small* **2024**, *20*, 2310013.
[166] H. Jo, J. Jang, H. J. Park, H. Lee, S. J. An, J. P. Hong, M. S. Jeong, H. Oh, *ACS. Nano.* **2024**, *18*, 30761.
[167] Y. Cheng, Z. Li, Y. Lin, Z. Wang, X. Shan, Y. Tao, X. Zhao, H. Xu, Y. Liu, *Adv. Funct. Mater.* **2025**, *35*, 2414404.
[168] W. Zhang, B. Gao, J. Tang, P. Yao, S. Yu, M.-F. Chang, H.-J. Yoo, H. Qian, H. Wu, *Nat. Electron.* **2020**, *3*, 371.
[169] Y. Zhou, J. Fu, Z. Chen, F. Zhuge, Y. Wang, J. Yan, S. Ma, L. Xu, H. Yuan, M. Chan, X. Miao, Y. He, Y. Chai, *Nat. Electron.* **2023**, *6*, 870.
[170] Y. Yan, N. Yu, Z. Yu, Y. Su, J. Chen, T. Xiang, Y. Han, J. Wang, *Small. Methods.* **2023**, *7*, 2201679.
[171] M. C. Sahu, S. Sahoo, S. K. Mallik, A. K. Jena, S. Sahoo, *Adv. Mater. Technol.* **2023**, *8*, 2201125.
[172] C. W. Lee, C. Yoo, S. S. Han, Y.-J. Song, S. J. Kim, J. H. Kim, Y. Jung, *ACS. Nano.* **2024**, *18*, 18635.
[173] J. Gong, Y. Wei, Y. Wang, Z. Feng, J. Yu, L. Cheng, M. Chen, L. Li, Z. L. Wang, Q. Sun, *Adv. Funct. Mater.* **2024**, *34*, 2408435.
[174] P. Xie, Y. Xu, J. Wang, D. Li, Y. Zhang, Z. Zeng, B. Gao, Q. Quan, B. Li, Y. Meng, W. Wang, Y. Li, Y. Yan, Y. Shen, J. Sun, J. C. Ho, *Nat. Commun.* **2024**, *15*, 8298.
[175] B. Mota, S. Herculano-Houzel, *Science* **2015**, *349*, 74.
[176] D. C. Van Essen, J. L. Gallant, *Neuron* **1994**, *13*, 1.
[177] L. Xu, W. Wang, Y. Li, Y. Lin, W. Yue, K. Qian, Q. Guo, J. Kim, G. Shen, *Nano. Res.* **2024**, *17*, 1902.
[178] D. Kumar, L. Joharji, H. Li, A. Rezk, A. Nayfeh, N. El-Atab, *Light. Sci. Appl.* **2023**, *12*, 109.
[179] Y. Deng, S. Liu, M. Li, N. Zhang, Y. Feng, J. Han, Y. Kapitonov, Y. Li, T. Zhai, *Chip* **2024**, *3*, 100088.
[180] F. Wang, F. Hu, M. Dai, S. Zhu, F. Sun, R. Duan, C. Wang, J. Han, W. Deng, W. Chen, M. Ye, S. Han, B. Qiang, Y. Jin, Y. Chua, N. Chi, S. Yu, D. Nam, S. H. Chae, Z. Liu, Q. J. Wang, *Nat. Commun.* **2023**, *14*, 1938.
[181] P.-Y. Huang, B.-Y. Jiang, H.-J. Chen, J.-Y. Xu, K. Wang, C.-Y. Zhu, X.-Y. Hu, D. Li, L. Zhen, F.-C. Zhou, J.-K. Qin, C.-Y. Xu, *Nat. Commun.* **2023**, *14*, 6736.
[182] M. Lee, Y. Kim, S. H. Mo, S. Kim, K. Eom, H. Lee, *Small* **2024**, *20*, 2309851.
[183] T. Zhang, X. Guo, P. Wang, X. Fan, Z. Wang, Y. Tong, D. Wang, L. Tong, L. Li, *Nat. Commun.* **2024**, *15*, 2471.
[184] L. Chen, R. Li, S. Yuan, A. Chen, Y. Li, T. Zhang, L. Wei, Q. Zhang, Q. Li, *Matter* **2023**, *6*, 925.
[185] Y. Wei, J. Yu, Y. Li, Y. Wang, Z. Huo, L. Cheng, D. Yue, K. Zhang, J. Gong, J. Wang, Z. L. Wang, Q. Sun, *Nano. Energy.* **2024**, *126*, 109622.
[186] Y. Sun, H. Wang, D. Xie, *Nano-Micro Lett.* **2024**, *16*, 211.
[187] X. Wu, S. Shi, J. Jiang, D. Lin, J. Song, Z. Wang, W. Huang, *Adv. Mater.* **2025**, *37*, 2419159.
[188] H. W. Song, D. Moon, Y. Won, Y. K. Cha, J. Yoo, T. H. Park, J. H. Oh, *Sci. Adv.* **2021**, *10*, adl2882.
[189] X. Cheng, Z. Shen, Y. Zhang, *Natl. Sci. Rev.* **2024**, *11*, nwad314.
[190] C. Yoo, S. S. Han, C. W. Lee, J. Pond, Y.-J. Song, J. H. Kim, Y. Jung, *Nano Lett.* **2025**, *25*, 106.
[191] L. Cheng, J. Yu, Y. Wei, Z. Feng, Y. Li, Y. Wang, N. Xu, Z. L. Wang, Q. Sun, *Nano. Energy.* **2023**, *114*, 108632.
[192] W. Zhang, S. Ma, X. Ji, X. Liu, Y. Cong, L. Shi, *Nat. Electron.* **2024**, *7*, 954.
[193] Z. Dong, Q. Hua, J. Xi, Y. Shi, T. Huang, X. Dai, J. Niu, B. Wang, Z. L. Wang, W. Hu, *Nano Lett.* **2023**, *23*, 3842.
[194] J. Yu, J. Fu, H. Ruan, H. Wang, Y. Yu, J. Wang, Y. He, J. Wu, F. Zhuge, Y. Ma, T. Zhai, *InfoMat.* **2024**, *6*, 12599.
[195] C.-M. Song, D. Kim, S. Lee, H.-J. Kwon, *Adv. Sci.* **2024**, *11*, 2308588.
[196] F. Guo, W. F. Io, Z. Dang, R. Ding, S.-Y. Pang, Y. Zhao, J. Hao, *Mater. Horiz* **2023**, *10*, 3719.
[197] K. Roy, A. Jaiswal, P. Panda, *Nature* **2019**, *575*, 607.
[198] Z. Weng, H. Zheng, L. Li, W. Lei, H. Jiang, K.-W. Ang, Z. Zhao, *Small.* **2024**, *20*, 2304518.
[199] J. An, N. Zhang, F. Tan, X. Zhao, C. Chang, M. Lanza, S. Li, *Small* **2024**, *20*, 2403103.
[200] P. Guo, M. Jia, D. Guo, Z. L. Wang, J. Zhai, *Matter* **2023**, *6*, 537.
[201] J. Bai, D. He, B. Dang, K. Liu, Z. Yang, J. Wang, X. Zhang, Y. Wang, Y. Tao, Y. Yang, *Adv. Mater.* **2024**, *36*, 2401060.
[202] J. Zhou, A. Chen, Y. Zhang, X. Zhang, J. Chai, J. Hu, H. Li, Y. Xu, X. Liu, N. Tan, F. Xue, B. Yu, *Nano. Lett.* **2024**, *24*, 14892.
[203] Y. Xia, N. Lin, J. Zha, H. Huang, Y. Zhang, H. Liu, J. Tong, S. Xu, P. Yang, H. Wang, L. Zheng, Z. Zhang, Z. Yang, Y. Chen, H. P. Chan, Z. Wang, C. Tan, *Adv. Mater.* **2024**, *36*, 2403785.
[204] J. Yao, Q. Wang, Y. Zhang, Y. Teng, J. Li, P. Zhao, C. Zhao, Z. Hu, Z. Shen, L. Liu, D. Tian, S. Qiu, Z. Wang, L. Kang, Q. Li, *Nat. Commun.* **2024**, *15*, 6147.
[205] B. Dang, T. Zhang, X. Wu, K. Liu, R. Huang, Y. Yang, *Nat. Electron.* **2024**, *7*, 991.
[206] S. Al Abdul Wahid, A. Asad, F. Mohammadi, *Electronics* **2024**, *13*, 2963.
[207] A. S. G. Andrae, T. Edler, *Challenges* **2015**, *6*, 117.
[208] S. Hadke, M.-A. Kang, V. K. Sangwan, M. C. Hersam, *Chem. Rev.* **2025**, *125*, 835.
[209] D. R. Muir, S. Sheik, *Nat. Commun.* **2025**, *16*, 3586.
[210] Z. Yang, Z. Zhang, S. Huo, F. Meng, Y. Wang, Y. Ma, B. Liu, F. Meng, Y. Xie, E. Wu, *SmartMat* **2025**, *6*, 70005.
[211] M. Ao, X. Zhou, X. Kong, S. Gou, S. Chen, X. Dong, Y. Zhu, Q. Sun, Z. Zhang, J. Zhang, Q. Zhang, Y. Hu, C. Sheng, K. Wang, S. Wang, J. Wan, J. Han, W. Bao, P. Zhou, *Nature* **2025**, *640*, 654.
[212] S. J. Kim, H.-J. Lee, C.-H. Lee, H. W. Jang, *npj 2D Mater. Appl.* **2024**, *8*, 70.


© 2025 Wiley-VCH GmbH

16136829, 0, Downloaded from https://onlinelibrary.wiley.com/doi/10.1002/smll.202503717 by City University Of Hong Kong, Wiley Online Library on [19/08/2025]. See the Terms and Conditions (https://onlinelibrary.wiley.com/terms-and-conditions) on Wiley Online Library for rules of use; OA articles are governed by the applicable Creative Commons License

**Pengshan Xie** is now a Postdoctoral Research Fellow in the Department of Materials Science and Engineering at the City University of Hong Kong. He received his B.S. and M.S. degrees from Central South University in 2017 and 2020, respectively, and his Ph.D. from City University of Hong Kong in 2024. His research interests mainly focus on the fabrication of nanomaterials, including III-V semiconductor nanowires, novel neuromorphic electronics, and field-effect transistors.

**Dengji Li** received his Ph.D. from City University of Hong Kong, following his B.S. degree at Wuhan University in 2016 and his M.S. degree from the University of Electronic Science and Technology of China. Currently, he serves as a Postdoctoral Fellow in the Department of Materials Science and Engineering at City University of Hong Kong. His research focuses on nanomaterial fabrication, including perovskite nanostructures (nanowires, nanosheets, and arrays), III-V semiconductor nanowires, as well as the development of novel neuromorphic electronics, field-effect transistors, and gas sensors.

**Weijun Wang** is currently a Postdoctoral Research Fellow in the Department of Materials Science and Engineering at the City University of Hong Kong. He received his B.S. and M.S. degrees from Harbin University of Science and Technology and Harbin Institute of Technology in 2016 and 2018, respectively, and his Ph.D. from the City University of Hong Kong in 2024. His research interests focus on low-dimensional materials and their heterostructures, particularly for 1D/2D materials synthesis, novel field-effect transistors, and neuromorphic electronics.

**Johnny C. Ho** is a Chair Professor of Materials Science and Engineering at City University of Hong Kong. He received his B.S. degree in chemical engineering, and his MS and Ph.D. degrees in Materials Science and Engineering from the University of California, Berkeley, in 2002, 2005, and 2009, respectively. From 2009 to 2010, he was a postdoctoral research fellow in the Nanoscale Synthesis and Characterization Group at Lawrence Livermore National Laboratory. His research interests focus on synthesis, characterization, integration, and device applications of nanoscale materials for various technological applications, including nanoelectronics, sensors, and energy harvesting.



© 2025 Wiley-VCH GmbH

16136829, 0, Downloaded from https://onlinelibrary.wiley.com/doi/10.1002/smll.202503717 by City University Of Hong Kong, Wiley Online Library on [19/08/2025]. See the Terms and Conditions (https://onlinelibrary.wiley.com/terms-and-conditions) on Wiley Online Library for rules of use; OA articles are governed by the applicable Creative Commons License